Testing the Limits of Approximate Solutions of the Quantum-Classical Liouville Equation for Modelling Quantum Processes Occurring in Condensed Phase Environments

by
Franz Martinez Rios

A thesis submitted in partial fulfillment of the requirements for the degree of
Doctor of Philosophy

Department of Chemistry
University of Alberta

Abstract

Many methods exist for simulating the nonadiabatic dynamics of mixed quantum-classical systems, some of which are more accurate than others. Some of the most accurate methods are based on solving the quantum-classical Liouville equation (QCLE) represented in the adiabatic basis, in terms of an ensemble of surface-hopping trajectories. However, long-time dynamics simulations of observables using these methods are computationally demanding as very large numbers of trajectories are required for convergence. Motivated by the need for more efficient approaches, more approximate methods were previously developed, but starting from a representation of the QCLE in the so-called mapping basis. These methods, known as the Poisson Bracket Mapping Equation (PBME) and Forward-Backward Trajectory Solution (FBTS), treat both the quantum and classical degrees of freedom in terms of continuous variables that evolve according to classical-like equations of motion. Owing to the approximate nature of these methods, it is necessary to understand the conditions under which they are valid. In this thesis, three studies were conducted to shed light on this matter. The first study was concerned with the laying down and testing of a formalism for calculating nonlinear spectroscopic signals efficiently using PBME and FBTS dynamics. In particular, expressions for simulating a time-integrated pump-probe transient absorption (TA) signal were first derived based on the so-called equation-of-motion phase-matching approach and then used to calculate the TA signal in a reduced model of a condensed phase photo-induced electron transfer (PIET) reaction. In the second study, calculations of TA signals were carried out for a more complex PIET model, in which the PIET takes place in a complex with an inner sphere vibrational mode. The details of how PBME and FBTS can be implemented for vibronic systems were worked out for two cases: one in which the vibrational mode is quantized and the other in which it is treated classically. In the third study, PBME simulations of a realistic model of a proton transfer (PT) reaction in a phenol-trimethylamine complex dissolved in a polar nanocluster are performed and analyzed. Expressions for calculating free energies as a function of both a classical and quantum reaction coordinate are derived and then evaluated for the PT reaction. The results of these studies collectively demonstrate that it is possible to extract useful information from PBME/FBTS simulations of nonlinear spectroscopic signals and about the dynamical behaviour of more realistic systems. However, great care must be taken in choosing which systems/conditions to apply these methods to. Beyond the limits of their underlying approximations, PBME/FBTS can yield highly inaccurate results and even portray a very different qualitative picture of a system's dynamical behaviour.

Preface

The candidate confirms that the work submitted is his own, except where work which has formed part of jointly-authored publications has been included. The contribution of the candidate and the other authors to this work is indicated explicitly below.

The research conducted for this thesis forms part of an ongoing original research program, led by Prof. Gabriel Hanna. The computer programs used for the data generation in Chapters 3, 4, and 5 were developed mostly by the candidate, with the help of Prof. Gabriel Hanna and some contributions by Dr. Najeh Rekik in Chapter 3. The data collection/analysis for Chapters 3 to 5 is original work done by the candidate. Further details of the jointly-authored publications are included below.

Chapter 3 of the thesis was published in F. Martinez, N. Rekik, G. Hanna, "Simulation of Nonlinear Optical Signals Via Approximate Solutions of the Quantum-Classical Liouville Equation: Application to the Pump-Probe Spectroscopy of a Condensed Phase Electron Transfer Reaction" Chem. Phys. Lett. 2013, 573, 77-83. The candidate was responsible for finishing/debugging/testing the code required for the data generation, collecting and analyzing the data, writing the first draft of the manuscript, and making refinements to the manuscript as instructed by Prof. Gabriel Hanna. Dr. Najeh Rekik contributed to the development of the theory and was responsible for the initial development of the code. Prof. Gabriel Hanna developed the original idea for the work, aided in laying down the theory, aided in the initial development of the code and debugging, revised the first draft of the manuscript, and worked with the candidate to refine the manuscript.

Chapter 4 of the thesis was published in F. Martinez, G. Hanna, "Mixed Quantum-Classical Simulations of Transient Absorption Pump-Probe Signals for a Photo-Induced Electron Transfer Reaction Coupled to an Inner-Sphere Vibrational Mode" J. Phys. Chem. A 2016, 120, 3196-3205. The candidate was responsible for developing/debugging/testing the code required for the data generation, collecting and analyzing the data, writing the first draft of the manuscript, and making refinements to the manuscript as instructed by Prof. Gabriel Hanna. Prof. Gabriel Hanna developed the original idea for the work, aided in laying down the theory, revised the first draft of the manuscript, and worked with the candidate to refine the manuscript.

The first two sections of Chapter 5 (i.e. Sections 5.1 and 5.2) were published in F. Martinez, G. Hanna, "Assessment of Approximate Solutions of the Quantum-Classical Liouville Equation for Dynamics Simulations of Quantum Subsystems Embedded in Classical Environments" Mol. Sim. 2015, 41, 107-122. The candidate was responsible for developing/debugging/testing the code required for the data generation, collecting and analyzing the data, writing the first draft of the manuscript, and making refinements to the manuscript as instructed by Prof. Gabriel Hanna. Prof. Gabriel Hanna developed the original idea for the work, aided in laying down the theory, revised the first draft of the manuscript, and worked with the candidate to refine the manuscript.

Acknowledgements

I would like to express my gratitude to my supervisor Prof. Gabriel Hanna for all his support and guidance during my Ph.D. studies.

I would also like to give special thanks to the members of my thesis committee: Prof. Yunjie Xu, Prof. James Harynuk, Prof. Arthur Mar, and Prof. Jeremy Schofield for reading and commenting on the work presented in this thesis.

My sincere thanks also goes to Robert and Anna Jordan for their help and encouragement during these past years.

And, last but not least, thanks to my fellow labmates and my family.

Contents

List of Tables

List of Figures

Chapter 1

Introduction

Understanding dynamical phenomena occurring in chemical and biological systems often requires an in-depth understanding of the underlying molecular dynamics. The widely accepted theory for explaining the dynamics of the microscopic world is quantum mechanics. Therefore, to study microscopic processes, one must consider the quantum mechanical nature of the systems in which they occur. To this end, the use of quantum dynamics simulations in interpreting experimental data, determining mechanisms, and guiding new experiments is necessary. However, when studying molecular systems with many degrees of freedom (DOF), such simulations are computationally intractable. One commonly employed way of circumventing this issue is to decompose a large system into two parts: a subsystem, which is the primary object of study (e.g. key proton(s) and/or electron(s) in a charge transfer reaction, key chromophores involved in a vibrational/electronic energy transfer process, excitons in a light harvesting system, etc.) and an environment (or bath), which contains the remaining degrees of freedom in the system (e.g., the rest of a molecule, protein, solvent, etc.). When a system is partitioned in this way, the challenge is to develop methods for simulating the dynamics of a subsystem while coupled to its environment (such a subsystem is commonly referred to as an open quantum system). This topic has been the subject of intensive research for many years in the chemical physics community.[1–3].

The concept of partitioning a system into different sets of DOF is at the heart of quantum chemistry. The Born–Oppenheimer (BO) approximation, which assumes a time/energy scale separation between the motion of nuclei and electrons, greatly simplifies quantum chemical calculations of molecular energies and wave functions. Within this approximation, the Schrödinger equation can be solved for the electronic DOF for a fixed configuration of the nuclei to obtain the electronic energies and wave functions. If the process is repeated by varying the positions of the nuclei in small steps, one can obtain the electronic energies as a function of the nuclear positions or the potential energy surfaces (PESs). Given the assumption of an energy scale separation between the nuclei and electrons, the system is restricted to evolve on a single PES, i.e., the electrons do not have enough energy to hop to another electronic PES because the energy gap between the PESs is relatively large. This is known as *adiabatic* dynamics. However, when the energy scales become comparable, the BO approximation may break down and the electrons can hop between different PESs. This *nonadiabatic* dynamics typically occurs in the vicinity of avoided crossings and conical intersections between PESs.

In general, adiabatic dynamics arises whenever one set of DOF changes slowly compared to another set, similar to the motions of nuclei and electrons in the BO approximation. For example, if one is able to partition a system into a subsystem containing very fast DOF of interest and an environment containing very slow DOF, then the dynamics of the environmental DOF will be governed by a single PES corresponding to the subsystem. However, when the time scales of motion of the subsystem and environmental DOF become comparable, motion on a single PES is no longer sufficient to accurately capture the dynamics of the slower DOF. Many important processes in chemistry and biology involve this nonadiabatic dynamics. Examples include intersystem crossings and internal conversions in photochemistry, electron transfer reactions in electrochemistry, ion–molecule reactions, reactions at metal surfaces, photo-induced dynamics of molecules adsorbed to semiconductor substrates (as in a photovoltaic cell), photo-induced dynamics in quantum dots, etc. Due to the ubiquity of nonadiabatic dynamics in chemistry and biology, a great deal of effort has been devoted to developing simulation methods that are capable of taking nonadiabatic effects into account. The most accurate methods, such as the multi-configuration time-dependent Hartree (MC-TDH) method[4–6], treat both the subsystem and environment fully quantum mechanically, but are highly computationally demanding and therefore restricted to molecular systems with tens of degrees of freedom [7, 8]. Less computationally demanding methods include path integral-based methods such as centroid molecular dynamics (CMD) [9–13], ring polymer molecular dynamics (RPMD) [14, 15], and the Feynman-Kleinert quasi-classical Wigner method [16, 17], and semiclassical methods such as the semiclassical initial value representation (SC-IVR) [18–23], linearized semiclassical initial value representation (LSC-IVR) [24–27], and forward-backward initial value representation (FB-IVR) [28, 29], which impart partial quantum mechanical character to both the subsystem and environmental DOF. Of particular interest to this thesis, mixed quantum-classical methods treat the subsystem quantum mechanically and the environment classically. We will discuss these methods next.

1.1 Mixed Quantum-Classical Dynamics Methods

Over the years, many mixed quantum-classical methods have been proposed for simulating nonadiabatic dynamics, which essentially differ in the way they couple the quantum and classical DOF. [30–45] The two most widely used methods are mean-field (or Ehrenfest) and fewest switches surface-hopping (FSSH) dynamics.[39, 46–58] Mean-field dynamics is based on the assumption that the environmental motions are governed by a single effective PES, which is a weighted average over the adiabatic PESs of the subsystem. On the other hand, surface-hopping methods evolve the environmental DOF on a single adiabatic PES at any given time, with instantaneous hops to other PESs at times when the BO approximation breaks down. However, both methods suffer from several drawbacks. Both methods do not correctly describe the "quantum backreaction", i.e., the effect due to the subsystem-environment coupling where a change in the environmental DOF modifies the subsystem Hamiltonian, which in turn modifies the forces governing the motion of the environmental DOF. Mean-field dynamics is not capable of capturing decoherence, while FSSH can do so after incorporating some ad hoc corrections.[56, 58] Both of these methods struggle with satisfying detailed balance. Due to the incorrect nature of the energy transfer between the subsystem and environment, it is possible for the subsystem to approach unrealistically high temperatures in mean-field dynamics [59]; in such cases, one can employ quantum correction factors that modify the dynamics in such a way that detailed balance is enforced [60]. In FSSH, it is possible to satisfy detailed balance in certain limits if the so-called frustrated hops are allowed. [61]

Other mixed quantum-classical methods have been developed, which are based on solutions of the quantum-classical Liouville equation (QCLE). [31, 33–36, 40, 62–73] The QCLE may be rigorously derived from the quantum Liouville equation in the limit that the environmental DOF are much heavier than the subsystem DOF and, as a result, its solution provides one of the most accurate methods for simulating mixed quantum-classical dynamics.[33] When the QCLE is represented in the adiabatic basis (i.e., set of eigenstates of the system Hamiltonian), its solution can be obtained from an ensemble of surface-hopping trajectories using the sequential short-time propagation (SSTP) algorithm [67, 68] or the Trotter-based quantum-classical algorithm (TBQC) [68, 69], which rely on the momentum jump approximation. [68, 74] Unfortunately, simulating the dynamics of a system out to long times using these algorithms has proven to be very challenging. This is due to the rapidly growing statistical error associated with the Monte Carlo sampling of nonadiabatic transitions, which necessitates very large numbers of trajectories to obtain converged expectation values. Although filtering schemes have been developed to impede this growth, they can introduce errors in the results if they are not implemented carefully.[68, 75–77]

Motivated by the need to circumvent the issues inherent to the SSTP and TBQC algorithms, two more approximate solutions of the QCLE were developed, the Poisson Bracket Mapping Equation (PBME) solution [70, 71, 78] and the Forward-Backward trajectory solution (FBTS) [40, 72]. The PBME and FBTS methods rely on representing the QCLE in the mapping basis [23, 79, 80] and the solution to the QCLE in the coherent state basis [81], respectively, which results in a representation of the quantum DOF in terms of continuous variables. These approaches yield relatively simple algorithms, in which the dynamics of both the quantum and classical (DOF) evolve according to classical-like equations of motion.

It is important to stress that to arrive at these simple algorithms, rather uncontrolled approximations are made that limit the situations in which these methods may be used. Consequently, they must be tested on a wide array of systems under a range of conditions to determine their domains of validity. The PBME method has been shown to accurately reproduce exact results for the spin-boson model.[70, 78, 82] However, for other systems, the PBME method has been shown to give rise to inaccurate or unphysical results [71, 83], which has been attributed to the dynamics taking the quantum variables outside of their physical space [71]. Several attempts have been made to improve the performance of PBME, either by combining it with another method or by modifying the PBME equations. An example of the first type exploits the fact that PBME can be accurate for simulating the short-time dynamics of the typically short-lived memory kernel in the generalized quantum master equation [73], while examples of the second type add approximate correction factors to the PBME in an attempt to improve its accuracy [84, 85]. The dynamics prescribed by FBTS has been shown to yield accurate results in several cases (even more accurate than PBME), but struggles in others.[40, 72, 86] In general, both PBME and FBTS struggle to reproduce the exact results under conditions of strong subsystem-environment coupling and when there is an asymmetry in the energies of the quantum subsystem states. This is due to the fact that the dynamics prescribed by both PBME and FBTS is mean-field in nature. It should be noted that the FBTS method can be improved by systematically relaxing its underlying approximation (known as the jump-FBTS method), albeit at a great computational expense.[72]

1.2 Theoretical Study of Charge Transfer Processes

In this thesis, we gauge the abilities of the PBME and FBTS approaches for quantitatively and qualitatively capturing the dynamics of two types of condensed phase charge transfer processes, which are discussed in the following subsections.

1.2.1 Photo-induced Electron Transfer Reactions

Photo-induced electron transfer (PIET) is a multi-step process, which can be described by a light-induced excitation of a donor chromophore from its ground electronic state to an excited state, followed by the transfer of an electron from the excited donor state to an excited acceptor state. The study of PIET reactions is of great importance because it is closely related to electronic energy transfer in photosynthetic systems [87–90] and it occurs in photovoltaic materials used to harvest solar energy [91–95]. Detailed information about the PIET dynamics and the participating vibrational modes may be obtained using a combination of time-resolved transient absorption (TA) pump-probe spectroscopy and theoretical modelling. This is particularly important in the case of complex systems, where the kinetics of the electron transfer is rarely captured by a single, simple exponential decay in the TA signal, but rather displays non-trivial oscillatory features due to the coupling between the donor–acceptor complex and its environment. [96–98]. Thus, simulations of the TA signals can aid in the interpretation of the various features observed in the experimental TA signals by identifying the factors that influence the reaction dynamics, e.g., coupled vibrational motions, vibronic coherences, environmental factors.

Theoretical methods for simulating nonlinear spectroscopic signals, such as a TA signal, generally fall into two categories: perturbative and nonperturbative approaches. In the perturbative approach, a desired spectroscopic signal may be obtained directly via calculations of optical response functions (ORFs), which capture the system's field-free dynamics at a particular order of the applied field in terms of multi-time dipole moment correlation functions. Unfortunately, exact quantum mechanical calculations of ORFs are feasible only in the case of very simple models. [99, 100] As the complexity of the system grows, ORFs cannot be evaluated efficiently, even with some semiclassical treatments [101–108]. Instead, mixed quantum-classical methods have provided viable alternatives for computing ORFs.[109–112] Using such methods, one often evaluates ORFs based on equilibrium classical molecular dynamics simulations of the photo-inactive DOF on the PES corresponding to the chromophore's ground state. However, when nonequilibrium solvation dynamics and nonradiative nonadiabatic transitions between multiple PESs are important, other methods based on the QCLE approach may be used.[111, 112] On the other hand, in the nonperturbative approach, one calculates the total polarization of a system by simulating its dynamics subject to the applied radiation fields. Then, the contribution corresponding to the desired spectroscopic signal is extracted by using its specific phase-matching condition.[113] Methods based on this approach have proven to be viable options for calculating a variety of nonlinear spectroscopic signals in model systems, but in the case of complex systems, the calculations become computationally expensive because, in general, a large number of simulations are needed to extract the desired signal. [113–122]

In this thesis, we adopt the equation-of-motion phase-matching approach (EOM-PMA), developed by Gelin et al. [123, 124], for calculating TA signals of PIET reactions. The EOM-PMA combines features from both the perturbative and non-perturbative approaches, and is therefore capable of calculating the time-dependent polarization of a system in any phase-matching direction in response to weak laser fields of arbitrary shape and width. In addition, it can be combined with any EOM to propagate a system's density matrix or dipole moment. In Chapter 3, we show how the EOM-PMA can be coupled with the PBME and FBTS methods to tackle larger, complex systems.

1.2.2 Proton Transfer Reactions in Nanoclusters

Proton transfer (PT) reactions constitute another class of reactions of great importance in chemical and biological processes.[125, 126] PT reactions are involved in acid-base and enzymatic reactions [127–129], and in technological applications including photostabilizers [130], information storage devices [131], and fuel cells [132–134]. Simulation of PT in condensed phases is challenging because quantum effects such as zero point energy and tunnelling are important. For this reason, various quantum dynamical methods including path integral-based methods [135–138], semiclassical methods [139, 140], and mixed quantum-classical methods [68, 135, 141–144] have been used to simulate condensed phase PT reactions.

In nanoscale environments such as those encountered in nanoclusters, aerosols, and nanomaterials, the thermodynamics, kinetics, and mechanisms of PT reactions can change significantly with respect to bulk environments because of the competition between bulk and surface forces. Therefore, an explicit treatment of the nanoscale environment is required for a proper understanding of the PT reaction. Such an understanding could lead to the development of new materials, whose size and composition could be tuned to enhance or inhibit the PT reactions. Over the years, numerous studies of PT in nanoclusters [138, 145–159] and nanoconfined environments [160–163] have been carried out. The main difference between PT in a nanocluster versus in a nanoconfined system is the possibility for the nanocluster to deform along the PT reaction, while this possibility does not exist in a nanoconfined system. In both cases, theoretical studies of PT in a nanosolvated phenol-trimethylamine complex have shown that the complex tends to reside in the center of the cluster when the complex is in its ionic form, while it tends to reside at the surface when it is in its covalent form.[155, 159, 163]

Information about the kinetics and thermodynamics of a PT reaction may be obtained by examining the free energy of the system along an appropriate reaction coordinate. A reaction coordinate is defined as a variable or function of variables that monitors the progress of a transformation from reactants to products, e.g., bond length would be used to monitor the dissociation of a diatomic molecule. For a PT reaction in a hydrogen-bonded complex, the shape of the free energy profile will depend on the strength of the hydrogen bond. In the case of a weak hydrogen bond, one expects a double-welled profile with a relatively high barrier, with each well corresponding to the covalent and ionic forms of the complex, respectively. In contrast, in the case of a strong hydrogen bond, one expects a single-welled profile or one with a relatively low barrier. A “good” reaction coordinate should be able to capture these features. Potential reaction coordinates include the proton position within the complex and, in cases where the proton is strongly coupled to its environment, the solvent polarization (a collective coordinate that depends on the solvent configuration). In a mixed quantum-classical treatment, the proton position would be treated quantum mechanically, while the solvent would be treated classically.

1.3 Objectives and Outline

The main objective of this thesis is to test the accuracy of the PBME and FBTS methods for modeling quantum processes in classical environments, namely condensed phase PIET and PT in a polar nanocluster. These processes were deliberately chosen as we were interested in testing, for the first time, to which extent these methods can qualitatively/quantitatively capture the expected behaviours in one or more of the following situations: strong subsystem-bath coupling, a complex, many-body, explicitly atomistic model of a system, a highly anharmonic subsystem, the presence of a time-dependent field-matter interaction, when calculating nonlinear spectroscopic signals, and when calculating free energy profiles. In doing so, one may gain insight into the factors that can cause these approximate solutions of the QCLE to break down. More specifically, we will investigate how well PBME and FBTS perform (i) when coupled to the EOM-PMA for efficiently simulating the TA pump-probe spectra of a model ET complex, both with and without an inner sphere vibrational mode, in a harmonic bath, (ii) for capturing the solvation dynamics of a nanocluster of polar molecules surrounding a PT complex, and (iii) for calculating the free energy profile as a function of a quantum reaction coordinate for this PT reaction.

The following is a description of the topics covered in each chapter:

- In Chapter 2, the QCLE and its approximate solutions are presented and discussed. The details for integrating the PBME and FBTS equations of motion are also provided.
- In Chapter 3, the derivations of the PBME-PMA and FBTS-PMA methods are

presented. Also, the machinery for calculating nonlinear spectroscopic signals is laid out and demonstrated with a calculation of the time-integrated pump-probe TA signal of a PIET in a model ET complex coupled a harmonic bath. The accuracies of the PBME-PMA and FBTS-PMA methods are assessed by comparing to numerically exact quantum results.

- In Chapter 4, we consider another version of the model ET complex, in which the electronic subsystem is coupled to an inner sphere vibrational mode. We present the theoretical details for implementing the PBME and FBTS dynamics in the cases where the vibrational mode is treated classically and quantum mechanically. Again, we calculate the time-integrated pump-probe TA signals using the PBME-PMA and FBTS-PMA methods and, by comparing to the numerically exact quantum results, comment on their accuracies and on how a classical versus quantum treatment of the vibrational mode affects the results.

- In Chapter 5, we examine how well PBME dynamics captures the solvation dynamics (by analyzing various properties of the solvent) in a realistic model of a PT reaction in a hydrogen-bonded complex dissolved in a nanocluster of methyl chloride molecules. We then formulate general expressions for calculating free energy profiles along an arbitrary reaction coordinate using the PBME approach. Cases in which the reaction coordinate is quantum mechanical and classical in nature are presented, and PBME simulations are used to calculate the free energy profiles of the PT reaction employing both reaction coordinates. Differences due to the nature of the reaction coordinate and the viability of PBME dynamics for calculating free energy profiles are discussed.

- Chapter 6 presents concluding remarks for the work presented in this thesis, as well as some perspectives and suggestions for future work.

Chapter 2

Approximate Solutions of the Quantum-Classical Liouville Equation

2.1 Quantum Dynamics

In quantum mechanics, the state of a closed system can be described by its wave function, which can be mathematically represented by a state vector $|\psi\rangle$. All of the information about a system is contained in its wave function and the possible results of a physical measurement are associated with the eigenvalues of the operator, $\hat{O}$, corresponding to an observable of interest. If one desires to study the dynamic behaviour of a system, either the wave function or the operator can be represented as a function of time. This gives rise to two different representations for formulating the dynamics of a quantum system. In the first case, when the time dependence is included in the state vector, the representation is known as the Schrödinger picture. Here, the time evolution is given by $|\psi(t)\rangle = \hat{U}|\psi(t_0)\rangle$, where $\hat{U}$ is a time evolution operator. On the other hand, if the operator depends on time, the representation is known as the Heisenberg picture. Here, the time evolution is given by

$$\frac{d}{dt}\hat{O}(t) = \frac{i}{\hbar}\left[\hat{H}, \hat{O}(t)\right], \tag{2.1}$$

where $\hat{H}$ is the Hamiltonian of the system and $[\cdot, \cdot]$ denotes the commutator of two operators. This approach has a direct analogy to classical physics, viz., if the operators are replaced by their classical analogues and the commutator by the Poisson bracket, the resulting equation is the classical Liouville equation. There is an additional intermediate picture, known as the Dirac or interaction picture, in which both the state vectors and operators are time-dependent. In this picture, the Hamiltonian is divided in two parts, one that is exactly solvable and another that is regarded as a perturbation. For all pictures, the expectation values of observables will be the same, but one chooses a given picture depending on the application at hand.

In the case of an open system, an ensemble of different states is required to describe the system in general, i.e., there is no single $|\psi\rangle$ that can describe it. In such cases, it is necessary to introduce a density operator, $\hat{\rho}$. For an ensemble of states, $\{|\psi_i\rangle\}$, the density operator has the following form:

$$\hat{\rho} = \sum_i p_i |\psi_i\rangle\langle\psi_i|, \tag{2.2}$$

where p_i is the probability for the system to be in state $|\psi_i\rangle$, and consequently has the property $\sum_i p_i = 1$. Using the density matrix formalism, an expectation value of an operator can be calculated using

$$\langle O\rangle = \mathrm{Tr}(\hat{\rho}\hat{O}), \tag{2.3}$$

where Tr denotes a trace operation. For a time-dependent system, one can express the time dependence either through the density operator or the operator corresponding to the observable. If the density matrix evolves in time, the evolution is given by the von Neumann equation or quantum Liouville equation,

$$i\hbar\frac{\partial\hat{\rho}(t)}{\partial t} = -\left[\hat{H}, \hat{\rho}(t)\right]. \tag{2.4}$$

The quantum Liouville equation is the quantum analogue of the classical Liouville equation which describes the time evolution of the phase space distribution function in classical physics. Alternatively, one may calculate the expectation value in Eq. 2.3 by evolving $\hat{O}(t)$, which can be done by solving the quantum Heisenberg equation in Eq. 2.1.

In some very simple cases, it is possible to find analytical and numerical solutions for the time evolution of a quantum system. However, due to the exponential scaling of computational cost with increasing system size, it is necessary to find approximate solutions to the dynamics of a system. Although approximate phenomenological methods are widely used, the best approach is to use approximate methods that can be derived from the exact quantum equations of motion. In doing so, the details of the approximations are known and, thus, one may be able to restrict a method to certain systems/conditions and/or more easily develop ways to improve the solutions when needed. The quantum-classical Liouville equation (QCLE) is one such approximate equation of motion, as it can be rigorously derived from the quantum Liouville equation. In the following sections, the QCLE is presented and the derivations of two approximate solutions of the QCLE, namely the Poisson Bracket Mapping Equation (PBME) solution and the Forward-Backward Trajectory Solution (FBTS), are outlined. The final section of the chapter is dedicated to outlining the algorithms used to integrate the equations of motion for these solutions.

2.2 The Quantum-Classical Liouville Equation

The QCLE prescribes the dynamics of the density operator, ρ, of a quantum subsystem coupled to a classical environment (or bath). It is given by [31, 33, 164–169]

$$\frac{d}{dt}\hat{\rho}_W(R,P,t) = -\frac{i}{\hbar}\left[\hat{H}_W, \hat{\rho}_W(t)\right] + \frac{1}{2}\left(\{\hat{H}_W, \hat{\rho}_W(t\} - \{\hat{\rho}_W(t), \hat{H}_W\}\right), \qquad (2.5)$$

where the Hamiltonian, $\hat{H}_W$, is given by the sum of the subsystem Hamiltonian, $\hat{h}_s(\hat{r},\hat{p})$, the environmental Hamiltonian, $H_e(R,P)$, and a subsystem-environment coupling term, $\hat{V}_c(\hat{r},R)$; R and P denote the positions and momenta of the environmental DOF, respectively; $\hat{r}$ and $\hat{p}$ denote the subsystem position and momentum operators, respectively. In the above equation, the subscript W denotes a partial Wigner transform [170] over the bath DOF, which results in a phase space description of the bath DOF while retaining the operator characters of the subsystem operators (which act in the Hilbert space of the subsystem). This mixed quantum-classical evolution equation can be obtained after truncating the quantum Liouville equation (in the partial Wigner representation) at linear order in the smallness parameter $\sqrt{m/M}$, where m and M denote the masses of the subsystem and bath particles, respectively. Such a truncation is justified when the bath DOF are much heavier than the subsystem DOF. For example, the QCLE can be used to model the formation/breaking of bonds (which involve a rearrangement of electrons) in a molecule surrounded by a solvent. In this case, key electronic DOF associated with the bond would be treated quantum mechanically, while the remaining DOF in the system would be treated classically.

Equation 2.5 evolves the density operator in time (i.e., Schrödinger picture), but in many cases it is more convenient to evolve an operator (i.e., Heisenberg picture). In this case, the QCLE is given by

$$\frac{d}{dt}\hat{O}_W(R,P,t) = \frac{i}{\hbar}\left[\hat{H}_W, \hat{O}_W(t)\right] - \frac{1}{2}\left(\{\hat{H}_W, \hat{O}_W(t\} - \{\hat{O}_W(t), \hat{H}_W\}\right). \qquad (2.6)$$

It should be noted that this equation has the same form as Eq. 2.4, except that the RHS differs by a factor of -1.

The QCLE may be expressed in terms of the quantum-classical Liouville operator, $i\hat{\mathcal{L}}$, defined by

$$\frac{\partial}{\partial t}\hat{\rho}_W(R,P,t) \equiv -i\hat{\mathcal{L}}\hat{\rho}_W(t). \qquad (2.7)$$

In this form, one sees that the formal solution of the QCLE is

$$\hat{\rho}_W(R,P,t) = e^{-i\hat{\mathcal{L}}t}\hat{\rho}_W(R,P,0). \qquad (2.8)$$

In practice, it is not easy to find a numerical solution. When the QCLE is cast in the adiabatic basis, one can solve it in terms of an ensemble of surface-hopping trajectories using the sequential short-time propagation (SSTP) [67, 68] or Trotter-based quantum-classical (TBQC) algorithms [69] after the momentum jump approximation is made [68, 74]. According to these algorithms, the classical DOF can hop between different adiabatic PESs, including the averages of two adiabatic PESs. It is the hops to and from these average surfaces that lead to the decoherence of the quantum subsystem, an important property that is not rigorously accounted for in FSSH [32, 46, 171] (as the jumps occur only between single adiabatic PESs). Both SSTP and TBQC have been shown to provide accurate solutions of the QCLE (with TBQC being somewhat more accurate than SSTP) for a number of relatively simple systems. While these solutions are rather accurate, these algorithms are restricted to relatively short times on the order of hundreds of femtoseconds, i.e., beyond these times the solutions become numerically unstable. This is due to the rapid growth of statistical weights (attached to each trajectory) associated with the Monte Carlo sampling of nonadiabatic transitions between the various adiabatic PESs involved in the dynamics. As a result, extremely large ensembles of trajectories are required to obtain converged solutions at longer times, making these solutions prohibitively expensive for simulating long time dynamics. Thus, the development of more efficient methods of solving the QCLE is an active area of research. One way to accomplish this is by developing more approximate solutions. In the following two sections, two such solutions are described, viz., PBME and FBTS.

2.3 Poisson Bracket Mapping Equation

2.3.1 Derivation of the PBME

The starting point to derive the Poisson Bracket Mapping Equation (PBME) solution [70] is to cast the QCLE in the mapping basis [79, 82, 172–174]. In this approach, the states of the quantum subsystem are ultimately exactly mapped onto a set of continuous variables. To accomplish this, one first maps the N level quantum subsystem onto a set of N quantum harmonic oscillators, such that the mapped wave function is a product of harmonic oscillator wave functions. The harmonic oscillator wave functions are restricted to be in their ground states, with the exception of the λ^{th} oscillator (to which the λ^{th} subsystem state was mapped) which is in its first excited state, i.e., $|\lambda\rangle \rightarrow |m_\lambda\rangle = |0_1, ...1_\lambda, ...0_N\rangle$. The $\{|\lambda\rangle\}$ states form the subsystem basis, which are the solutions of the eigenvalue problem, $\hat{h}_s|\lambda\rangle = \epsilon_\lambda|\lambda\rangle$, where $\hat{h}_s$ is the subsystem Hamiltonian given by

$$\hat{h}_s = \frac{\hat{p}^2}{2m} + \hat{V}(\hat{r}). \tag{2.9}$$

In the subsystem and mapping bases, the matrix elements of an operator may be written as $O_W^{\lambda\lambda'} = \langle\lambda|\hat{O}_W|\lambda'\rangle = \langle m_\lambda|\hat{O}_m|m_{\lambda'}\rangle$. In the second equality, the mapping analogue of an operator is defined as

$$\hat{O}_m(R,P) = \sum_{\lambda\lambda'} \hat{O}_W^{\lambda\lambda'}(R,P)\hat{a}_\lambda^\dagger \hat{a}_{\lambda'}, \tag{2.10}$$

where the mapping annihilation and creation operators are given by

$$\hat{a}_\lambda = \sqrt{\frac{1}{2\hbar}}(\hat{r}_\lambda + i\hat{p}_\lambda), \quad \hat{a}_\lambda^\dagger = \sqrt{\frac{1}{2\hbar}}(\hat{r}_\lambda - i\hat{p}_\lambda), \tag{2.11}$$

and satisfy the commutation relation $\left[\hat{a}_\lambda, \hat{a}_{\lambda'}^\dagger\right] = \delta_{\lambda,\lambda'}$.

At this point, one can represent the QCLE (Eq. 2.7) in the subsystem basis to yield

$$\frac{\partial}{\partial t}\langle\lambda|\hat{\rho}_W(R,P,t)|\lambda'\rangle = -i\langle\lambda|\hat{\mathcal{L}}\hat{\rho}_W(t)|\lambda'\rangle. \tag{2.12}$$

Owing to the equivalence between matrix elements in the subsystem and the mapping basis, this equation can also be expressed as

$$\frac{\partial}{\partial t}\langle m_\lambda|\hat{\rho}_m(R,P,t)|m_{\lambda'}\rangle = -i\langle m_\lambda|\hat{\mathcal{L}}_m\hat{\rho}_m(t)|m_{\lambda'}\rangle. \tag{2.13}$$

Thus, the mapping analogue of the QCLE is

$$\frac{\partial}{\partial t}\hat{\rho}_m(R,P,t) = -i\hat{\mathcal{L}}_m\hat{\rho}_m(t). \tag{2.14}$$

To achieve a continuous phase space representation of the subsystem DOF, one performs a Wigner transform over the subsystem DOF of Eq. 2.14:

$$\begin{aligned}\frac{\partial}{\partial t}\rho_m(x,X,t) = &-\frac{2}{\hbar}H_m \sin\left(\frac{\hbar\Lambda_m}{2}\right)\rho_m(t)\\ &+\frac{\partial H_m}{\partial R}\cos\left(\frac{\hbar\Lambda_m}{2}\right)\cdot\frac{\partial\rho_m(t)}{\partial P} - \frac{P}{M}\cdot\frac{\partial\rho_m(t)}{\partial R},\end{aligned} \tag{2.15}$$

where $x = (r, p)$ are the mapping variables of the quantum subsystem, $X = (R, P)$ are the positions and momenta of the environmental DOF, $\Lambda_m = \overleftarrow{\nabla}_p \cdot \overrightarrow{\nabla}_r - \overleftarrow{\nabla}_r \cdot \overrightarrow{\nabla}_p$ (where the arrows indicate the direction in which the gradient operators act), and the mapping Hamiltonian, H_m, is given by

$$H_m(x,X) = \frac{P^2}{2M} + V(R) + \frac{h^{\lambda\lambda'}}{2\hbar}(r_\lambda r_{\lambda'} + p_\lambda p_{\lambda'} - \hbar\delta_{\lambda,\lambda'}), \tag{2.16}$$

with $h^{\lambda\lambda'} = \langle\lambda|\hat{h}_s + \hat{V}_c(\hat{r},R)|\lambda'\rangle$. In this representation, the mapping analogue of any operator $\hat{O}_W(X)$ is given by

$$O_m(x,X) = \sum_{\lambda\lambda'} O_W^{\lambda\lambda'}(X)c_{\lambda\lambda'}(x), \tag{2.17}$$

where

$$c_{\lambda\lambda'}(x) = \frac{1}{2\hbar}[r_\lambda r_{\lambda'} + p_\lambda p_{\lambda'} + i(r_\lambda p_{\lambda'} - r_{\lambda'}p_\lambda) - \hbar\delta_{\lambda\lambda'}]. \tag{2.18}$$

Given the following relations involving any O_m,

$$H_m\Lambda_m O_m = \frac{1}{\hbar}\sum_{\lambda\lambda'} h^{\lambda\lambda'}\left(p_\lambda\frac{\partial}{\partial r_{\lambda'}} - r_\lambda\frac{\partial}{\partial p_{\lambda'}}\right)O_m, \tag{2.19}$$

$$H_m\Lambda_m^2 O_m = \frac{1}{\hbar}\sum_{\lambda\lambda'} h^{\lambda\lambda'}\left(\frac{\partial}{\partial r_{\lambda'}}\frac{\partial}{\partial r_\lambda} + \frac{\partial}{\partial p_{\lambda'}}\frac{\partial}{\partial p_\lambda}\right)O_m, \tag{2.20}$$

$$H_m\Lambda_m^n O_m = 0 \quad \text{for } n \geq 3 \tag{2.21}$$

it is possible to show that the QCLE in the mapping basis becomes

$$\begin{aligned}\frac{\partial}{\partial t}\rho_m(x,X,t) = \; & \frac{1}{\hbar}\sum_{\lambda\lambda'} h^{\lambda\lambda'}\left(r_\lambda \frac{\partial}{\partial p_{\lambda'}} - p_\lambda \frac{\partial}{\partial r_{\lambda'}}\right)\rho_m(t) \\ & + \left(\frac{\partial H_m}{\partial R}\frac{\partial}{\partial P} - \frac{P}{M}\frac{\partial}{\partial R}\right)\rho_m(t) \\ & - \frac{\hbar}{8}\sum_{\lambda\lambda'}\frac{\partial h^{\lambda\lambda'}}{\partial R}\left(\frac{\partial}{\partial r_{\lambda'}}\frac{\partial}{\partial r_\lambda} + \frac{\partial}{\partial p_{\lambda'}}\frac{\partial}{\partial p_\lambda}\right)\frac{\partial}{\partial P}\rho_m(t). \end{aligned} \tag{2.22}$$

This equation is composed of three terms: the first one describes the evolution of the quantum subsystem in the mapping phase space, the second term describes the evolution of the environmental DOF with forces that depend on the mapping variables, and the third term represents the higher order correlations between the quantum subsystem and its environment. Finally, noting that the first two terms correspond to a Poisson bracket in the mapping-bath phase space of the system, Eq. 2.22 can be rewritten in the following compact way:

$$\begin{aligned}\frac{\partial}{\partial t}\rho_m(x,X,t) = & \{H_m,\rho_m\}_{x,X} - \frac{\hbar}{8}\sum_{\lambda\lambda'}\frac{\partial h^{\lambda\lambda'}}{\partial R}\left(\frac{\partial}{\partial r_{\lambda'}}\frac{\partial}{\partial r_\lambda} + \frac{\partial}{\partial p_{\lambda'}}\frac{\partial}{\partial p_\lambda}\right)\frac{\partial}{\partial P}\rho_m(t) \\ \equiv & \left(-i\mathcal{L}_m^0 - i\mathcal{L}_m'\right)\rho_m(t). \end{aligned} \tag{2.23}$$

The operator $i\mathcal{L}_m^0$ gives rise to the Poisson bracket, which generates a classical-like evolution of the subsystem and bath DOF in terms independent Newtonian trajectories. The force field that the bath DOF experience depends on the matrix elements of the coupling potential, which change continuously as the mapping variables evolve. The operator $i\mathcal{L}_m'$, which contains higher order derivatives, is more complex because it generates "entanglement" between trajectories; thus, its effect can only be accounted for by generating an ensemble of entangled trajectories [71]. It should be noted that the mapping QCLE can be derived for an operator using the same procedure, yielding a RHS that differs by a factor of -1 from that in Eq. 2.23.

Because no approximation has been made to arrive at Eq. 2.22, the *mapping* QCLE is equivalent to the QCLE. However, the complex nature of the $i\mathcal{L}'_m$ term greatly complicates the solution of Eq. 2.22 and, therefore, one conceivable approximation is to simply drop this term. After doing so, one arrives at the PBME:

$$\frac{\partial}{\partial t}\rho_m(x, X, t) \approx -i\mathcal{L}^0_m \rho_m(t) = \{H_m, \rho_m(t)\}_{x,X}. \tag{2.24}$$

The resulting equation now only contains a Poisson bracket on its RHS and, thus, can be solved using the method of characteristics. This gives rise to the following set of ordinary differential equations: [70, 78]

$$\begin{aligned}
\frac{dr_\lambda(t)}{dt} &= \frac{\partial H_m}{\partial p_\lambda} = \frac{1}{\hbar}\sum_{\lambda'} h_{\lambda\lambda'}\left(R(t)\right) p_{\lambda'}(t), \\
\frac{dp_\lambda(t)}{dt} &= -\frac{\partial H_m}{\partial r_\lambda} = -\frac{1}{\hbar}\sum_{\lambda'} h_{\lambda\lambda'}\left(R(t)\right) r_{\lambda'}(t), \\
\frac{dR(t)}{dt} &= \frac{\partial H_m}{\partial P(t)} = \frac{P(t)}{M}, \ \frac{dP(t)}{dt} = -\frac{\partial H_m}{\partial R(t)}.
\end{aligned} \tag{2.25}$$

As can be seen, Eqs. 2.25 are Newtonian equations of motion for both the quantum mapping and classical phase space variables.

In the mapping formalism, one can show that the expectation value of a time-dependent operator is given by[70, 78]

$$\overline{O(t)} = \int dx dX O_m(x, X, t)\tilde{\rho}_m(x, X), \tag{2.26}$$

where

$$\tilde{\rho}_m(x, X) = \frac{1}{(2\pi\hbar)^n} \sum_{\lambda\lambda'} g_{\lambda\lambda'}(x) \rho_W^{\lambda'\lambda}(X), \tag{2.27}$$

and

$$g_{\lambda\lambda'}(x) = \frac{2^{n+1}}{\hbar} e^{-x^2/\hbar} [r_\lambda r_{\lambda'} - i(r_\lambda p_{\lambda'} - r_{\lambda'} p_\lambda) + p_\lambda p_{\lambda'} - \frac{\hbar}{2}\delta_{\lambda\lambda'}]. \tag{2.28}$$

2.3.2 Instabilities in PBME Dynamics

Instabilities in PBME dynamics can arise due to the form of the last term of H_m in Eq. 2.16. More specifically, the potential can "invert" if this term becomes negative. Kelly et al. [71] proposed a way to partially tame these instabilities by considering an alternative (yet equivalent) form of H_m, which will now be discussed.

It is possible to arrive at an equivalent form of an operator, as long as it is confined to the physical mapping space. Starting from the fact that

$$\langle m_\lambda | \sum_\nu \hat{a}_\nu^\dagger \hat{a}_\nu | m_{\lambda'} \rangle = \langle m_\lambda | m_{\lambda'} \rangle, \tag{2.29}$$

where $\sum_\nu \hat{a}_\nu^\dagger \hat{a}_\nu$ is an identity operator in the mapping space, one can use the definition of $g_{\lambda\lambda'}$ (see Eq. 2.28) to write the right side of Eq. 2.29 as,

$$\langle m_\lambda | m_{\lambda'} \rangle = \int dx \, g_{\lambda\lambda'}(x). \tag{2.30}$$

Inserting complete sets of coordinate states and taking Wigner transforms of the left side of Eq. 2.29, leads to the following equivalent form of Eq. 2.29:

$$\int dx \, g_{\lambda\lambda'}(x) \sum_\nu c_{\nu\nu}(x) = \int dx \, g_{\lambda\lambda'}(x). \tag{2.31}$$

This form reveals that

$$\sum_{\lambda} c_{\lambda\lambda}(x) = \frac{1}{2\hbar}\sum_{\lambda}(r_{\lambda}^2 + p_{\lambda}^2 - \hbar) = 1, \tag{2.32}$$

as long as it lies under the $g_{\lambda\lambda'}(x)$ integral. This identity has consequences on the form of operators in the mapping basis. In the subsystem basis, one may always write the matrix elements of an operator as a sum of its trace and traceless contributions:

$$B_W^{\lambda\lambda'}(X) = \delta_{\lambda\lambda'}\text{Tr }(B_W)/N + \overline{B}_W^{\lambda\lambda'}(X), \tag{2.33}$$

where $\overline{B}_W^{\lambda\lambda'}$ denotes the traceless contribution. If one then inserts this result into Eq. 2.17, one finds the following expression for B_m:

$$B_m(x, X) = \text{Tr }(B_W)/N + \sum_{\lambda\lambda'} \overline{B}_W^{\lambda\lambda'}(X)\bar{c}_{\lambda\lambda'}(x), \tag{2.34}$$

where $\bar{c}_{\lambda\lambda'}(x)$ is the traceless version of $c_{\lambda\lambda'}(x)$ in Eq. 2.18, and has the following form:

$$\bar{c}_{\lambda\lambda'}(x) = \frac{1}{2\hbar}\left[r_{\lambda}r_{\lambda'} + p_{\lambda}p_{\lambda'} + i(r_{\lambda}p_{\lambda'} - r_{\lambda'}p_{\lambda})\right]. \tag{2.35}$$

Equation 2.34 holds only as long as B_m lies under a $g_{\lambda\lambda'}$ integral, i.e., is projected onto the physical space. It should be emphasized that both forms of B_m are equivalent, as long as the operator lies under the $g_{\lambda\lambda'}$ integral.

One can express H_m in a similar way (assuming that it lies under the $g_{\lambda\lambda'}$ integral):

$$H_m(x, X) = \frac{P^2}{2M} + V_0(R) + \frac{1}{2\hbar}\sum_{\lambda\lambda'} \overline{h}^{\lambda\lambda'}(R)(r_{\lambda}r_{\lambda'} + p_{\lambda}p_{\lambda'}), \tag{2.36}$$

where $\overline{h}^{\lambda\lambda'}$ is the traceless version of $h^{\lambda\lambda'}$, and $V_0(R) = V(R) + \text{Tr }(h)/N$. The two forms of

H_m will generate equivalent results under QCLE dynamics, as QCLE dynamics restricts the system to the physical space [71]. However, the results generated by these two forms will not be equivalent under PBME dynamics (an approximation to QCLE dynamics) because it takes the system out of the physical space. Thus, dynamical instabilities can arise that depend on the form of H_m. Previous studies have shown that it is possible to minimize these instabilities when the form of H_m in Eq. 2.36 is used. [71] Nonetheless, even if the occurrence of inverted potentials is suppressed at early times, they may still arise at later times due to the approximate nature of PBME dynamics.

2.4 Forward-Backward Trajectory Solution

We now present a summary of the derivation of the Forward-Backward Trajectory Solution (FBTS), another approximate solution of the QCLE (see Refs. [40], [72], and [86] for all the details). To arrive at this solution, one first writes the QCLE (i.e., Eq. 2.5) in terms of forward and backward operators [175]:

$$\frac{\partial}{\partial t}\hat{\rho}_W(X,t) = -\frac{i}{\hbar}\left(\overrightarrow{\mathcal{H}}_\Lambda \hat{\rho}_W(t) - \hat{\rho}_W(t)\overleftarrow{\mathcal{H}}_\Lambda\right), \tag{2.37}$$

where the forward operator

$$\overrightarrow{\mathcal{H}}_\Lambda = \hat{H}_W\left(1+\frac{\hbar\Lambda}{2i}\right), \tag{2.38}$$

and the backward operator

$$\overleftarrow{\mathcal{H}}_\Lambda = \left(1+\frac{\hbar\Lambda}{2i}\right)\hat{H}_W. \tag{2.39}$$

The formal solution of Eq. 2.37 may be written as

$$\hat{\rho}_W(X,t) = \mathcal{S}\left(e^{-i\overrightarrow{\mathcal{H}}_\Lambda t/\hbar}\hat{\rho}_W(X)e^{i\overleftarrow{\mathcal{H}}_\Lambda t/\hbar}\right), \tag{2.40}$$

where $\mathcal{S}$ is an operator that specifies the order in which the forward and backward evolution operators act on $\hat{\rho}_W(X)$. Similarly, for an arbitrary operator $\hat{A}(X)$, the solution can be written in the same form (except for a change in sign):

$$\hat{A}_W(X,t) = \mathcal{S}\left(e^{i\overrightarrow{\mathcal{H}}_\Lambda t/\hbar}\hat{A}_W(X)e^{-i\overleftarrow{\mathcal{H}}_\Lambda t/\hbar}\right). \tag{2.41}$$

This equation is the starting point for the derivation of the FBTS.

The next step involves representing $\hat{A}_W(X,t)$ in the mapping basis (as done in the previous section):

$$\begin{aligned}\hat{A}_W^{\lambda\lambda'}(X,t) &= \langle\lambda|\mathcal{S}\left(e^{i\overrightarrow{\mathcal{H}}_\Lambda t/\hbar}\hat{A}_W(X)e^{-i\overleftarrow{\mathcal{H}}_\Lambda t/\hbar}\right)|\lambda'\rangle \\ &= \langle m_\lambda|\mathcal{S}\left(e^{i\overrightarrow{\mathcal{H}}_{\Lambda,m} t/\hbar}\hat{A}_m(X)e^{-i\overleftarrow{\mathcal{H}}_{\Lambda,m} t/\hbar}\right)|m_{\lambda'}\rangle.\end{aligned} \tag{2.42}$$

Thus, we see that the formal solution of the QCLE in the mapping basis is

$$\hat{A}_m(X,t) = \mathcal{S}\left(e^{i\overrightarrow{\mathcal{H}}_{\Lambda,m} t/\hbar}\hat{A}_m(X)e^{-i\overleftarrow{\mathcal{H}}_{\Lambda,m} t/\hbar}\right). \tag{2.43}$$

At this point, instead of applying a Wigner transform over the mapping space, a coherent state basis $|z\rangle = |z_1, z_2 \dots z_N\rangle$ is introduced in the mapping space. This set of coherent states has eigenvalues $z = (q + ip)/\sqrt{2\hbar}$, where $q = (q_1, \dots, q_N)$ and $p = (p_1, \dots, p_N)$ are the average positions and momenta of the harmonic oscillators in state $|z\rangle$, respectively, e.g., $q = \langle z|\hat{q}|z\rangle$. In this basis, the resolution of identity is given by

$$I = \int \frac{d^2 z}{\pi^N}|z\rangle\langle z|. \tag{2.44}$$

One can then express the forward and backward evolution operators in Eq. 2.42 as a concatenation of M short-time evolution segments with $\Delta t_i = t_i - t_{i-1} = \tau$ (for all i with

$t_0 = 0$, $t_M = t$, and $M\tau = t$), where for each segment two sets of coherent state variables are introduced using the resolution of identity. In this way, the matrix elements of $\hat{A}_W(X,t)$ may be expressed in terms of the coherent state basis as [40, 72]

$$\begin{aligned} A_W^{\lambda\lambda'}(X,t) &= \sum_{\mu\mu'} \int \prod_{i=1}^{M} \frac{d^2 z_i}{\pi^n} \frac{d^2 z_i'}{\pi^n} \langle m_\lambda | z_1 \rangle \langle z_1' | m_{\lambda'} \rangle \\ &\quad \times \Big(\langle z_1(t_1) | z_2 \rangle e^{i\Delta t_2 \mathcal{L}_e(X_{t_1}, z_2, z_2')/2} \big(\langle z_2 | \ldots \\ &\quad \times A_W^{\mu\mu'}(X_{t_1}) \ldots | z_2' \rangle \Big) \langle z_2' | z_1'(t_1) \rangle \Big) . \end{aligned} \tag{2.45}$$

Here, the effective evolution operator $i\mathcal{L}_e(X,z,z')$ is given by

$$i\mathcal{L}_e(X,z,z') = \frac{P}{M} \cdot \frac{\partial}{\partial R} - \frac{\partial V_e(X,z,z')}{\partial R} \cdot \frac{\partial}{\partial P}, \tag{2.46}$$

where

$$V_e(X,z,z') = [V_{cl}(R,z) + V_{cl}(R,z')]/2, \tag{2.47}$$

and

$$V_{cl}(R,z) = V(R) - \mathrm{Tr}_s \hat{h}(R) + \sum_{\lambda\lambda'} V_c^{\lambda\lambda'}(R) z_\lambda^* z_{\lambda'}. \tag{2.48}$$

In contrast to the actions of the forward and backward operators, this single operator acts according to $e^{i\mathcal{L}_e(X,z,z')\tau} \hat{A}_W(X) = \hat{A}_W(X_\tau)$.

At this point, one has to make an approximation to arrive at a continuous trajectory picture of the dynamics. If the phase space coordinates of the two coherent states involved in the overlap integrals in Eq. 2.45 are substantially different, then one can assume that $\langle z_1(t_1) | z_2 \rangle \approx \pi^N \delta(z_2 - z_1(t_1))$ and $\langle z_2' | z_1'(t_1) \rangle \approx \pi^N \delta(z_2' - z_1'(t_1))$, for example. Next, integrating over the coherent state variables z_i and z_i' for $\{i, i'\} \geq 2$ and applying the effective evolution operator leads to

$$\begin{aligned} A_W^{\lambda\lambda'}(X,t) &= \sum_{\mu\mu'} \int \frac{d^2 z_1}{\pi^N} \frac{d^2 z_1'}{\pi^N} \langle m_\lambda | z_1 \rangle \langle z_1' | m_{\lambda'} \rangle \\ &\quad \times \Big(\langle z_1(t_1) | m_\mu \rangle A_W^{\mu\mu'}(X_t) \langle m_{\mu'} | z_1'(t) \rangle \Big) . \end{aligned} \tag{2.49}$$

Finally, evaluating the overlap integrals using $\langle m_\lambda | z \rangle = z_\lambda e^{-|z|^2/2}$, expressing the above equation in terms of $x = (q,p)$ variables, and using the fact that $\sum_\nu (q_\nu^2 + p_\nu^2)$ is conserved under coherent state dynamics, gives

$$\begin{aligned} A_W^{\lambda\lambda'}(X,t) &= \sum_{\mu\mu'} \int dx dx' \phi(x) \phi(x') \\ &\quad \times \frac{1}{2\hbar} (q_\lambda + i p_\lambda)(q'_{\lambda'} - i p'_{\lambda'}) A_W^{\mu\mu'}(X_t) \\ &\quad \times \frac{1}{2\hbar} (q_\mu(t) - i p_\mu(t))(q'_{\mu'}(t) + i p'_{\mu'}(t)), \end{aligned} \tag{2.50}$$

where $\phi(x) = (2\pi\hbar)^{-N} e^{-\sum_\nu (q_\nu^2 + p_\nu^2)/2\hbar}$. The coupled evolution of the environmental and coherent state variables is dictated by the following set of coupled differential equations:

$$\begin{aligned} &\frac{dq_\mu}{dt} = \frac{\partial H_{cl}(X,x)}{\partial p_\mu}, \quad \frac{dp_\mu}{dt} = -\frac{\partial H_{cl}(X,x)}{\partial q_\mu}, \\ &\frac{dq_{\mu'}}{dt} = \frac{\partial H_{cl}(X,x')}{\partial p_{\mu'}}, \quad \frac{dp_{\mu'}}{dt} = -\frac{\partial H_{cl}(X,x')}{\partial q_{\mu'}}, \\ &\frac{dR}{dt} = \frac{P}{M}, \quad \frac{dP}{dt} = -\frac{\partial H_e(X,x,x')}{\partial R}, \end{aligned} \tag{2.51}$$

where

$$H_e(X,x,x') = \frac{1}{2} [H_{cl}(X,x) + H_{cl}(X,x')], \tag{2.52}$$

with

$$H_{cl}(X,x) = H_e(X) - \mathrm{Tr}_s \hat{h}(R) + \frac{1}{2\hbar} \sum_{\lambda\lambda'} h^{\lambda\lambda'} (q_{\lambda'} q_\lambda + p_\lambda p_{\lambda'}). \tag{2.53}$$

Solving these equations yields a simple dynamics, in which the forward and backward trajectories of the coherent state variables are propagated forward in time, while the environmental coordinates evolve on a mean potential that depends on these two sets of trajectories. Finally, the expectation value of an observable $\hat{A}(t)$ is given by

$$\overline{A(t)} = \sum_{\lambda\lambda'} \int dX A_W^{\lambda\lambda'}(X,t)\rho_W^{\lambda'\lambda}(X), \tag{2.54}$$

where $A_W^{\lambda\lambda'}(X,t)$ is given by Eq. (2.50).

2.5 Numerical Integration of Equations of Motion

Standard molecular dynamics integrators can be used to solve the PBME and FBTS equations of motion (Eqs. 2.25 and 2.51, respectively). For instance, one may use a velocity-Verlet-type algorithm for integrating the PBME equations of motion as follows:

$$\begin{aligned}
P(\Delta t/2) &= P(0) + \frac{\Delta t}{2}\mathcal{F}(0) \\
p_\lambda(\Delta t/2) &= p_\lambda(0) - \frac{\Delta t}{2\hbar}\sum_{\lambda'} h^{\lambda\lambda'}(R(0))r_{\lambda'}(0) \\
R(\Delta t) &= R(0) + \Delta t \frac{P(\Delta t/2)}{M} \\
r_\lambda(\Delta t) &= r_\lambda(0) + \frac{\Delta t}{\hbar}\sum_{\lambda'} h^{\lambda\lambda'}(R(\Delta t))p_{\lambda'}(\Delta t/2) \\
p_\lambda(\Delta t) &= p_\lambda(\Delta t/2) - \frac{\Delta t}{2\hbar}\sum_{\lambda'} h^{\lambda\lambda'}(R(\Delta t))r_{\lambda'}(\Delta t) \\
P(\Delta t) &= P(\Delta t/2) + \frac{\Delta t}{2}\mathcal{F}(\Delta t),
\end{aligned} \tag{2.55}$$

where the PBME force is given by

$$\mathcal{F} = -\frac{\partial H_m}{\partial R}. \tag{2.56}$$

The algorithm for integrating the FBTS equations of motion is similar to that in Eq. 2.55, with the *one* set of mapping variables replaced by now *two* sets of coherent state variables and the FBTS force is given by

$$\mathcal{F} = -\frac{\partial H_e}{\partial R}. \tag{2.57}$$

It should be noted that the classical variables typically evolve on a much longer time scale than the quantum subsystem variables. Therefore, very small time steps must be used to resolve the rapid fluctuations in the quantum variables and to conserve energy. For the systems studied in this thesis, we have found that this integrator performs best with time steps of $\Delta t \approx 10^{-2}$ to 10^{-1} fs, which can make it computationally expensive to simulate large systems.

To alleviate this problem, Kelly et. al[71] designed an integrator which admits larger time steps by taking advantage of the separation of time scales between the quantum and classical DOF and using the exact solution of the subsystem equations of motion with the classical positions held fixed. This integration algorithm goes as follows:

$$\begin{aligned}
R(\Delta t/2) &= R(0) + \frac{\Delta t}{2}\frac{P(\Delta t/2)}{M} \\
r_\lambda(\Delta t) &= \sum_{\mu\lambda'} C_{\lambda\mu}(R) C^{-1}_{\mu\lambda'}(R)[\cos(\omega_\mu \Delta t) r_{\lambda'}(0) + \sin(\omega_\mu \Delta t) p_{\lambda'}(0)] \\
p_\lambda(\Delta t) &= \sum_{\mu\lambda'} C_{\lambda\mu}(R) C^{-1}_{\mu\lambda'}(R)[\cos(\omega_\mu \Delta t) p_{\lambda'}(0) - \sin(\omega_\mu \Delta t) r_{\lambda'}(0)] \\
P(\Delta t) &= P(0) - \frac{\partial V_0(R)}{\partial R}\Delta t - \sum_\lambda \frac{\Delta t}{2\hbar}\frac{\partial E_\lambda(R)}{\partial R}(\tilde{r}_\lambda(0)^2 + \tilde{p}_\lambda(0)^2 - 1) \\
R(\Delta t) &= R(\Delta t/2) + \frac{\Delta t}{2}\frac{P(\Delta t)}{M},
\end{aligned} \tag{2.58}$$

where $V_0(R) = V(R) + (\mathrm{Tr}\ \hat{h})/N$, the columns of the matrix C contain the eigenvectors of the traceless $\overline{h}(R)$, E_μ are the eigenvalues of $\overline{h}(R)$, $\omega_\mu(R) = E_\mu(R)/\hbar$, and the tilded mapping variables are given by

$$\tilde{r}_\lambda = C^{-1}_{\lambda\lambda'} r_{\lambda'}, \quad \tilde{p}_\lambda = C^{-1}_{\lambda\lambda'} p_{\lambda'}. \tag{2.59}$$

For the systems we have studied, this integrator can use time steps that are ≈ 20 times larger than those used by the velocity-Verlet-type algorithm. Hence, this integrator could prove to be useful for simulating larger systems.

To conclude this chapter, it is important to mention that both PBME and FBTS have been previously applied to a variety of models, yielding reliable results mainly under conditions of weak subsystem–bath coupling [38, 71, 72, 78, 83, 179]. The validity of these approximations will be further considered over the course of the following three chapters, where three new models with varying subsystem–bath coupling strengths are investigated.

Chapter 3

Simulation of Nonlinear Optical Signals via Approximate Solutions of the Quantum-Classical Liouville Equation: Application to the Pump-Probe Spectroscopy of a Condensed Phase Electron Transfer Reaction

3.1 Abstract

The equation-of-motion phase-matching approach provides an efficient way for calculating a system's time-dependent polarization in any phase-matching direction subject to weak laser fields of arbitrary shape. Within this approach, we employ two approximate solutions of the quantum-classical Liouville equation (QCLE), for simulating the laser-induced dynamics of a quantum subsystem in a classical environment. We illustrate this approach by calculating

the transient absorption (TA) pump-probe signal in a model photo-induced electron transfer (PIET) reaction. The results are found to be in reasonable agreement with the exact results, which is promising for applications to realistic systems.

3.2 Introduction

Nonlinear spectroscopies constitute a powerful set of techniques which can yield detailed information about molecular structure and dynamics [109, 176, 177]. However, the information contained in nonlinear signals is often manifested in indirect ways, making their interpretation difficult. Theory and simulation have proven to be indispensable in understanding these signals, but they must be both accurate for reliable interpretations and efficient for tackling systems with many degrees of freedom (DOF).

Theoretical methods for calculating nonlinear spectra fall into two main categories: perturbative and nonperturbative approaches. In the perturbative approach, a desired spectroscopic signal may be obtained directly via calculations of optical response functions (ORFs), which capture the system's field-free dynamics at a particular order of the applied field in terms of multi-time dipole moment correlation functions. Unfortunately, exact quantum mechanical calculations of ORFs are only feasible in the case of very simple models [99, 100], so as the complexity of the system grows, ORFs can no longer be efficiently evaluated even using some semiclassical treatments [101–108]. Mixed quantum-classical methods, which are based on treating a small subset of photo-active DOF (i.e., the chromophore) quantum mechanically while the remaining photo-inactive DOF (i.e., the bath) are treated in a classical-like manner, represent attractive alternatives for computing ORFs[109–112]. Such applications have often been based on equilibrium classical molecular dynamics simulations of the photo-inactive DOF on the potential energy surface (PES) corresponding to the chromophore's ground state. In order to tackle situations where nonequilibrium solvation dynamics on and nonradiative nonadiabatic transitions between multiple PESs are important, methods based on the QCLE in the adiabatic basis have been developed [111, 112]. In the nonperturbative approach, one calculates the total polarization of a system by simulating its dynamics subject to the applied radiation fields, and then extracts the contribution corresponding to a spectroscopic signal using its specific phase-matching condition [113]. Methods based on this approach have proven to be viable options for calculating a variety of nonlinear spectroscopic signals in model systems, but in the case of complex systems, the calculations become computationally intensive since, in general, numerous simulations are needed to extract the desired signal [113–122].

More recently, the equation-of-motion phase-matching approach (EOM-PMA), which combines features of both perturbative and non-perturbative approaches, was developed by Gelin et al.[123, 124] EOM-PMA is capable of efficiently simulating the time-dependent polarization of a system in any phase-matching direction in response to weak laser fields of arbitrary shape and width. One of the highlights of this method is that it can incorporate any EOM for propagating the system's density matrix or dipole moment. Therefore, in principle, EOM-PMA can be coupled with a semiclassical or mixed quantum-classical dynamical method for tackling larger, complex systems.

In this Chapter, we take a mixed quantum-classical approach for evolving a quantum subsystem that interacts with N_p laser fields and is coupled to classical environment. Since photo-induced dynamics is inherently nonadiabatic in nature, it is important that the mixed quantum-classical method correctly describe the effect of the time-dependent fields on the photoactive quantum DOF and the coupling between the quantum and classical DOF. Here, we consider methods based on the QCLE because, in the adiabatic representation, they are capable of capturing nonequilibrium solvation dynamics on multiple adiabatic PESs, as well as both the radiative and non-radiative nonadiabatic transitions between them [83, 111, 112].

These features are particularly important when modeling the nonlinear spectra of systems that exhibit strong subsystem-bath coupling or whose spectra are inherently sensitive to the bath dynamics. In such cases, the ground- and excited-state PESs may be significantly different, and hence a ground-state adiabatic treatment of the dynamics may not be justified.

Unfortunately, in the case of complex systems, solving the QCLE in the adiabatic basis is computationally demanding due to the large number of trajectories required to average out the highly oscillatory terms which enter into the calculation of an observable [68]. Driven by the desire to develop more efficient algorithms for solving the QCLE, the mapping basis [23, 79, 80, 178] has been used to represent the discrete quantum DOF in the QCLE in terms of continuous variables, so that all DOF are represented as continuous variables [70, 71, 78]. If one neglects the higher order correlations between the subsystem and the bath, the QCLE in the mapping basis reduces to the Poisson Bracket Mapping Equation (PBME) [70, 78], which is a simple evolution equation that can be solved by propagating both the quantum and classical DOF under a Newtonian-like dynamics. Although the PBME has been shown to be accurate for some model systems [70, 78, 179], it can lead to instabilities for others [71, 83]. Recently, the mapping basis has been used as a starting point along with the coherent state basis [81] to derive another approximate solution of the QCLE in terms of forward-backward propagators [40]. The result is a set of equation of motions that retain the simplicity of PBME, with a better description of the nonadiabatic dynamics, at the cost of doubling the set of variables that describe the quantum DOF (to be propagated in forward and backward trajectories). This method, known as the forward-backward trajectory solution (FBTS), has been tested on a host of simple model systems including the two-level symmetric and asymmetric spin-boson models, exhibiting a range of agreements with the numerically exact quantum results from moderate to excellent [72].

To advance the testing of these techniques and the development of more efficient methods for simulating nonlinear optical signals, in this Chapter we present a way to compute the time-dependent nonlinear polarization of a system induced by N_p weak pulses, within the context of the EOM-PMA, using the PBME and FBTS approaches. In particular, we demonstrate its implementation for calculating the TA pump-probe signal in a three-state model of a condensed phase PIET reaction. Although more efficient methods for calculating pump-probe signals exist (which can even treat strong pump pulses) [180, 181], our aim here is to simply illustrate this general approach, using a pump-probe signal as an example, and then to compare our results to the numerically exact quantum results reported in Ref. [118] in order to probe the effectiveness of these implementations.

3.3 Mixed Quantum-Classical Liouville Evolution of a System Interacting with Multiple Laser Pulses

We start by considering a quantum subsystem driven by a classical electric field that is coupled to a classical environment, described by the following time-dependent Hamiltonian:

$$\begin{aligned}\hat{H}(t) &= \frac{\mathbf{P}^2}{2\mathbf{M}} + V_e(\mathbf{R}) + \frac{\hat{\mathbf{p}}^2}{2\mathbf{m}} + \hat{V}_s(\hat{\mathbf{q}}) + \hat{V}_c(\hat{\mathbf{q}},\mathbf{R}) + \hat{W}(\hat{\mathbf{q}},t) \equiv \hat{H}_M(\hat{\mathbf{q}},\hat{\mathbf{p}},\mathbf{R},\mathbf{P}) + \hat{W}(\hat{\mathbf{q}},t) \\ &\equiv H_e(\mathbf{R},\mathbf{P}) + \hat{h}_s(\hat{\mathbf{q}},\hat{\mathbf{p}}) + \hat{V}_c(\hat{\mathbf{q}},\mathbf{R}) + \hat{W}(\hat{\mathbf{q}},t) \\ &\equiv H_e(\mathbf{R},\mathbf{P}) + \hat{h}(\mathbf{R},t) \end{aligned} \tag{3.1}$$

where $\mathbf{m}$, $\hat{\mathbf{q}}$, and $\hat{\mathbf{p}}$ are the vectors of masses, positions, and momenta, respectively, of the n photoactive quantum DOF; $\mathbf{M}$, $\mathbf{R}$, and $\mathbf{P}$ are the vectors of masses, positions, and momenta, respectively, of the N photoinactive classical DOF; $\hat{H}_M = \hat{H} - \hat{W}$ is the material Hamiltonian; $H_e = \frac{\mathbf{P}^2}{2\mathbf{M}} + V_e$ and $\hat{h}_s = \frac{\hat{\mathbf{p}}^2}{2\mathbf{m}} + \hat{V}_s$ are the environment and subsystem Hamiltonians, respectively; $\hat{V}_c$ is the subystem-environment coupling potential energy and

$\hat{h} = \hat{h}_s + \hat{V}_c + \hat{W}$ [in what follows, operators are capped (e.g., $\hat{A}$) and all vectors except those corresponding to positions and momenta will be boldfaced (e.g., $\mathbf{A}$)]. The field-subsystem interaction term, $\hat{W}(\hat{q}, t)$, is assumed to be given by

$$\hat{W}(\hat{q}, t) = -\hat{\mu}\left(\hat{q}\right) \cdot \mathbf{E}\left(t\right), \tag{3.2}$$

where $\hat{\mu}(\hat{q})$ is the subsystem's dipole moment operator, and the incident electric field is expressed as a sum of N_p coherent laser pulses:

$$\mathbf{E}\left(t\right) = \sum_{\alpha=1}^{N_p} \mathbf{A}_\alpha f_\alpha\left(t - t_\alpha\right) \exp\left\{i\left[\mathbf{k}_\alpha \mathbf{r} - \omega_\alpha\left(t - t_\alpha\right)\right]\right\} + \text{c.c.} \tag{3.3}$$

where each laser pulse is characterized by its wave vector $\mathbf{k}_\alpha$, leading frequency ω_α, and pulse envelope $f_\alpha\left(t - t_\alpha\right)$, and $\mathbf{A}_\alpha$ is the product of the polarization vector and the overall amplitude of the pulse. The envelope function is taken to be a Gaussian centered at time t_α:

$$f_\alpha\left(t - t_\alpha\right) = \sqrt{\frac{4\ln 2}{\pi\tau_\alpha^2}} \exp\left(-4\ln 2 \frac{\left(t - t_\alpha\right)^2}{\tau_\alpha^2}\right), \tag{3.4}$$

where τ_α is the full-width at half-maximum of the pulse.

Our interest lies in the quantum-classical dynamics of an observable, which can be described in terms of the partial Wigner transform [170] of its corresponding operator, $\hat{A}(t)$, over the environmental DOF:

$$\hat{A}_W(X, t) = \int dZ e^{iP\cdot Z/\hbar} \langle R - Z/2|\hat{A}(t)|R + Z/2\rangle, \tag{3.5}$$

where $X = (R, P)$. The expectation value of an observable $\hat{A}_W$ is then given by

$$\overline{A(t)} = \text{Tr}_s \int dX \hat{A}_W(X, t) \hat{\rho}_W(X), \tag{3.6}$$

where Tr_s denotes a trace over the subsystem DOF and $\hat{\rho}_W$, the partial Wigner transform of the density operator, is given by:

$$\hat{\rho}_W(X) = \left(\frac{1}{2\pi\hbar}\right)^N \int dZ e^{iP\cdot Z/\hbar} \langle R - Z/2|\hat{\rho}|R + Z/2\rangle. \tag{3.7}$$

If $m/M \ll 1$, the quantum-classical Liouville equation (QCLE) can be used to accurately describe the dynamics of $\hat{A}_W(X,t)$ to first order in $\sqrt{m/M}$ [33, 182]:

$$\begin{aligned} \frac{\partial}{\partial t}\hat{A}_W(X,t) &= \frac{i}{\hbar}\left[\hat{H}_W\left(X,t\right), \hat{A}_W\left(X,t\right)\right] \\ &\quad -\frac{1}{2}\left(\left\{\hat{H}_W\left(X,t\right), \hat{A}_W\left(X,t\right)\right\} - \left\{\hat{A}_W\left(X,t\right), \hat{H}_W\left(X,t\right)\right\}\right). \end{aligned} \tag{3.8}$$

Here, $[\cdots]$ is the commutator and $\{\cdots\}$ is the Poisson bracket given by

$$\left\{\hat{A}_W\left(X,t\right), \hat{B}_W\left(X,t\right)\right\} = \hat{A}_W\left(X,t\right)\left(\overleftarrow{\nabla}_P \overrightarrow{\nabla}_R - \overleftarrow{\nabla}_R \overrightarrow{\nabla}_P\right)\hat{B}_W\left(X,t\right), \tag{3.9}$$

where $\overrightarrow{\nabla}_{R/P}$ and $\overleftarrow{\nabla}_{R/P}$ correspond to taking the gradient with respect to R/P of the term to the right and left, respectively.

3.3.1 Quantum-Classical Dynamics via the PBME Solution

In this section, we provide a summary of the main theoretical results leading to the PBME solution and for calculating expectation values of operators in the mapping basis. More details are provided in Refs. [70] and [78].

In the mapping basis, the QCLE takes the following form [70]:

$$\begin{aligned}
\frac{\partial}{\partial t} A_m(X,x,t) &= \frac{1}{\hbar}\sum_{\lambda\lambda'} h^{\lambda\lambda'}\left(p_\lambda \frac{\partial}{\partial r_{\lambda'}} - r_\lambda \frac{\partial}{\partial p_{\lambda'}}\right) A_m(t) + \left(\frac{P}{M}\frac{\partial}{\partial R} - \frac{\partial H_m}{\partial R}\frac{\partial}{\partial P}\right) A_m(t) \\
&\quad + \frac{\hbar}{8}\sum_{\lambda\lambda'} \frac{\partial h^{\lambda\lambda'}}{\partial R}\left(\frac{\partial}{\partial r_{\lambda'}}\frac{\partial}{\partial r_\lambda} + \frac{\partial}{\partial p_{\lambda'}}\frac{\partial}{\partial p_\lambda}\right)\frac{\partial}{\partial P} A_m(t) \\
&\equiv -\{H_m(t), A_m(t)\}_{X,x} \\
&\quad + \frac{\hbar}{8}\sum_{\lambda\lambda'} \frac{\partial h^{\lambda\lambda'}}{\partial R}\left(\frac{\partial}{\partial r_{\lambda'}}\frac{\partial}{\partial r_\lambda} + \frac{\partial}{\partial p_{\lambda'}}\frac{\partial}{\partial p_\lambda}\right)\frac{\partial}{\partial P} A_m(t),
\end{aligned} \tag{3.10}$$

where A_m, the mapping analogue of the operator $\hat{A}_W(X)$, is given by

$$A_m(x,X) = \sum_{\lambda\lambda'} A_W^{\lambda\lambda'}(X) c_{\lambda\lambda'}(x), \tag{3.11}$$

and $x = (r,p) = (r_1,\ldots,r_n,p_1,\ldots,p_n)$ denotes the positions and momenta of the subsystem mapping variables and the subscripts/superscripts $\lambda\lambda'$ denote a representation in the subsystem basis, $\{|\lambda\rangle; \lambda = 1,\ldots,n\}$, which is defined by the eigenvalue problem $\hat{h}_s|\lambda\rangle = \epsilon_\lambda|\lambda\rangle$. Here, $c_{\lambda\lambda'}(x)$ is given by [78]

$$c_{\lambda\lambda'}(x) = \frac{1}{2\hbar}[r_\lambda r_{\lambda'} + p_\lambda p_{\lambda'} + i(r_\lambda p_{\lambda'} - r_{\lambda'} p_\lambda) - \hbar\delta_{\lambda\lambda'}]. \tag{3.12}$$

As a result, the *mapping Hamiltonian* is given by

$$H_m(x,X) = H_e(X) + \frac{1}{2\hbar}\sum_{\lambda\lambda'} h^{\lambda\lambda'}(R,t)\left(r_\lambda r_{\lambda'} + p_\lambda p_{\lambda'} - \hbar\delta_{\lambda\lambda'}\right), \tag{3.13}$$

where

$$\begin{aligned}
h^{\lambda\lambda'}(R,t) &= \langle\lambda|\hat{p}^2/2m + \hat{V}_s(\hat{q}) + \hat{V}_c(\hat{q},R) + \hat{W}(\hat{q},t)|\lambda'\rangle \\
&= \epsilon_\lambda\delta_{\lambda\lambda'} + V_c^{\lambda\lambda'}(R) + W^{\lambda\lambda'}(t),
\end{aligned} \tag{3.14}$$

with $W^{\lambda\lambda'}(t) = -\hat{\mu}^{\lambda\lambda'} \cdot \mathbf{E}(t)$ and it has been assumed that $h^{\lambda\lambda'} = h^{\lambda'\lambda}$.

If the last term of Eq. (3.10) is dropped to arrive at the PBME, $A_m(t)$ may be obtained by solving the following set of Hamiltonian equations of motion [70]:

$$
\begin{aligned}
\frac{dr_\lambda}{dt} &= \frac{\partial H_m}{\partial p_\lambda} = \frac{1}{\hbar}\sum_{\lambda'} h_{\lambda\lambda'}\left(R(t),t\right)p_{\lambda'}(t) \\
\frac{dp_\lambda}{dt} &= -\frac{\partial H_m}{\partial r_\lambda} = -\frac{1}{\hbar}\sum_{\lambda'} h_{\lambda\lambda'}\left(R(t),t\right)r_{\lambda'}(t) \\
\frac{dR(t)}{dt} &= \frac{\partial H_m}{\partial P(t)} = \frac{P(t)}{M}, \ \frac{dP(t)}{dt} = -\frac{\partial H}{\partial R(t)}
\end{aligned}
\tag{3.15}
$$

Thus, the mapping and bath variables can be easily propagated in terms of Newtonian trajectories.

In the mapping basis, the expectation value of an observable $\hat{A}(t)$ may be written as[70]

$$
\overline{A(t)} = \int dxdX\, A_m(x,X,t)\tilde{\rho}_m(x,X), \tag{3.16}
$$

where

$$
\tilde{\rho}_m(x,X) = \frac{1}{(2\pi\hbar)^N}\sum_{\lambda\lambda'} g_{\lambda\lambda'}(x)\rho_W^{\lambda'\lambda}(X). \tag{3.17}
$$

Here, $g_{\lambda\lambda'}(x)$ is given by [78]

$$
g_{\lambda\lambda'}(x) = \frac{2^{n+1}}{\hbar}e^{-x^2/\hbar}[r_\lambda r_{\lambda'} - i(r_\lambda p_{\lambda'} - r_{\lambda'}p_\lambda) + p_\lambda p_{\lambda'} - \frac{\hbar}{2}\delta_{\lambda\lambda'}]. \tag{3.18}
$$

3.3.2 Quantum-Classical Dynamics via the FBTS

In this section, we provide a summary of the main theoretical results leading to the FBTS of the QCLE in terms of the coherent state basis. The full details are given in Ref. [40].

The matrix elements of $\hat{A}_W(X,t)$ in the subsystem basis may be expressed in terms of the coherent state basis as

$$\begin{aligned}
A_W^{\lambda\lambda'}(X,t) &= \sum_{\mu\mu'}\int\prod_{i=1}^{M}\frac{d^2z_i}{\pi^n}\frac{d^2z_i'}{\pi^n}\langle m_\lambda|z_1\rangle\langle z_1'|m_{\lambda'}\rangle \\
&\quad\times\Big(\langle z_1(t_1)|z_2\rangle e^{i\Delta t_2\mathcal{L}_e(X_{t_1},z_2,z_2')/2}\left(\langle z_2|\ldots\right. \\
&\quad\left.\times A_W^{\mu\mu'}(X_{t_1})\ldots|z_2'\rangle\right)\langle z_2'|z_1'(t_1)\rangle\Big)\,, \qquad (3.19)
\end{aligned}$$

where $|m_\lambda\rangle$ is the eigenstate of n fictitious harmonic oscillators (with occupation numbers 0 or 1 such that $|m_\lambda\rangle = |0_1,\ldots,1_\lambda,\ldots,0_n\rangle$), $|z_i\rangle$ is the n-dimensional coherent state [81] at time step i with eigenvalue $z = (q+ip)/\sqrt{2\hbar}$, and $\Delta t_i = t_i - t_{i-1} = \tau$ for all i with $t_0 = 0$ and $t_M = t$. Here, $q = (q_1,\ldots,q_n)$ and $p = (p_1,\ldots,p_n)$ are the average positions and momenta of the harmonic oscillators in the state $|z\rangle$, respectively; e.g., $q = \langle z|\hat{q}|z\rangle$. The effective evolution operator $i\mathcal{L}_e(X,z,z')$ is given by

$$i\mathcal{L}_e(X,z,z') = \frac{P}{M}\cdot\frac{\partial}{\partial R} - \frac{\partial V_e(X,z,z')}{\partial R}\cdot\frac{\partial}{\partial P}, \qquad (3.20)$$

where $V_e(X,z,z') = [V_{cl}(R,z)+V_{cl}(R,z')]/2$ and $V_{cl}(R,z) = V_e(R) - \mathrm{Tr}_s\hat{h}(R) + V_c^{\lambda\lambda'}(R)z_\lambda^* z_{\lambda'}$. Consequently, $e^{i\mathcal{L}_e(X,z,z')\tau}\hat{A}_W(X) = \hat{A}_W(X_\tau)$.

If the phase space coordinates of two coherent states are substantially different, then one can assume that $\langle z_1(t_1)|z_2\rangle \approx \pi^n\delta(z_2 - z_1(t_1))$ and $\langle z_2'|z_1'(t_1)\rangle \approx \pi^n\delta(z_2' - z_1'(t_1))$, for example. Then, performing the integrals over the coherent state variables z_i and z_i' for $\{i,i'\} \geq 2$ and applying the effective evolution operator to the coherent state and bath phase space variables leads to

$$\begin{aligned}
A_W^{\lambda\lambda'}(X,t) &= \sum_{\mu\mu'}\int\frac{d^2z_1}{\pi^n}\frac{d^2z_1'}{\pi^n}\langle m_\lambda|z_1\rangle\langle z_1'|m_{\lambda'}\rangle \\
&\quad\times\Big(\langle z_1(t_1)|m_\mu\rangle A_W^{\mu\mu'}(X_t)\langle m_{\mu'}|z_1'(t)\rangle\Big)\,. \qquad (3.21)
\end{aligned}$$

Evaluating the overlaps using $\langle m_\lambda | z \rangle = z_\lambda e^{-|z|^2/2}$, expressing the above equation in terms of $x = (q,p)$ variables, and using the fact that $\sum_\nu (q_\nu^2 + p_\nu^2)$ is conserved under coherent state dynamics, gives

$$\begin{aligned} A_W^{\lambda\lambda'}(X,t) &= \sum_{\mu\mu'} \int dx dx' \phi(x)\phi(x') \\ &\quad \times \frac{1}{2\hbar}(q_\lambda + ip_\lambda)(q'_{\lambda'} - ip'_{\lambda'}) A_W^{\mu\mu'}(X_t) \\ &\quad \times \frac{1}{2\hbar}(q_\mu(t) - ip_\mu(t))(q'_{\mu'}(t) + ip'_{\mu'}(t)), \end{aligned} \tag{3.22}$$

where $\phi(x) = (2\pi\hbar)^{-n} e^{-\sum_\nu (q_\nu^2 + p_\nu^2)/2\hbar}$. The coupled evolution of the bath and coherent state variables are dictated by the following equations of motion:

$$\begin{aligned} &\frac{dq_\mu}{dt} = \frac{\partial H_{cl}(R,P,q,p)}{\partial p_\mu}, \quad \frac{dp_\mu}{dt} = -\frac{\partial H_{cl}(R,P,q,p)}{\partial q_\mu}, \\ &\frac{dq_{\mu'}}{dt} = \frac{\partial H_{cl}(R,P,q',p')}{\partial p_{\mu'}}, \quad \frac{dp_{\mu'}}{dt} = -\frac{\partial H_{cl}(R,P,q',p')}{\partial q_{\mu'}}, \\ &\frac{dR}{dt} = \frac{P}{M}, \quad \frac{dP}{dt} = -\frac{\partial H_e(R,P,q,p,q',p')}{\partial R}, \end{aligned} \tag{3.23}$$

where

$$H_e(R,P,q,p,q',p') = \frac{1}{2}[H_{cl}(R,P,q,p) + H_{cl}(R,P,q',p')], \tag{3.24}$$

with

$$H_{cl}(X,x) = H_e(X) - \mathrm{Tr}_s \hat{h}(R) + \frac{1}{2\hbar} \sum_{\lambda\lambda'} h^{\lambda\lambda'} (q_{\lambda'} q_\lambda + p_\lambda p_{\lambda'}). \tag{3.25}$$

Solving these equations yields a simple dynamics in which the forward and backward trajectories of the coherent state variables are propagated forward in time, while the bath coordinates evolve on the mean potential that depends on these two sets of trajectories.

Finally, the expectation value of an observable $\hat{A}(t)$ is given by

$$\overline{A(t)} = \sum_{\lambda\lambda'} \int dX A_W^{\lambda\lambda'}(X,t)\rho_W^{\lambda'\lambda}(X), \tag{3.26}$$

where $A_W^{\lambda\lambda'}(X,t)$ is given by Eq. (3.22).

3.3.3 Nonlinear Optical Response via the Equation-of-Motion Phase-Matching Approach

In order to calculate the components of the N^{th} order polarization corresponding to a specific phase-matching condition, we adopt the EOM-PMA [123, 124] coupled with the PBME solution and FBTS. In this approach, one directly calculates these components in the spirit of the perturbative approach, avoiding the decomposition of the total polarization as in the nonperturbative approach. As a result, EOM-PMA is computationally more efficient than the nonperturbative approach, yet maintains the attractive features of this approach (i.e., allows for arbitrary pulse shapes/durations and pulse overlap). However, as in the perturbative approach, EOM-PMA is restricted to weak fields.

According to the PBME [using Eq. (3.16)] and FBTS [using Eqs. (3.22) and (3.26)] approaches, the total polarization (i.e., expectation value of the dipole moment operator) may be calculated via

$$P(t) = \int dxdX \mu_m(x,X,t)\tilde{\rho}_m(x,X) \equiv \langle \mu(t) \rangle_{PBME}, \tag{3.27}$$

and

$$\begin{aligned} P(t) &= \sum_{\mu\mu'\lambda\lambda'} \int dX dx dx' \phi(x)\phi(x')\rho_W^{\lambda'\lambda}(X) \\ &\times \frac{1}{2\hbar}(q_\lambda + ip_\lambda)(q'_{\lambda'} - ip'_{\lambda'})\mu_W^{\mu\mu'}(X_t) \\ &\times \frac{1}{2\hbar}(q_\mu(t) - ip_\mu(t))(q'_{\mu'}(t) + ip'_{\mu'}(t)) \\ &\equiv \langle \mu(t) \rangle_{FBTS}, \end{aligned} \tag{3.28}$$

respectively. The total polarization contains contributions from all possible wave vectors

$$\mathbf{k} = \sum_{\alpha=1}^{N_p} l_\alpha \mathbf{k}_\alpha, \tag{3.29}$$

where l_α can be any integer. However, in nonlinear spectroscopic experiments, different signals are often distinguished by the direction of the wave vector of the emitted radiation. Thus, one needs to extract the component of $P(t)$ corresponding to a signal with a particular $\mathbf{k}$:

$$P_{\mathbf{k}}(t) = \mathcal{P}_{\mathbf{k}}(t) \exp\{i\mathbf{kr}\} + \text{c.c.} \tag{3.30}$$

According to EOM-PMA, the component $\mathcal{P}_{\mathbf{k}}(t)$ proportional to $\exp\{\pm i\mathbf{kr}\}$ may be calculated via

$$\mathcal{P}_k(t) \approx \langle \mu^\Sigma(t) \rangle_{PBME/FBTS}, \tag{3.31}$$

where

$$\mu^\Sigma(t) = \sum_{n=0}^{N_p} (-1)^{n+1} \mu_n(t), \tag{3.32}$$

with

$$\mu_n(t) = \sum_{|\mathbf{g}|^2=n} \mu^{g_{\alpha_1}, g_{\alpha_2}, \ldots, g_{\alpha_{N_P}}}(\mathbf{g}, t) \qquad n = 0, 1, 2, \ldots, N_p \tag{3.33}$$

Here, $\mathbf{g} = (g_1, g_2, \ldots, g_{N_P})$ where g_α can equal either 0 (field switched off) or 1 (field switched on). The time evolution of $\mu^{g_{\alpha_1}, g_{\alpha_2}, \ldots, g_{\alpha_{N_P}}}(\mathbf{g}, t)$ may be simulated by solving Eqs. (3.15) and Eqs. (3.23) in the cases of PBME and FBTS, respectively, under the influence of a *complex* field given by

$$\mathbf{E}\left(\mathbf{g}, t\right) = \sum_{\alpha=1}^{N_P} g_\alpha \mathbf{A}_\alpha f_\alpha \left(t - t_\alpha\right) \exp\left\{-i\omega_\alpha \left(t - t_\alpha\right)\right\}. \tag{3.34}$$

3.3.4 Simulation of Pump-Probe Signal

The approach explained above can be applied to simulate any type of N_p-pulse experiment. Here, we focus on the simulation of TA pump-probe signals. To this end, we consider the interaction of a material system with three laser pulses (i.e., $N_P = 3$): two identical super-imposed pulses centered at time t_1 (constituting the pump pulse) and a third pulse centered at time t_3 (constituting the probe pulse). The pump-probe signal radiates in the $\mathbf{k}_{PP} = -\mathbf{k}_1 + \mathbf{k}_2 + \mathbf{k}_3 = \mathbf{k}_3$ (since $\mathbf{k}_1 = \mathbf{k}_2$) direction and, therefore, we wish to extract the component of $P(t)$ that is proportional to $\exp\left\{\pm i\mathbf{k_3 r}\right\}$ (i.e., $\mathcal{P}_{k_3}(t)$). In order to perform this extraction, we rewrite the *real* electric field (see Eq. (3.3)) as follows:

$$\mathbf{E}\left(t\right) = \sum_{\alpha=1}^{3} \left(\upsilon_\alpha^+\left(t\right) \exp\left\{+i\mathbf{k}_\alpha \mathbf{r}\right\} + \upsilon_\alpha^-\left(t\right) \exp\left\{-i\mathbf{k}_\alpha \mathbf{r}\right\}\right), \tag{3.35}$$

where

$$\upsilon_\alpha^\pm\left(t\right) = \mathbf{A}_\alpha f\left(t - t_\alpha\right) \exp\{\mp i\omega_\alpha \left(t - t_\alpha\right)\}. \tag{3.36}$$

Since the first two pulses propagate in the $-\mathbf{k_1}$ and $+\mathbf{k_1}$ directions, respectively, and the third pulse propagates in the $\mathbf{k}_3$ direction, we see that (by comparing with Eq. (3.35)) the complex field in Eq. (3.34) which performs the required extraction may be written as

$$\mathbf{E}\left(\mathbf{g},t\right) = g_1 \upsilon_1^- + g_2 \upsilon_2^+ + g_3 \upsilon_3^+. \tag{3.37}$$

Next, we write the expression for $\mu^{\Sigma}(t)$ explicitly as

$$\mu^{\Sigma}(t) = -\mu_0(t) + \mu_1(t) - \mu_2(t) + \mu_3(t), \tag{3.38}$$

where, using Eq. (3.33), the $\mu_n(t)$'s may be written more explicitly as

$$\begin{aligned}
\mu_0(t) &= \mu^{0,0,0}(\mathbf{0},t) \\
\mu_1(t) &= \mu^{1,0,0}(\mathbf{1},t) + \mu^{0,1,0}(\mathbf{1},t) + \mu^{0,0,1}(\mathbf{1},t) \\
\mu_2(t) &= \mu^{1,1,0}(\mathbf{2},t) + \mu^{1,0,1}(\mathbf{2},t) + \mu^{0,1,1}(\mathbf{2},t) \\
\mu_3(t) &= \mu^{1,1,1}(\mathbf{3},t).
\end{aligned} \tag{3.39}$$

In writing these equations, we have considered all combinations of g_α's (i.e., combinations of pulses on and off) that satisfy $|\mathbf{g}|^2 = n$. Thus, in total, there are 2^{N_P} $\mu_m^{g_{\alpha_1}, g_{\alpha_2}, g_{\alpha_3}}$'s that must be propagated. However, if the system has no permanent dipole moment, then $\mu^{0,0,0} = 0$ and the number of propagations reduces to $2^{N_P} - 1$. It should be noted that one can further reduce the number of propagations by invoking the rotating wave approximation for the field-matter interaction [124].

In the end, we calculate the time-integrated TA pump-probe signal, which is given by [114]

$$I\left(t_3 - t_1\right) = \int_{-\infty}^{+\infty} dt \dot{E}_3\left(t; t_3\right) \mathcal{P}'_{\mathbf{k}_3}\left(t; t_3 - t_1\right), \tag{3.40}$$

where $\mathcal{P}'_{\mathbf{k}_3}$ is the difference between the polarizations with and without excitation by the pump pulse, i.e., $\mathcal{P}_{\mathbf{k}_3}^{\text{pump on}} - \mathcal{P}_{\mathbf{k}_3}^{\text{pump off}}$. If the rotating-wave and slowly-varying amplitude approximations are applied, then the signal becomes [114]

$$I\left(t_3 - t_1\right) = \operatorname{Im} \int_{-\infty}^{+\infty} dt E_3\left(t; t_3\right) \left(\mathcal{P}_{\mathbf{k}_3}^{\prime}\right)^{*} \left(t; t_3 - t_1\right). \tag{3.41}$$

Because this method is limited to weak fields, we have chosen a field strength such that the population does not exceed a few percent.

3.4 Application to a Model PIET Reaction

3.4.1 Model Details

We apply the techniques described above for simulating the time-dependent TA pump-probe signal in a model developed in Ref. [118] for a PIET reaction in the condensed phase. In Ref. [118], the pump-probe signal is computed using a nonperturbative approach for describing nonlinear optical response and the self-consistent hybrid (SCH) method [183] for simulating the quantum dynamics of the system, which is in principle numerically exact. The model subsystem is composed of three electronic states: a ground state $|g\rangle$, a photoinduced excited state $|d\rangle$ corresponding to the donor of the ET reaction, and an optically dark charge transfer state $|a\rangle$ corresponding to the acceptor of the ET reaction. The model bath (which mimics the effect of a polar solvent on the ET reaction) is composed of a collection of independent harmonic oscillators that are linearly coupled to the acceptor state of the subsystem. Within our mixed quantum-classical approach, the subsystem is treated quantum mechanically, whereas the oscillator bath is treated classically.

The Hamiltonian of this system is given by

$$\begin{aligned}\hat{H}(t) &= |g\rangle\epsilon_g\langle g| + |d\rangle\epsilon_d\langle d| + |a\rangle\epsilon_a\langle a| + \Delta\left(|d\rangle\langle a| + |a\rangle\langle d|\right) \\ &+\frac{1}{2}\sum_{j=1}^{N}\left[P_j^2 + \omega_j^2\left(R_j + |a\rangle\frac{2c_j}{\omega_j^2}\langle a|\right)^2\right] - \hat{\mu}\cdot\mathbf{E}\left(t\right), \end{aligned}\tag{3.42}$$

where ϵ_g, ϵ_d, and ϵ_a are the energies of the ground, excited donor, and excited acceptor electronic states, respectively, Δ is the donor-acceptor electronic coupling, R_j and P_j are the mass-weighted coordinate and momentum, respectively, of the j^{th} bath mode with frequency ω_j and coupling constant c_j, and $N_p = 3$ in $\mathbf{E}\left(t\right)$. The dipole moment operator of the subsystem couples states $|g\rangle$ and $|d\rangle$ and is given by

$$\hat{\mu} = |g\rangle\mu_{gd}\langle d| + |d\rangle\mu_{dg}\langle g|, \tag{3.43}$$

where $\mu_{gd} = \mu_{dg}$ is the electronic transition dipole moment. In the subsystem basis $\{|g\rangle, |d\rangle, |a\rangle\}$, $\hat{H}(t)$ has the following matrix form:

$$\begin{aligned}\hat{H}(t) &= \begin{pmatrix} \epsilon_g & -\mu_{gd}\mathbf{E}\left(t\right) & 0 \\ -\mu_{dg}\mathbf{E}\left(t\right) & \epsilon_d & \Delta \\ 0 & \Delta & \epsilon_a + 2\sum_j R_j c_j + 2\sum_j \frac{c_j^2}{\omega_j^2} \end{pmatrix} + H_e\mathbb{I}, \\ &\equiv \hat{h}(R) + H_e\mathbb{I}, \end{aligned}\tag{3.44}$$

where $H_e = \frac{1}{2}\sum_j(P_j^2 + \omega_j^2 R_j^2)$ and $\mathbb{I}$ is the identity matrix.

The coupling between the subsystem and oscillator bath is characterized by a spectral density $J\left(\omega\right) = \frac{\pi}{2}\sum_j \frac{c_j^2}{\omega_j}\delta\left(\omega - \omega_j\right)$, which is chosen to be Debye in form [184]:

$$J\left(\omega\right) = \frac{\lambda_D}{2}\sum_j \frac{\omega\omega_D}{\omega^2 + \omega_D^2}, \tag{3.45}$$

where λ_D is the bath reorganization energy and ω_D is the characteristic frequency. Using the bath discretization procedure described in Ref. [183], one can show that $c_j = \sqrt{\lambda_D \tan^{-1}(\omega_{max}/\omega_D)/(\pi N)}\omega_j$ and $\omega_j = \tan(j \tan^{-1}(\omega_{max}/\omega_D)/N)\omega_D$, where ω_{max} is the maximum frequency of the spectral density and N is the number of oscillators [185].

The initial density matrix is assumed to be uncorrelated, with the subsystem in its ground state and the bath in thermal equilibrium:

$$\rho_W\left(0\right) = \rho_s\left(0\right)\rho_e\left(X\right), \tag{3.46}$$

where the subsystem density matrix, $\rho_s(0)$, is

$$\rho_s(0) = \begin{pmatrix} 1 & 0 & 0 \\ 0 & 0 & 0 \\ 0 & 0 & 0 \end{pmatrix}, \tag{3.47}$$

and the Wigner distribution of the bath, $\rho_e\left(X\right)$, is [186]

$$\rho_e\left(X\right) = \prod_{j=1}^{N} \frac{\beta\omega_j}{2\pi u_j^{''}} \exp\left[-\frac{\beta}{u_j^{''}}\left\{\frac{P_j^2}{2} + \frac{1}{2}\omega_j^2 R_j^2\right\}\right], \tag{3.48}$$

with $u_j^{''} = u_j \coth u_j$ and $u_j = \frac{\beta\hbar\omega_j}{2}$.

3.4.2 PBME Equations

From Eq. (3.13), the mapping form of the Hamiltonian is given by

$$\begin{aligned} H_m(t) &= \frac{1}{2}\sum_{j=1}^{N}\left(P_j^2+\omega_j^2R_j^2\right)+\frac{\epsilon_g}{2\hbar}\left(r_g^2+p_g^2-\hbar\right)+\frac{\epsilon_d}{2\hbar}\left(r_d^2+p_d^2-\hbar\right) \\ &\quad +\frac{1}{2\hbar}\left(\epsilon_a+\sum_j 2R_jc_j+\sum_j\frac{2c_j^2}{\omega_j^2}\right)\left(r_a^2+p_a^2-\hbar\right)+\frac{\Delta}{\hbar}\left(r_dr_a+p_dp_a\right) \\ &\quad -\frac{1}{\hbar}\left[\left(\mu_{gd}+\mu_{dg}\right)\mathbf{E}\left(t\right)\left(r_gr_d+p_gp_d\right)\right]. \end{aligned} \tag{3.49}$$

With the aid of Eqs. (3.16)−(3.18) and Eq. (3.31), we can compute the polarization component $\mathcal{P}_{\mathbf{k}}(t)$ via

$$\mathcal{P}_k(t)=\int dxdX\mu_m^{\Sigma}(x,t)\tilde{\rho}_{sm}\left(x\right)\rho_e\left(X\right), \tag{3.50}$$

where, according to Eq. (3.17),

$$\tilde{\rho}_{sm}\left(x\right)=\frac{2}{\hbar^4\pi^3}\left(r_g^2+p_g^2-\frac{\hbar}{2}\right)e^{-x^2/\hbar}, \tag{3.51}$$

with $x^2=x\cdot x=\sum_\lambda\left(r_\lambda^2+p_\lambda^2\right)$. The expectation value in Eq. (3.50) is determined by sampling the initial bath and mapping variables from their appropriate Gaussian distributions, reweighting by $\frac{2}{\hbar^4\pi^3}\left(r_g^2+p_g^2-\frac{\hbar}{2}\right)$, and, in order to compute $\mu_m^{\Sigma}(x,t)$, simulating the time evolution of the mapping variables in

$$\mu_m^{g_{a_1},g_{a_2},g_{a_3}}\left(x,\mathbf{g},t\right)=\frac{\mu_{gd}}{\hbar}\left[r_g(\mathbf{g},t)r_d(\mathbf{g},t)+p_g(\mathbf{g},t)p_d(\mathbf{g},t)\right], \tag{3.52}$$

according to Eqs. (3.15) with the Hamiltonian in Eq. (3.49).

3.4.3 FBTS Equations

Using Eqs. (3.22), (3.26), and (3.31), the polarization component can be computed via

$$\begin{aligned}
\mathcal{P}_k(t) &= \int dX \ \mu^{\Sigma}(x,x',t)\rho_e(X) \\
&= \frac{1}{4\hbar^2}\int dX dx dx' \ \phi(x)\phi(x')(q_g+ip_g)(q'_g-ip'_g)\rho_e(X) \\
&\quad \times \sum_{\mu\mu'} \mu^{\Sigma}_{\mu\mu'}(q_\mu(t)-ip_\mu(t))(q'_{\mu'}(t)+ip'_{\mu'}(t)) \\
&\equiv \frac{1}{4\hbar^2}\int dX dx dx' \ \tilde{\rho}_s(x,x')\rho_e(X)\mu^{\Sigma}(x,x',t),
\end{aligned} \tag{3.53}$$

where

$$\tilde{\rho}_s(x,x') = \phi(x)\phi(x')(q_g+ip_g)(q'_g-ip'_g), \tag{3.54}$$

and

$$\mu^{\Sigma}(x,x',t) = \sum_{\mu\mu'} \mu^{\Sigma}_{\mu\mu'}(q_\mu(t)-ip_\mu(t))(q'_{\mu'}(t)+ip'_{\mu'}(t)). \tag{3.55}$$

The computation of $\mu^{\Sigma}(x,x',t)$ is accomplished by simulating the time evolution of the coherent state variables in the individual $\mu^{g_{\alpha_1},g_{\alpha_2},g_{\alpha_3}}(x,x',\mathbf{g},t)$'s according to

$$\begin{aligned}
\mu^{g_{\alpha_1},g_{\alpha_2},g_{\alpha_3}}(x,x',\mathbf{g},t) &= \mu_{gd}\{(q_g(\mathbf{g},t)-ip_g(\mathbf{g},t))(q'_d(\mathbf{g},t)+ip'_d(\mathbf{g},t)) \\
&\quad +(q_d(\mathbf{g},t)-ip_d(\mathbf{g},t))(q'_g(\mathbf{g},t)+ip'_g(\mathbf{g},t))\}.
\end{aligned} \tag{3.56}$$

The expectation value in Eq. (3.53) is finally obtained by sampling the initial bath and coherent state variables from their appropriate Gaussian distributions, $\phi(x)$ and $\phi(x')$, reweighting by $\frac{1}{4\hbar^2}(q_g+ip_g)(q'_g-ip'_g)$, and simulating the time evolutions of the coherent state variables $\{q(t)$, $p(t)$, $q'(t)$, and $p'(t)\}$ according to Eqs. (3.23) with the Hamiltonian in Eq. (3.25) and the definitions of $H_e(X)$ and $\hat{h}$ given by Eq. (3.44).

3.4.4 Results and Discussion

We now present the results of the TA pump-probe signal, which probes the population dynamics of the donor state in the model described above. The model parameters, taken from Ref. [118], are as follows. The electronic energies of the ground, excited donor, and excited acceptor states are $\epsilon_g = 0$ cm^{-1}, $\epsilon_d = 13000$ cm^{-1}, and $\epsilon_a = 13000$ cm^{-1}, respectively, and the donor-acceptor coupling is $\Delta = 50$ cm^{-1}. The characteristic frequency and reorganization energy of the bath, dictated by the Debye spectral density in Eq. (3.45), are $\omega_D = 50$ cm^{-1} and $\lambda_D = 500$ cm^{-1}, respectively. The number of harmonic oscillators needed to represent the condensed phase environment is $N = 20$ and the temperature is $T = 300$ K. All laser pulses have a carrier frequency of $\omega_1 = \omega_2 = \omega_3 = 13000$ cm^{-1} (in resonance with the electronic transition) and a duration of $\tau_1 = \tau_2 = \tau_3 = 50$ fs. The first two laser pulses, which constitute the pump, have a strength of $\mu_{gd}|\mathbf{A}_\alpha|\sqrt{4\ln 2/(\pi\tau_\alpha^2)} = 50$ cm^{-1}, while the probe pulse is taken to be significantly weaker (such that the results are independent of the strength of the probe). In all of our simulations, we have used dimensionless variables and parameters with time scaled by ω_D. The dimensionless time step used for integrating the equations of motion (using the algorithm in Ref. [83]) is $\Delta t = 5 \times 10^{-5}$. Converged results were obtained with 2×10^5 trajectories. As in Ref. [118], the magnitude of the TA signal was rescaled to coincide with that of the population of the photo-excited donor state (results not shown), and is therefore measured in arbitrary units.

Figure 3.1 shows our results for the time-integrated TA pump-probe signal, calculated using Eq. (3.41), in the case of no ET (i.e., $\Delta = 0$ cm^{-1}) as a function of the delay time between the pump and probe pulses. In this case, the ET complex is not coupled to the bath. As can be seen, the profiles calculated via the PBME and FBTS methods are in excellent agreement with the exact result, with the TA signal increasing to a plateau following excitation by the pump pulse. This agreement is expected because the PBME

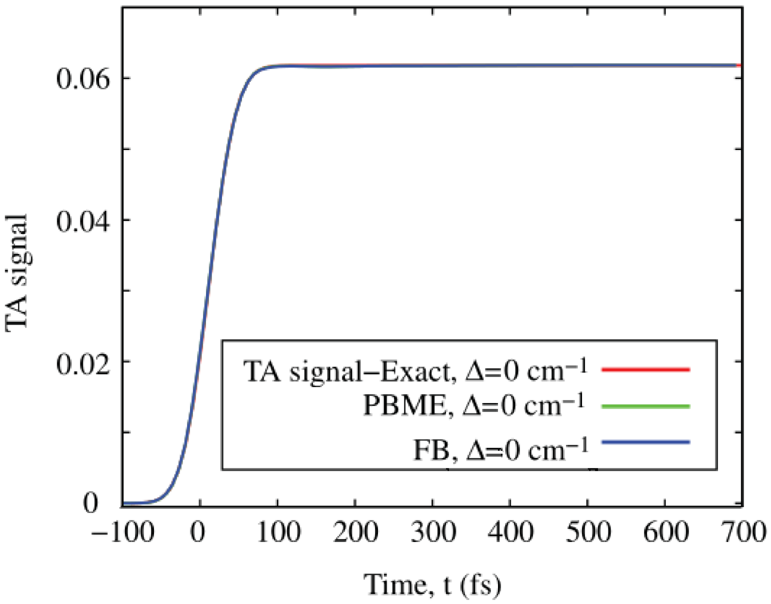

Figure 3.1: Comparison between the TA signal from Ref. [118] and the PBME and FBTS calculations of the TA signal in the absence of electron transfer (where $\Delta = 0$ cm^{-1}). The signal is measured in arb. units.

solution and FBTS become exact when the subsystem is not coupled to the bath.

In the $\Delta = 50$ cm^{-1} case, ET occurs and, in turn, the subsystem and bath couple through the acceptor state. From Fig. 3.2, we see that PBME and FBTS reasonably capture the monotonic decay of the TA signal after the initial rapid increase due to the pump pulse. The signals decay by ~ 0.3 arb. unit and ~ 0.4 arb. unit in the case of PBME and FBTS, respectively (cf. ~ 0.9 arb. unit in the case of the exact result), which suggests that, in this case, replacing the overlap integral by a delta function (see text above Eq. (3.21)) to arrive at the FBTS is not as harsh of an approximation as dropping the extra coupling term in the mapping QCLE to arrive at the PBME. It should be noted that the agreement obtained here for the TA signals is substantially better than that obtained for the time-dependent population of the donor-state (calculated in Ref. [83]), where PBME yielded an unphysical

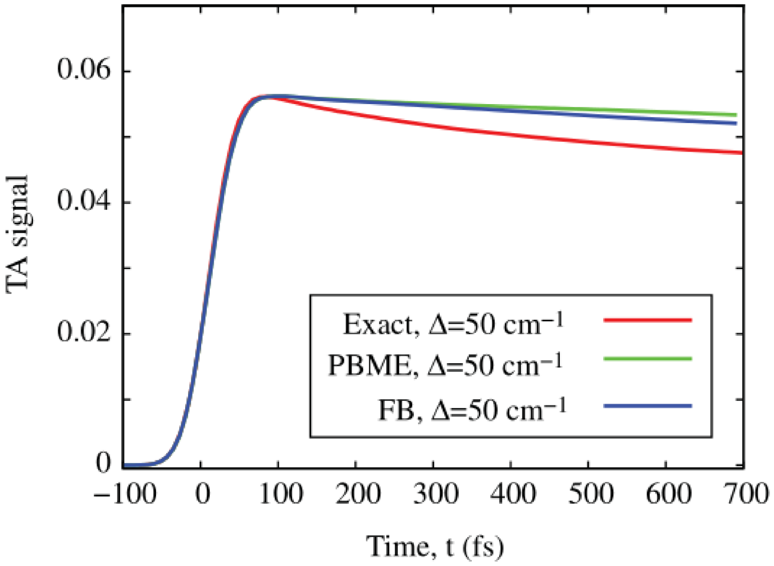

Figure 3.2: Comparison between the TA signal from Ref. [118] and the PBME and FBTS calculations of the TA signal in the presence of electron transfer (where $\Delta = 50$ cm^{-1}). The signal is measured in arb. units.

increase of $\sim 1\%$, while FBTS yielded a decrease of $\sim 0.4\%$ (cf. $\sim 2\%$ decrease for the exact result). This difference in agreements is not surprising as it has been previously observed that the agreement can depend on the form of the observable. For example, accurate PBME results for differences in state populations have been obtained for the symmetric spin-boson model [70], whereas for the model studied herein, PBME yields an unphysical result for the donor-state population due to the $-\hbar$ term in Eq. (3.12) (which vanishes in the case of population differences) [83]. In this study, due to the off-diagonal nature of the subsystem dipole moment observable, the $-\hbar$ term does not even contribute (see Eq. (3.12)).

A potential reason for the discrepancy between the PBME/FBTS and exact results is the relatively strong subsystem-bath coupling (i.e., $\lambda_D\beta = 2.4 > 1$). In Ref. [83], it was observed that as $\lambda_D\beta$ is decreased from 2.4 to 0.24, the agreement between the donor-state population decays predicted by PBME/FBTS and the more accurate QCLE-based surface-hopping improves. This behaviour can be traced back to the fact that the underlying approximations in PBME/FBTS improve as the strength of the subsystem-bath coupling decreases.

3.5 Concluding Remarks

In this Chapter, we presented an approach for calculating nonlinear spectroscopic signals that is based on combining EOM-PMA with the PBME and FBTS methods, two approximate solutions of the QCLE, which give rise to a simple phase-space-like evolution for both the quantum photoactive and classical photoinactive DOF subject to N_p laser pulses. Within the EOM-PMA, one avoids the computationally intensive calculation of multi-time ORFs and directly calculates the desired component of the N^{th} order polarization in a specific phase-matching direction, which can make it more efficient than both perturbative and nonperturbative methods. In practice, the simulations involve generating ensembles of $2^{N_P} - 1$ short trajectories of the chromophore's dipole moment (with the initial conditions of the quantum and classical variables sampled from their corresponding equilibrium distributions) for each set of values of the pulse delays. Although EOM-PMA is restricted to weak fields, it allows for arbitrary pulse shapes/durations and accounts for pulse overlap effects.

The use of the PBME and FBTS methods within the EOM-PMA was demonstrated by calculating TA pump-probe signals for a model condensed phase PIET reaction. By comparing with the numerically exact results for the TA signals, we were able to evaluate the performance of these mixed quantum-classical approaches. Taking into consideration the fact that the subsystem-bath coupling is relatively strong, we find that our results are in reasonable agreement with the exact results, with FBTS performing slightly better than PBME. In general, both methods would work best in low subsystem-bath coupling situations (i.e., $\lambda_D \beta \leq 1$), since their underlying approximations improve as the strength of the subsystem-bath coupling decreases. Given the simplicity of their algorithms and their improved convergence properties (relative to QCLE-based surface-hopping), PBME and FBTS can provide effective alternatives to surface-hopping methods in EOM-PMA simulations of multidimensional vibrational/electronic spectra of realistic mixed quantum-classical chemical and biological systems.

Chapter 4

Mixed Quantum-Classical Simulations of Transient Absorption Pump-Probe Signals for a Photo-Induced Electron Transfer Reaction Coupled to an Inner-Sphere Vibrational Mode

4.1 Abstract

In the previous chapter, we demonstrated the ability of two approximate solutions of the quantum-classical Liouville equation (QCLE) for qualitatively capturing the electronic dynamics in the pump-probe transient absorption (TA) signal of a model of a condensed phase photo-induced electron transfer reaction whose ground and excited donor states have the same equilibrium geometry. However, the question remains as to the ability of these solutions for treating the more complex situation in which the electronic states are coupled

to a low-frequency inner-sphere harmonic vibrational mode (representing an intramolecular mode of the donor-acceptor complex) that shifts their equilibrium geometries with respect to each other and thereby gives rise to signatures of vibrational dynamics in the TA signal. Thus, in this chapter, we investigate this situation by treating the vibrational mode both quantum mechanically and classically within the context of the approximate Poisson Bracket Mapping Equation (PBME) and Forward-Backward Trajectory solutions (FBTS) of the QCLE. Depending on the definition of the quantum subsystem, both PBME and FBTS are capable of qualitatively capturing several of the main features in the exact TA signal and quantitatively capturing the characteristic timescale of the vibrational dynamics, despite the moderately strong subsystem-bath coupling in this model. Particularly, we find that treating the vibrational mode quantum mechanically using either PBME or FBTS better captures the signatures of the vibrational dynamics, while treating it classically using FBTS better captures the decay in the signal. These findings underscore the utility of the PBME and FBTS approaches for efficiently modelling and interpreting TA signals.

4.2 Introduction

The study of photo-induced electron transfer (PIET) is of great importance to the understanding of energy transfer in photosynthetic systems [87–90] and to the development of solar energy harvesting materials such as those used in photovoltaic cells [91–95]. Detailed experimental information about the electron transfer dynamics and participating vibrational modes may be obtained using ultrafast nonlinear spectroscopies. However, given the complexity of the systems in which PIET often occurs, the spectroscopic signals may be difficult to interpret, making it difficult to extract detailed information about the electronic and vibrational dynamics. Theoretical modelling of time- and frequency-resolved spectroscopic signals plays an instrumental role in their interpretation, in particular when the PIET occurs in complex, condensed phase environments. In practice, however, fully quantum mechanical simulations of nonlinear spectroscopic signals are not computationally tractable in the case of systems with many degrees of freedom (DOF). Thus, it is desirable to develop and apply approximate methods that are capable of capturing the essential physics with reasonable accuracy and within a reasonable amount of computational time.

The fact that PIET reactions first involve a light-induced excitation of a chromophore from its ground electronic state to an excited donor state, followed by the transfer of an electron from a donor group to an acceptor group, suggests that the system may be partitioned into three sets of DOF: the electronic DOF of the donor and acceptor, key vibrational DOF in the donor and acceptor which influence the electron transfer, and the typically many DOF in the environment. The mass scale separations between these sets of DOF can be exploited to avoid a fully quantum mechanical treatment of the system and to adopt a mixed quantum-classical one. In a mixed quantum-classical treatment, one would treat the electronic DOF of the donor and acceptor quantum mechanically, the vibrational DOF involved in the electron transfer either quantum mechanically or classically, and the environmental DOF classically. Such a treatment could dramatically reduce the cost of computing observables, while retaining a sufficiently accurate picture of the coupled electronic and nuclear dynamics. Over the years, many mixed quantum-classical methods have been proposed for simulating nonadiabatic dynamics, which essentially differ in the way they couple the quantum and classical DOF [30–45].

The Fewest Switches Surface-Hopping (FSSH) method [46] is one of the most popular mixed quantum-classical methods for simulating nonadiabatic dynamics. However, in spite of its popularity, FSSH suffers from an inability to treat decoherence. Several schemes have been developed to resolve this problem, but because FSSH lacks a rigorous derivation, they are ad hoc in nature [56–58, 187]. One of the most rigorous ways of simulating the nonadiabatic dynamics of mixed quantum-classical systems is based on the solution of the quantum-classical Liouville equation (QCLE) [31, 33, 164–166, 169]. The QCLE approach has been shown to perform better than FSSH, due to its rigorous treatment of decoherence effects. However, observables calculated via the surface-hopping solution of the QCLE [67–69] are challenging to converge for systems of appreciable size and complexity due to highly oscillatory weights that result from the Monte Carlo sampling of nonadiabatic transitions, i.e., a huge ensemble of trajectories is typically required for convergence. This drawback motivated the development of two approximate solutions of the QCLE, namely the Poisson Bracket Mapping Equation (PBME) solution[38, 71, 78] and the Forward-Backward Trajectory Solution (FBTS),[40, 72, 86] which greatly reduce the number of trajectories required for the convergence of observables. In these approaches, the quantum DOF are expressed in terms of continuous variables, while in the surface-hopping implementation they are represented in terms of discrete states. The approximations which lead to these two solutions are most valid when the coupling between the quantum and the classical DOF is relatively weak. These solutions have been tested on both simple and complex model systems, yielding a wide range of agreements with more accurate results [38, 71, 72, 78, 83, 179, 188, 189].

In our previous study [188], we combined the efficiency of the PBME and FBTS methods and the efficiency of the equation-of-motion phase-matching approach (EOM-PMA) [124, 190] for calculating the pump-probe transient absorption (TA) signal of a model condensed phase PIET reaction whose ground and excited donor states have the same equilibrium geometry. EOM-PMA is an attractive approach because it combines attractive features from both perturbative [99, 101, 102, 107, 111] and nonperturbative [113, 114, 116, 121, 122, 191] methods for calculating nonlinear spectra to efficiently simulate the time-dependent polarization of a system in any phase-matching direction in response to weak laser fields of arbitrary shape. The results of our study demonstrated that while the PBME and FBTS methods were not capable of qualitatively capturing the behaviour of the time-dependent population of the excited donor state, these methods performed comparatively well at capturing the TA signal [188]. This fortuitous agreement was attributed to the off-diagonal nature of the dipole moment operator, which leads to a cancellation of errors in the calculation of the polarization.

The goal of this chapter is to gauge the abilities of PBME-PMA and FBTS-PMA for effectively simulating the TA signal of the same condensed phase PIET model as in Ref. [188], but now with the donor and acceptor electronic states coupled to an inner-sphere harmonic vibrational mode representing a key vibration in the electron transfer complex. This has the effect of shifting the equilibrium geometries of the ground and excited donor states with respect to each other, which gives rise to nonequilibrium vibrational dynamics upon photo-excitation that can be detected in the TA signal. The TA signals are calculated using different pulse parameters (viz., width and carrier frequency), while treating the additional vibrational mode either quantum mechanically or classically. In addition, we calculate the time-dependent population of the excited donor state and compare to the results obtained when the ground and excited donor states have the same equilibrium geometry. The PBME-PMA and FBTS-PMA results are compared to those obtained via the numerically exact self-consistent hybrid (SCH) method [28, 192] in order to assess their abilities for extracting quantitative and qualitative insights into the electron transfer dynamics and the dynamics of the inner-sphere vibrational mode.

4.3 PIET Model

In this chapter, we study a vibronic model for a condensed phase PIET, originally proposed in Ref. [118], with the following Hamiltonian

$$\begin{aligned}\hat{H}(t) = & |g\rangle\epsilon_g\langle g| + |d\rangle\epsilon_d\langle d| + |a\rangle\epsilon_a\langle a| + \Delta(|d\rangle\langle a| + |a\rangle\langle d|) \\ & + \frac{1}{2}\left\{P_v^2 + \Omega^2\left[|g\rangle Q_v^2\langle g| + |d\rangle\left(Q_v - \frac{2\kappa}{\Omega^2}\right)^2\langle d| + |a\rangle\left(Q_v - \frac{\kappa}{\Omega^2}\right)^2\langle a|\right]\right\}, \\ & + \frac{1}{2}\sum_{j=1}^{N}\left[P_j^2 + \omega_j^2\left(Q_j + |a\rangle\frac{2c_j}{\omega_j^2}\langle a|\right)^2\right] - \hat{\mu}\cdot\mathbf{E}(t)\end{aligned} \tag{4.1}$$

This Hamiltonian corresponds to a system with three electronic states: a ground state $|g\rangle$ with energy ϵ_g, a photo-excited donor state $|d\rangle$ with energy ϵ_d, and an optically dark acceptor state $|a\rangle$ with energy ϵ_a. The parameter Δ refers to the electronic coupling between the donor and acceptor states. Each electronic state is coupled to an inner-sphere vibrational mode, with position Q_v, momentum P_v, frequency Ω, and coupling constant κ. The electron transfer complex is linearly coupled to a bath of N independent harmonic oscillators (intended to mimic the effect of a solvent) with frequencies $\{\omega_j\}$, coupling constants $\{c_j\}$, and mass-weighted positions and momenta $\{Q_j\}$ and $\{P_j\}$, respectively. The last term in the Hamiltonian denotes the field-matter interaction energy, with $\hat{\mu}$ given by [118]

$$\hat{\mu} = |g\rangle\mu_{gd}\langle d| + |d\rangle\mu_{dg}\langle g|, \tag{4.2}$$

where $\mu_{gd} = \mu_{dg}$ is the electronic transition dipole moment and the incident electric field $E(t)$, which is composed of a sum of N_p coherent laser pulses, is given by

$$\mathbf{E}(t) = \sum_{\alpha=1}^{N_p}\mathbf{A}_\alpha f_\alpha(t - t_\alpha)\exp\{i\,[\mathbf{k}_\alpha\mathbf{r} - \omega_\alpha(t - t_\alpha)]\} + \text{c.c.} \tag{4.3}$$

In the above equation, each laser pulse α is characterized by its wave vector $\mathbf{k}_\alpha$, carrier frequency ω_α, pulse envelope f_α, and the product of the polarization vector and amplitude of the pulse, $\mathbf{A}_\alpha$. The envelope function is taken to be a Gaussian centered at time t_α:

$$f_\alpha(t - t_\alpha) = \sqrt{\frac{4\ln 2}{\pi\tau_\alpha^2}} \exp\left(-4\ln 2\frac{(t - t_\alpha)^2}{\tau_\alpha^2}\right) \tag{4.4}$$

where τ_α is the full-width at half-maximum of the pulse. In this chapter, we will assume that the electric field remains parallel to the dipole moment vector over the duration of the pulse (to simplify the notation, we drop the vector notation for the dipole moment).

The model parameters correspond to those used for calculating the exact quantum results in Ref. [118]. The electronic state energies are $\epsilon_g = 0$ and $\epsilon_d = \epsilon_a = 12000$ cm^{-1}. Two values of the donor-acceptor coupling are investigated, i.e., $\Delta = 0$ cm^{-1} (for no electron transfer) and $\Delta = 50$ cm^{-1}. The parameters corresponding to the inner-sphere vibrational mode are $\Omega = 300$ cm^{-1} and $2\kappa^2/\Omega^2 = 1000$ cm^{-1}. The harmonic oscillator bath is characterized by its spectral density $J(\omega) = \frac{\pi}{2}\sum_j \frac{c_j^2}{\omega_j}\delta(\omega - \omega_j)$ and is chosen to be of Debye form [184]

$$J(\omega) = \frac{\lambda_D}{2}\sum_j \frac{\omega\omega_D}{\omega^2 + \omega_D^2} \tag{4.5}$$

where $\lambda_D = 500$ cm^{-1} is the bath reorganization energy and $\omega_D = 50$ cm^{-1} is the characteristic frequency. The coupling constants and frequencies are given by $c_j = \sqrt{\lambda_D \tan^{-1}(\omega_{max}/\omega_D)/(\pi N)}\omega_j$ and $\omega_j = \tan(j\tan^{-1}(\omega_{max}/\omega_D)/N)\omega_D$, respectively, where ω_{max} is the maximum frequency of the spectral density [28, 185, 192].

4.4 Observables via the PBME and FBTS Methods

In this section, we summarize the main results needed to compute observables via the PBME and FBTS methods. Before starting, we note that the Hamiltonian of a quantum subsystem coupled to a classical environment has the following general form:

$$\hat{H} = H_e + \hat{h}_s + \hat{V}_c \equiv H_e + \hat{h} \tag{4.6}$$

where H_e is the environmental Hamiltonian, $\hat{h}_s$ is the subsystem Hamiltonian, $\hat{V}_c$ is the subsystem-environment coupling, and $\hat{h} = \hat{h}_s + \hat{V}_c$.

Within the PBME approach, the expectation value of an operator $\hat{A}$ may be calculated via [38]

$$\overline{A(t)} = \int dx dX A_m(x, X, t) \tilde{\rho}_m(x, X) \tag{4.7}$$

where the analogue of $\hat{A}$ in the mapping basis [79] is given by

$$A_m(x, X) = \frac{1}{2\hbar} \sum_{\lambda\lambda'} A_W^{\lambda\lambda'}(X)(r_\lambda r_{\lambda'} + p_\lambda p_{\lambda'} - \hbar\delta_{\lambda\lambda'}) \tag{4.8}$$

and the analogue of the initial density matrix in the mapping basis is given by

$$\begin{aligned}\tilde{\rho}_m(x, X) =& \frac{1}{(2\pi\hbar)^n} \sum_{\lambda\lambda'} \frac{2^{n+1}}{\hbar} e^{-\sum_\lambda (r_\lambda^2 + p_\lambda^2)/\hbar} \rho_W^{\lambda'\lambda}(X) \\ & \times \left(r_\lambda r_{\lambda'} - i(r_\lambda p_{\lambda'} - r_{\lambda'} p_\lambda) + p_\lambda p_{\lambda'} - \frac{\hbar}{2}\delta_{\lambda\lambda'} \right)\end{aligned} \tag{4.9}$$

In the above equations, $x = (r, p) = (r_1, \ldots, r_n, p_1, \ldots, p_n)$ denotes the set of mapping variables of the n-dimensional quantum subsystem, $X = (R, P)$ denotes the set of positions and momenta of the N-dimensional classical environment, the subscript W denotes a partial Wigner transform [170] over the environmental DOF, and $A^{\lambda\lambda'} = \langle\lambda|\hat{A}|\lambda'\rangle$, where $|\lambda\rangle$ is a quantum subsystem state defined by $\hat{h}_s|\lambda\rangle = \epsilon_\lambda|\lambda\rangle$. The time evolution of $A_m(x, X, t)$ is obtained by first sampling the initial values of the subsystem mapping and bath variables using $\tilde{\rho}_m(x, X)$ and evolving them in time by solving the following coupled equations of motion

$$\begin{aligned}
\frac{dr_\lambda(t)}{dt} &= \frac{\partial H_m}{\partial p_\lambda} = \frac{1}{\hbar}\sum_{\lambda'} \overline{h}_{\lambda\lambda'}\,(R(t), t)\, p_{\lambda'}(t), \\
\frac{dp_\lambda(t)}{dt} &= -\frac{\partial H_m}{\partial r_\lambda} = -\frac{1}{\hbar}\sum_{\lambda'} \overline{h}_{\lambda\lambda'}\,(R(t), t)\, r_{\lambda'}(t), \\
\frac{dR(t)}{dt} &= \frac{\partial H_m}{\partial P(t)} = \frac{P(t)}{M},\ \frac{dP(t)}{dt} = -\frac{\partial H_m}{\partial R(t)}
\end{aligned} \tag{4.10}$$

where the mapping analogue of the Hamiltonian is given by [71]

$$H_m(x, X) = H_e(X) + \frac{\mathrm{Tr}\,\hat{h}}{n} + \frac{1}{2\hbar}\sum_{\lambda\lambda'} \overline{h}^{\lambda\lambda'}(r_\lambda r_{\lambda'} + p_\lambda p_{\lambda'}), \tag{4.11}$$

and the traceless form of the matrix elements of $\hat{h}$ are given by

$$\overline{h}^{\lambda\lambda'} = h^{\lambda\lambda'} - \delta_{\lambda\lambda'}(\mathrm{Tr}\,\hat{h}/n) \tag{4.12}$$

It should be noted that using the traceless version of the Hamiltonian has been shown to enhance the reliability of the simulations by minimizing the incidence of unstable trajectories that take the system out of the physical space [71, 193, 194].

Within the FBTS approach, the expectation value of an operator $\hat{A}$ may be calculated via [40]

$$\overline{A(t)} = \sum_{\lambda\lambda'} \int dX A_W^{\lambda\lambda'}(X, t)\rho_W^{\lambda'\lambda}(X), \tag{4.13}$$

where

$$\begin{aligned} A_W^{\lambda\lambda'}(X,t) &= \sum_{\mu\mu'} \int dx dx' \phi(x)\phi(x') \\ &\quad \times \frac{1}{2\hbar}(q_\lambda + ip_\lambda)(q'_{\lambda'} - ip'_{\lambda'}) A_W^{\mu\mu'}(X_t) \\ &\quad \times \frac{1}{2\hbar}(q_\mu(t) - ip_\mu(t))(q'_{\mu'}(t) + ip'_{\mu'}(t)) \end{aligned} \tag{4.14}$$

In the above equations, $x = (q,p) = (q_1,\ldots,q_n,p_1,\ldots,p_n)$ and $x' = (q',p') = (q'_1,\ldots,q'_n,p'_1,\ldots,p'_n)$ denote the two sets of coherent state variables [81] of the n-dimensional quantum subsystem, and $\phi(x) = (2\pi\hbar)^{-n} e^{-\sum_\nu (q_\nu^2+p_\nu^2)/2\hbar}$. The time evolution of $A_W^{\lambda\lambda'}(X,t)$ is obtained by first sampling the initial values of the coherent state and bath variables using $\phi(x)$, $\phi(x')$, and $\rho_W^{\lambda'\lambda}(X)$, and evolving them forward in time by solving the following coupled equations of motion

$$\begin{aligned} &\frac{dq_\mu}{dt} = \frac{\partial H_{cl}(x,X)}{\partial p_\mu}, \quad \frac{dp_\mu}{dt} = -\frac{\partial H_{cl}(x,X)}{\partial q_\mu}, \\ &\frac{dq_{\mu'}}{dt} = \frac{\partial H_{cl}(x',X)}{\partial p_{\mu'}}, \quad \frac{dp_{\mu'}}{dt} = -\frac{\partial H_{cl}(x',X)}{\partial q_{\mu'}}, \\ &\frac{dR}{dt} = \frac{P}{M}, \quad \frac{dP}{dt} = -\frac{\partial H_{e2}(x,x',X)}{\partial R} \end{aligned} \tag{4.15}$$

where the coherent state variables are propagated using

$$H_{cl}(x,X) = H_e(X) + \frac{1}{2\hbar}\sum_{\lambda\lambda'} \overline{h}^{\lambda\lambda'}(q_{\lambda'}q_\lambda + p_\lambda p_{\lambda'}), \tag{4.16}$$

and the bath variables are propagated using the mean potential

$$H_{e2}(x,x',X) = \frac{1}{2}\left[H_{cl}(x,X) + H_{cl}(x',X)\right]. \tag{4.17}$$

4.5 Computational Details

4.5.1 Calculating the Hamiltonian Matrix Elements

The calculation of the Hamiltonian matrix elements appearing in the PBME and FBTS approaches will depend on how the quantum subsystem is defined. For the vibronic model considered herein, it is possible to define the quantum subsystem Hamiltonian in two ways, depending on whether or not we include the inner-sphere vibrational mode as part of the quantum subsystem. When the inner-sphere vibrational mode is treated classically, the quantum subsystem Hamiltonian only involves the first line of Eq. 4.1, and the calculations are the same as in our previous studies [83, 188]. On the other hand, when it is treated quantum mechanically, one must also add the terms involving P_v and Q_v to the subsystem Hamiltonian. This introduces some new technical details in the implementation of the PBME and FBTS, which we discuss in this section. From this point on, we will specify whether the additional vibrational mode is treated quantum mechanically or classically along with the method, e.g., classical-Q_v PBME will refer to a classical treatment of the vibrational mode within the context of PBME dynamics, and so on.

When treating the inner-sphere vibrational mode quantum mechanically, we may express the subsystem Hamiltonian as

$$\hat{h}_s = \hat{h}^g + \hat{h}^d + \hat{h}^a \tag{4.18}$$

where

$$\hat{h}^\alpha = |\alpha\rangle \left[\epsilon_\alpha + \frac{1}{2}\{\hat{P}_v^2 + \Omega^2 \left(\hat{Q}_v - q_\alpha\right)^2\} \right] \langle\alpha| \tag{4.19}$$

Here, q_α refers to the shift in the equilibrium geometry of electronic state $|\alpha\rangle$ along the vibrational coordinate, i.e., $q_g = 0$, $q_d = 2\kappa/\Omega^2$ and $q_a = \kappa/\Omega^2$ (see Eq. 4.1). Owing to the form of $\hat{h}_s$, one may represent it as a block diagonal matrix (i.e., $h_s = h_v^g \oplus h_v^d \oplus h_v^a$, where

h_v^α is a Hamiltonian in the vibrational subspace corresponding to electronic manifold α and $\oplus$ denotes the matrix direct sum) and decompose the diagonalization of h_s into three independent eigenvalue problems (i.e., $\hat{h}_v^\alpha|i^\alpha\rangle = \varepsilon_i^\alpha|i^\alpha\rangle$, where $|i^\alpha\rangle$ is the i^{th} vibrational eigenstate within electronic manifold α). Thus, a subsystem eigenstate can be expressed as $|\alpha, i^\alpha\rangle = |\alpha\rangle|i^\alpha\rangle \equiv |\lambda\rangle$. Because the vibrational mode is a harmonic oscillator, we can easily write that

$$\langle\alpha|\langle i^\alpha|\hat{h}_s|j^\beta\rangle|\beta\rangle = \left[\epsilon_\alpha + \Omega\left(i + \frac{1}{2}\right)\right]\delta_{\alpha i,\beta j} \tag{4.20}$$

Consequently, there is no need to numerically diagonalize the subsystem Hamiltonian at each step of the dynamics and all of the Hamiltonian matrix elements, $h^{\lambda\lambda'}$, for this model may be computed analytically.

As we have seen, quantizing the inner-sphere vibrational mode generates a set of vibronic subsystem states for each electronic manifold. The factor that determines the number of vibronic states used for the ground electronic manifold in the simulations is the temperature. Higher vibronic levels may have negligible or no populations at certain temperatures and, therefore, will not contribute to the dynamics. Based on the model parameters used in this study, we found that 20 vibronic states for the ground electronic manifold was sufficient for convergence of the results. In the case of the donor and acceptor electronic states, more vibronic levels were used to account for the possibility of the pump pulse leading to the population of higher vibronic levels on the donor electronic state. The precise number of levels depends on the pulse and vibrational mode coupling parameters, and for this study we found that 25 vibronic states for each of the donor and acceptor manifolds was sufficient.

4.5.2 Initializing the System

We now discuss how the initial values for the quantum and classical variables were sampled for the vibronic model considered herein. As is commonly done, we assume that the initial system density matrix is uncorrelated, with the subsystem in its ground electronic state and the environment in thermal equilibrium. Thus, its expression can be given by

$$\hat{\rho}_W(0) \approx \hat{\rho}_s(0) \otimes \rho_e(X). \tag{4.21}$$

In the case that the inner-sphere vibrational mode is treated classically, the subsystem density matrix is given by

$$\hat{\rho}_s(0) \rightarrow \begin{pmatrix} 1 & 0 & 0 \\ 0 & 0 & 0 \\ 0 & 0 & 0 \end{pmatrix}, \tag{4.22}$$

and the Wigner distribution of the harmonic oscillator bath is given by [186]

$$\rho_e(X) = \prod_{j=1}^{N} \frac{\beta\omega_j}{2\pi u_j''} \exp\left[-\frac{\beta}{u_j''}\left(\frac{P_j^2}{2} + \frac{1}{2}\omega_j^2 R_j^2\right)\right], \tag{4.23}$$

with $u_j^{''} = u_j \coth u_j$, $u_j = \frac{\beta\hbar\omega_j}{2}$, and $\beta = 1/kT$. It should be noted that the initial position and momentum (Q_v, P_v) of the harmonic inner-sphere vibrational mode are also sampled using Eq. 4.23, with its corresponding parameters. In the case that the inner-sphere vibrational mode is treated quantum mechanically, the subsystem density matrix is obtained by assuming a Boltzmann distribution for the vibrational state populations in the ground electronic state. More specifically,

$$\hat{\rho}_s(0) \rightarrow \frac{1}{Z}\begin{pmatrix} \rho_{\mathbf{g}} & & \mathbf{0} \\ & \mathbf{0} & \\ \mathbf{0} & & \mathbf{0} \end{pmatrix}, \tag{4.24}$$

where the partition function Z is given by

$$Z = \sum_{\lambda} \langle \lambda | e^{-\beta \hat{h}} | \lambda \rangle \tag{4.25}$$

and $\rho_{\mathbf{g}}$ is a 20×20 diagonal matrix, whose diagonal matrix elements are given by

$$\rho_g^i = \exp\left[-\frac{\epsilon_g + \Omega\,(i + 1/2)}{kT} \right]. \tag{4.26}$$

This equation can be used to verify that for the twentieth vibronic level $\rho_g^{20} \approx 0$. As in the previous case, the positions and momenta of the harmonic oscillator bath are sampled using Eq. 4.23. In both cases, the initial values of the mapping and coherent state variables are sampled from $e^{-\sum_{\lambda}\left(r_{\lambda}^2 + p_{\lambda}^2/\hbar\right)}$ and $e^{-\sum_{\nu}(q_{\nu}^2 + p_{\nu}^2)/2\hbar}$, respectively.

4.5.3 Simulating the Pump-probe TA Signal

The approach for calculating the TA signal using PBME and FBTS within the EOM-PMA [124, 190] was formulated in the previous chapter and demonstrated on a purely electronic model of a condensed phase PIET reaction. Here, we only summarize the main results needed to calculate the TA signal for the model studied herein.

In a typical pump–probe experiment, the subsystem under study essentially interacts with three laser pulses: two super-imposed pulses (forming the pump pulse) centered at time t_1 and a third probe pulse centered at time t_3. The resulting polarization of interest, $\mathcal{P}_{\mathbf{k_3}}(t)$, radiates in the $\mathbf{k}_{PP} = -\mathbf{k}_1 + \mathbf{k}_2 + \mathbf{k}_3 = \mathbf{k}_3$ (since $\mathbf{k}_1 = \mathbf{k}_2$) direction. Within PBME/FBTS-PMA, $\mathcal{P}_{\mathbf{k_3}}(t)$ may be calculated via [188]

$$\mathcal{P}_{\mathbf{k_3}}(t) \approx \langle \mu^{\Sigma}(t) \rangle_{PBME/FBTS}, \tag{4.27}$$

where $\langle \cdots \rangle_{PBME/FBTS}$ refers to an average calculated using Eq. 4.7/Eq. 4.13 and

$$\mu^{\Sigma}(t) = -\mu_0(t) + \mu_1(t) - \mu_2(t) + \mu_3(t), \tag{4.28}$$

and

$$\begin{aligned}
\mu_0(t) &= \mu^{0,0,0}(\mathbf{0}, t) \\
\mu_1(t) &= \mu^{1,0,0}(\mathbf{1}, t) + \mu^{0,1,0}(\mathbf{1},t) + \mu^{0,0,1}(\mathbf{1}, t) \\
\mu_2(t) &= \mu^{1,1,0}(\mathbf{2}, t) + \mu^{1,0,1}(\mathbf{2},t) + \mu^{0,1,1}(\mathbf{2}, t) \\
\mu_3(t) &= \mu^{1,1,1}(\mathbf{3}, t)
\end{aligned} \tag{4.29}$$

In the above equation, $\mu^{g_1,g_2,g_3}(\mathbf{g}, t)$ represents the dipole moments resulting from different combinations of the pulses being on and off, i.e., g_α can either be 0 or 1 depending on whether the α^{th} pulse is off or on, respectively, with $\mathbf{g} = g_1 + g_2 + g_3$. When the inner-sphere vibrational mode is treated classically, the classical-Q_v PBME evolution of these dipole moments is given by [188]

$$\mu^{g_1,g_2,g_3}(x, \mathbf{g}, t) = \frac{\mu_{gd}}{\hbar}\left[r_g(\mathbf{g}, t) r_d(\mathbf{g}, t) + p_g(\mathbf{g}, t) p_d(\mathbf{g}, t)\right], \tag{4.30}$$

while the classical-Q_v FBTS evolution is given by [188]

$$\begin{aligned}
\mu^{g_1,g_2,g_3}(x, x', \mathbf{g}, t) &= \mu_{gd}\{(q_g(\mathbf{g}, t) - ip_g(\mathbf{g}, t))(q'_d(\mathbf{g}, t) + ip'_d(\mathbf{g}, t)) \\
&\quad +(q_d(\mathbf{g}, t) - ip_d(\mathbf{g}, t))(q'_g(\mathbf{g}, t) + ip'_g\mathbf{g}, t))\},
\end{aligned} \tag{4.31}$$

where (r_g, p_g) and (r_d, p_d) are the mapping variables corresponding to the ground and donor electronic states, respectively, while (q_g, p_g, q'_g, p'_g) and (q_d, p_d, q'_d, p'_d) are the coherent state variables corresponding to the ground and donor electronic states, respectively. When the inner-sphere vibrational mode is treated quantum mechanically, the quantum-Q_v PBME evolution of these dipole moments is given by

$$\mu^{g_1,g_2,g_3}(x,\mathbf{g},t) = \frac{\mu_{gd}}{\hbar}\sum_{i,j}\langle i^g|j^d\rangle\left[r_{g,i}(\mathbf{g},t)r_{d,j}(\mathbf{g},t)+p_{g,i}(\mathbf{g},t)p_{d,j}(\mathbf{g},t)\right], \tag{4.32}$$

while the quantum-Q_v FBTS evolution is given by

$$\begin{aligned}\mu^{g_1,g_2,g_3}(x,x',\mathbf{g},t) &= \mu_{gd}\sum_{i,j}\langle i^g|j^d\rangle\{(q_{g,i}(\mathbf{g},t)-ip_{g,i}(\mathbf{g},t))(q'_{d,j}(\mathbf{g},t)+ip'_{d,j}(\mathbf{g},t)) \\ &\quad +(q_{d,j}(\mathbf{g},t)-ip_{d,j}(\mathbf{g},t))(q'_{g,i}(\mathbf{g},t)+ip'_{g,i}(\mathbf{g},t))\},\end{aligned} \tag{4.33}$$

where $(r_{\alpha,i},p_{\alpha,i})$ and $(q_{\alpha,i},p_{\alpha,i},q'_{\alpha,i},p'_{\alpha,i})$ are the mapping and coherent state variables, respectively, corresponding to the subsystem state $|\alpha,i^\alpha\rangle$. Therefore, to calculate $\mu^\Sigma(t)$ in Eq. 4.28, one must propagate eight trajectories corresponding to all on–off combinations of the pump and probe pulses (i.e., each term on the RHS of Eqs. 4.29) by evolving the mapping and coherent state variables in time as prescribed by Eqs. 4.10 and 4.15, respectively. Finally, within the rotating wave and slowly-varying amplitude approximations, the time-integrated TA pump–probe signal can be calculated via [114]

$$I\left(t_3-t_1\right) = \mathrm{Im}\int\limits_{-\infty}^{+\infty} E_3\left(t;t_3\right)\left(\mathcal{P}'_{\mathbf{k}_3}\right)^*\left(t;t_3-t_1\right)dt, \tag{4.34}$$

where the asterisk denotes the complex conjugate, E_3 is the probe field, and $\mathcal{P}'_{\mathbf{k}_3} = \mathcal{P}^{\text{pump on}}_{\mathbf{k}_3} - \mathcal{P}^{\text{pump off}}_{\mathbf{k}_3}$ is the difference between the polarizations with and without excitation by the pump pulse.

In the following section, we also present PBME and FBTS results for the time-dependent population of the donor state. These were obtained by calculating the expectation value of

$\hat{P}_d = |d\rangle\langle d|$ using Eqs. 4.7 and 4.13.

4.6 Results and Discussion

Our main goal is to assess how effective the PBME and FBTS methods are for simulating the time-integrated TA signal of the vibronic PIET model presented herein. This is accomplished by comparing our results to the numerically exact results in Ref. 118 obtained using a combination of a nonperturbative approach for simulating the nonlinear signal and the SCH method. Unless mentioned otherwise, the pulse parameters used in this study are $\omega_1 = \omega_2 = \omega_3 = 13000$ cm^{-1} and $\tau_1 = \tau_2 = \tau_3 = 30$ fs. The equations of motion (i.e., Eqs. 4.10 and 4.15) were integrated using a velocity Verlet-type algorithm [83] with time steps of $\Delta t = 0.2$ fs for PBME and $\Delta t = 0.04$ fs for FBTS. We used 20 harmonic oscillators for the bath and the temperature was 300 K (giving rise to a moderately strong subsystem-bath coupling since $\beta\lambda_D = 2.4 > 1$). Converged results were obtained using approximately 10^5 trajectories.

Before presenting the results of the time-integrated TA signals, we first discuss the time-dependent population of the donor state to get a sense of how well the PBME and FBTS methods fare in capturing the population dynamics. Previously, we found that PBME and FBTS struggled to qualitatively capture the population dynamics in a purely electronic version of the model under moderately strong subsystem-bath coupling conditions [83]. In particular, PBME gave rise to a non-physical increase in the donor-state population in time instead of a decrease due to electron transfer to the acceptor state. This was due to the combination of the -$\hbar\delta_{\lambda\lambda'}$ term in Eq. 4.8 (which is non-zero when propagating operators that are diagonal in the subsystem basis) and the emergence of inverted potentials that take the mapping variables out of their physical space [71]. On the other hand, FBTS performed substantially better than PBME, since it yielded a slight decrease in the population.

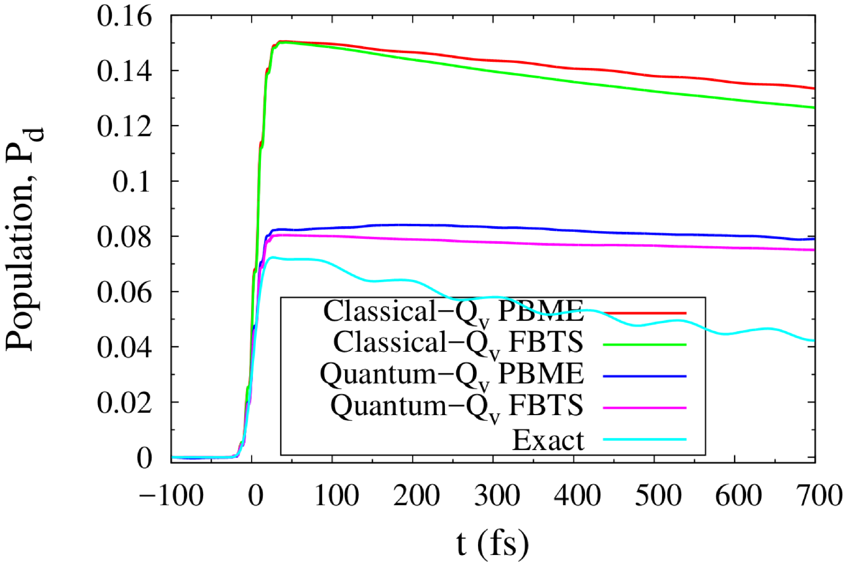

Figure 4.1: Time-dependent populations of the donor state calculated via the PBME and FBTS methods with $\Delta = 50$ cm^{-1}, using quantized and classical treatments of the inner-sphere vibrational mode. For comparison, the exact result obtained via the SCH method is shown [118].

In Fig. 4.1, we show the donor-state populations obtained for the case in which the electronic coupling between the donor and acceptor states is $\Delta = 50$ cm^{-1}. As can be seen, the exact population starts at zero, rapidly increases to a maximum value of $\approx 7\%$ after photo-excitation by the pump pulse, and then exhibits an oscillatory decay to $\approx 4\%$ within 700 fs due to electron transfer to the acceptor state. The ≈ 100 fs period of the oscillation corresponds to the vibrational frequency of $\Omega = 300$ cm^{-1} of the inner-sphere mode to which the electron transfer is coupled.

The PBME/FBTS results in Fig. 4.1 differ from the exact ones in several respects, which depend on whether or not the inner-sphere vibrational mode is described quantum mechanically. First, the maximum population observed in the quantum-Q_v PBME/FBTS results is $\approx 1\%$ higher than that in the exact result, while the classical-Q_v PBME/FBTS methods overshoot the exact maximum by $\approx 8\%$. This inability to reproduce the exact maximum during the pulse is due to the fact that PBME and FBTS employ generalized mean potentials, which are not capable of accurately capturing the abrupt changes in the potential that lead to the electron transfer. The improvement in the agreement with the exact maximum upon quantization of the vibrational mode is due to the fact that, in a classical description, there is no restriction on the energy that can be absorbed by the system from the pulse. In this case, a higher number of accessible vibronic states within the donor electronic state manifold become populated, leading to the much higher maximum donor-state populations observed in the classical-Q_v results. Second, the quantum-Q_v PBME/FBTS results show very small decays in the population compared to the exact decay of $\approx 3\%$, while the classical-Q_v PBME/FBTS results exhibit a decay of $\approx 1.6\%$ and 2.4% for PBME and FBTS, respectively. It should be noted that, between 50 and 150 fs, quantum-Q_v PBME exhibits a slight increase in the population before it decays, while in our previous study [83], PBME gave rise to a relatively large monotonic increase in the population. In the current model, the coupling of the vibrational mode to the electron transfer complex leads to a reduction in the asymmetry of the diagonal elements of the Hamiltonian (induced by the coupling to the harmonic oscillator bath) compared to that of the Hamiltonian in the absence of the vibrational mode. As a result, using the traceless version of the Hamiltonian, $\overline{h}$, leads to better behaved results than using the original Hamiltonian, h, which could lead to sudden inversions of the potential that take the mapping variables outside of their physical space. When the original Hamiltonian, h, is used in this case, one obtains unphysical results with classical-Q_v PMBE, namely a monotonic increase in the donor-state population after the pump pulse, and barely any change with classical-Q_v FBTS [83]. With quantum-Q_v FBTS/PBME, the increase in the dimensionality of the system aggravates the asymmetry of h and thereby increases the incidence of numerical instabilities in trajectories (i.e., breakdown in energy conservation), especially in the case of quantum-Q_v PBME. Finally, of the approximate methods, only the classical-Q_v PBME result exhibits oscillations, although they are highly damped compared to the exact case. This could be understood in terms of how the approximations leading to these two methods are affected by the partitioning of the system into quantum and classical parts. In the case of PBME, a term responsible for higher order couplings between the quantum subsystem and classical environment is dropped from the QCLE in the mapping representation to arrive at the PBME. It has been shown that retaining this term cancels out an extra term in the PBME, which over-compensates for the back reaction of the quantum subsystem on its environment [78]. Therefore, by adding the vibrational mode to the quantum subsystem in quantum-Q_v PBME, one over-compensates for the back reaction of this mode on the classical environment, which may in turn wash out the signatures of the vibrational dynamics. In contrast, by adding the vibrational mode to the classical environment in classical-Q_v PBME, these effects are avoided, albeit at the cost of treating this mode classically. In the case of FBTS, an orthogonality approximation is made in the exact solution of the QCLE to arrive to the FBTS [40], which has been shown to work best under weaker subsystem-bath coupling conditions. As seen, the effect of this approximation is to wash out the oscillations and to minimize the population decay when the vibrational mode is treated quantum mechanically. In summary, no single approximate method qualitatively captures all of the features of the population dynamics. Quantizing the inner-sphere vibrational mode leads to a dramatic improvement in the maximum population, but substantially inhibits the subsequent population decay compared to the classical treatment.

We now move on to the main results of this study, i.e., the time-integrated TA signals calculated via the PBME and FBTS methods. In Figures 4.2 and 4.3, we show the TA signals obtained for two values of the electronic coupling between the donor and acceptor

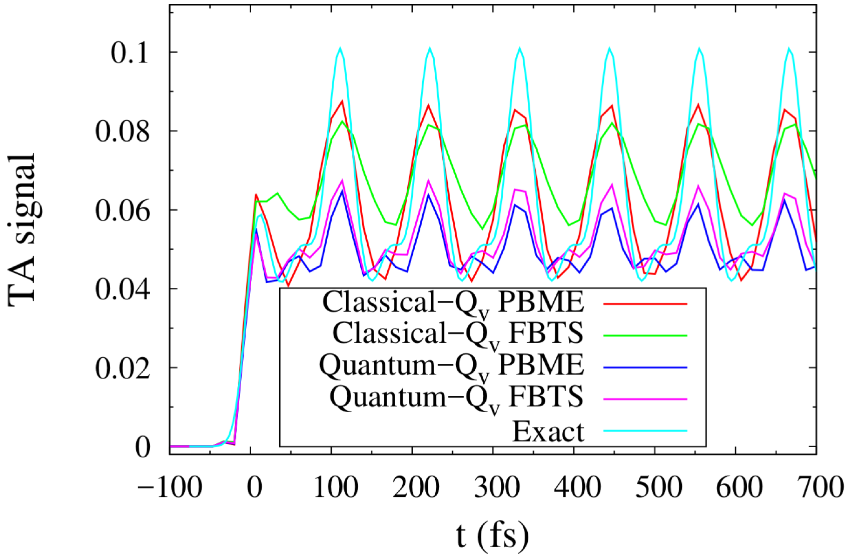

Figure 4.2: Time-integrated TA signal calculated via the PBME and FBTS methods with $\Delta = 0$ cm^{-1}, using quantized and classical treatments of the inner-sphere vibrational mode. For comparison, the exact result obtained via the SCH method is shown [118].

states, viz. $\Delta = 0$ cm^{-1} (where no electron transfer occurs) and $\Delta = 50$ cm^{-1}, respectively. In the $\Delta = 0$ cm^{-1} case, the exact TA signal initially exhibits a rise, followed by a repeated pattern of oscillations with a ≈ 100 fs period. No overall decay of the signal is observed since the donor and acceptor states are not electronically coupled. By comparing with the $\Delta = 0$ cm^{-1} result in the absence of the inner-sphere vibrational mode, which does not exhibit any oscillations, we realize that these oscillations are due to the vibrational dynamics of the inner-sphere mode in the excited donor state [118]. In addition, the shoulders associated with the main oscillations were shown to be due to the vibrational dynamics in the ground state [118]. All of the approximate methods yield decent qualitative and, for some features, quantitative agreement with the exact result, in contrast to the population results. First, the maximum intensity of the TA signal immediately following the photo-excitation by the pump pulse (i.e., after ≈ 15 fs) is well reproduced by all of the approximate methods. Although all four approximate methods underestimate the magnitudes of the remaining oscillations in the TA signal, classical-Q_v PBME captures the majority of the magnitude. More importantly, all methods are able to accurately reproduce the period of the oscillations. Interestingly, quantum-Q_v PBME/FBTS are capable of reproducing the shoulders, while their classical counterparts are not. Overall, this level of agreement between the PBME/FBTS and exact results is promising for future simulations of TA signals in more complex systems. The better agreement between the PBME and exact results (compared to the population results) is likely due to the fact that the time evolution of the dipole moment operator does not involve a -$\hbar$ in Eq. 4.32 (owing to its off-diagonal nature) and, as a result, is less sensitive to trajectories that take the mapping variables out of their physical space. The better agreement between the FBTS and exact results (compared to the population results) is also likely due to the form of the dipole moment operator.

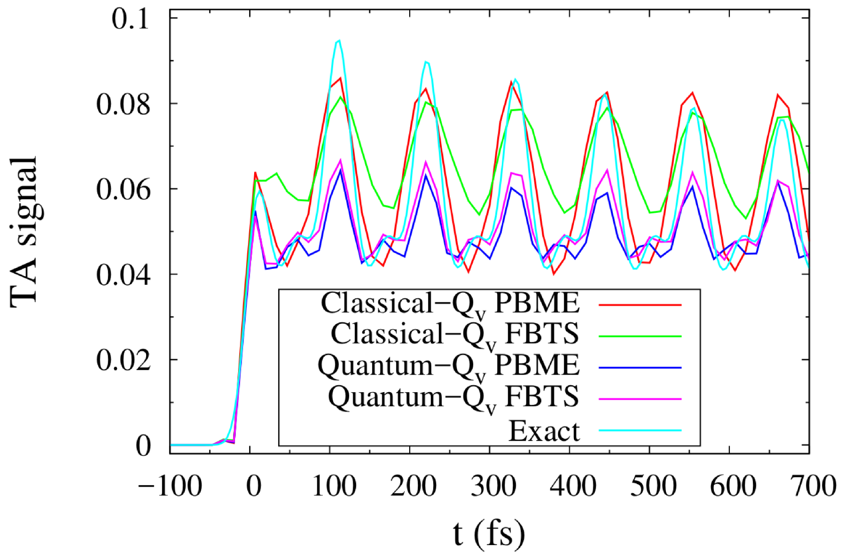

Figure 4.3: Time-integrated TA signal calculated via the PBME and FBTS methods with $\Delta = 50$ cm^{-1}, using quantized and classical treatments of the inner-sphere vibrational mode. For comparison, the exact result obtained via the SCH method is shown [118].

As seen in Fig. 4.3, when $\Delta = 50$ cm^{-1}, the exact TA signal initially rises and then exhibits an oscillatory decay from a peak of maximum intensity 0.095 arb. unit (centered at ≈ 110 fs) to a peak of intensity 0.078 arb. unit (centered at ≈ 660 fs). This decay is due to the electron transfer from the donor to the acceptor state. However, due to the vibrational effects involved in the electron transfer, the TA signal has a slower decay rate than that of the donor-state population since it is composed of both stimulated emission (which reports on the dynamics in the excited donor state) and stimulated Raman (which reports on the dynamics in the ground state) signals [118]. As in the $\Delta = 0$ cm^{-1} case, shoulders associated with the main oscillations are observed. All of the approximate methods yield decent qualitative and, in some cases, quantitative agreement with the exact result. They all give rise to a decay of the signal, albeit not to the same extent as the exact result (viz., from 0.085 arb. unit to 0.082 arb. unit for classical-Q_v PBME, from 0.080 arb. unit to 0.078

arb. unit for classical-Q_v FBTS, from 0.064 arb. unit to 0.061 arb. unit for quantum-Q_v PBME, and from 0.068 arb. unit to 0.061 arb. unit for quantum-Q_v FBTS). Moreover, all of the peaks occur at the same times as those in the exact result.

More information can be obtained from the TA signal using different pulse parameters. For instance, for this model, it is possible to separate the stimulated emission (which reflects the dynamics of the donor-state population) and stimulated Raman contributions to the TA signal if a probe pulse with a sufficiently smaller frequency than the vertical excitation frequency is used [118]. As seen in Fig. 4.4, when $\omega_3 = 11000$ cm^{-1}, the exact TA signal exhibits a more pronounced decay than that in Fig. 4.3, which is in much better agreement with that of the donor-state population and, thus, could be used to extract the electron transfer rate. In addition, there is a change in the frequency and structure of the oscillation compared to those in Fig. 4.3. There are now two frequencies present in the signal, viz., a slower frequency corresponding to that of the vibrational mode and a faster frequency corresponding to the fact that the probe pulse detects the vibrational wave packet twice during each vibration [118]. Also, there is no longer a shoulder associated with each peak. Quantum-Q_v PBME/FBTS are capable of capturing some of the changes in the TA signal (see Fig. 4.4). Both methods capture the two frequencies in the oscillation, but quantum-Q_v PBME yields a more irregular oscillatory pattern, while quantum-Q_v FBTS yields a more regular pattern. On the other hand, classical-Q_v PBME exhibits a different oscillatory pattern, with shoulders appearing next to the main peaks, while classical-Q_v FBTS is only capable of capturing the slower frequency. In both the classical- and quantum-Q_v treatments, FBTS exhibits a slight decay, while PBME does not.

We next investigate how PBME and FBTS perform when the duration of the probe pulse is increased. Increasing the duration leads to lower resolution of the TA signal, as manifested by the disappearance of the peak sub-structure, due to the inability of the probe

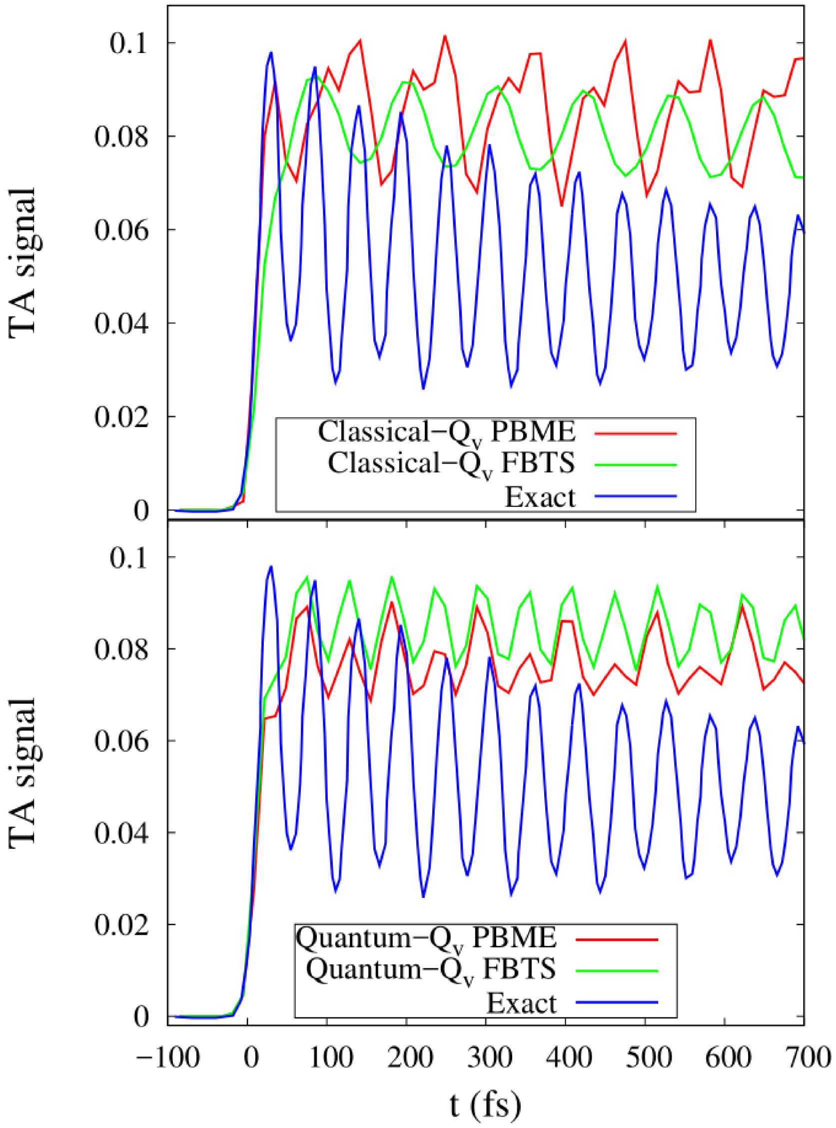

Figure 4.4: Time-integrated TA signal calculated via the classical-Q_v (top panel) and quantum-Q_v (bottom panel) PBME/FBTS methods with $\Delta = 50$ cm^{-1}, but now with a probe pulse frequency of $\omega_3 = 11000$ cm^{-1}. For comparison, the exact result obtained via the SCH method is shown [118].

pulse to detect faster changes in the system. As seen in the exact TA signal in Fig. 4.5, when the duration of the probe pulse is increased to $\tau_3 = 50$ fs, there is only an oscillation with a ≈ 100 fs period corresponding to the period of the vibrational mode. One can no longer resolve the faster oscillation that appeared when the probe pulse had a frequency of $\omega_3 = 11000$ cm^{-1} and a duration of $\tau_3 = 30$ fs (see Fig. 4.4). The PBME and FBTS results for this longer pulse duration are presented in Fig. 4.5. In the quantum-Q_v results, we see that the slower oscillation predominates, although there is still a signature of the faster oscillation. This signature persists for the entire time in the quantum-Q_v FBTS results, while in the PBME results, it disappears after some time. Both quantum-Q_v PBME and FBTS struggle to capture the decay of the TA signal. On the other hand, classical-Q_v PBME exhibits a highly irregular oscillatory pattern, with no decay, while classical-Q_v FBTS exhibits a regular oscillatory pattern with the same frequency as the exact result but with a slightly different phase. It should be noted that of all four methods, classical-Q_v FBTS exhibits a non-negligible decay.

4.7 Concluding Remarks

In this study, we applied two approximate, highly efficient solutions of the QCLE, namely the PBME solution and FBTS, for simulating the time evolution of the donor-state population and the pump-probe TA signal of a vibronic model of a condensed phase PIET reaction. This model represents an electron transfer complex coupled, in which an inner-sphere vibrational mode influences the electron transfer. We considered two different decompositions of the system, one in which this vibrational mode coupled is included in the quantum subsystem and another in which it is included in the classical environment. This led us to test four methods, i.e., classical-Q_v PBME/FBTS and quantum-Q_v PBME/FBTS. Since this was the first application of PBME/FBTS to a PIET reaction involving a harmonic inner-sphere

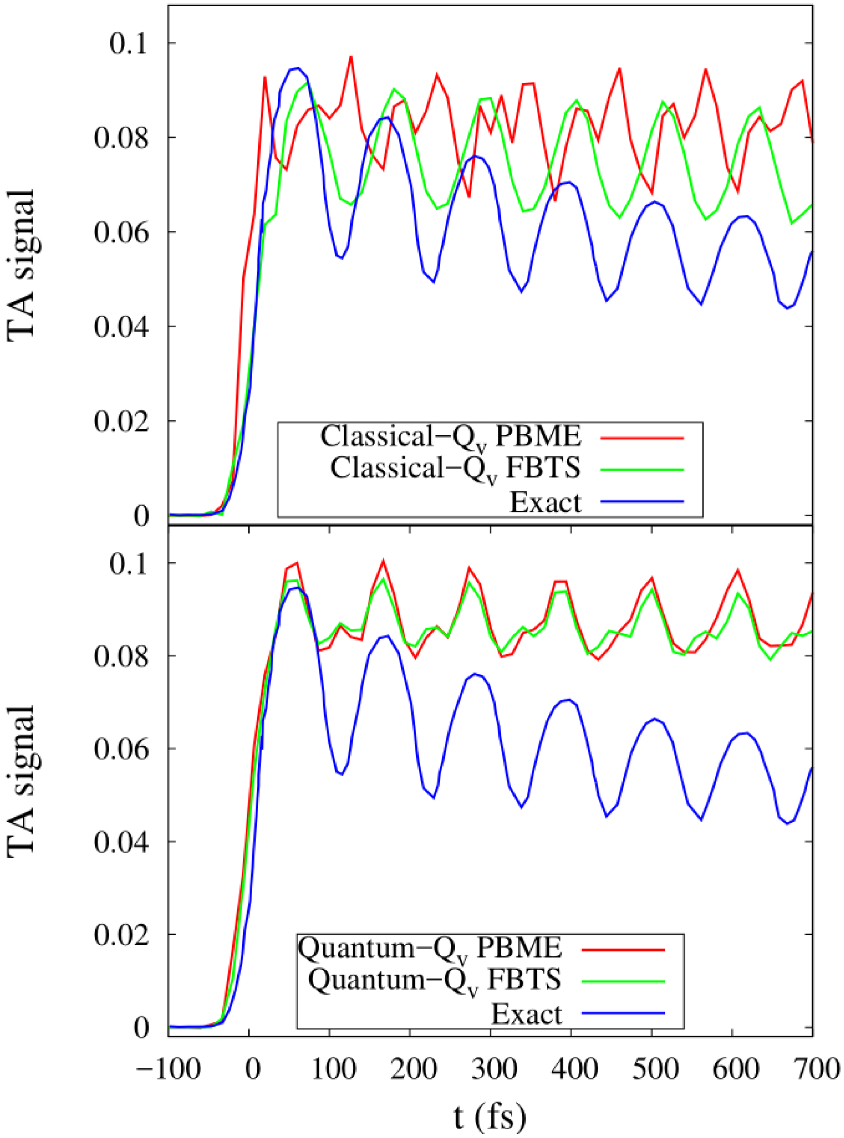

Figure 4.5: Time-integrated TA signal calculated via the classical-Q_v (top panel) and quantum-Q_v (bottom panel) PBME/FBTS methods with $\Delta = 50$ cm^{-1}, but now with a probe pulse frequency of $\omega_3 = 11000$ cm^{-1} and width of $\tau_3 = 50$ fs. For comparison, the exact result obtained via the SCH method is shown [118].

vibrational mode, the details of quantizing this mode were worked out and presented in this study. Due to the approximations inherent to these methods and the moderately strong nature of the subsystem-bath coupling in this model, no single method was able to quantitatively capture all of the features in the exact population and TA signals. Nonetheless, all of the methods were able to qualitatively capture at least some of the features (and some even quantitatively) in these observables. Overall, FBTS and PBME performed similarly, although in some cases FBTS performed slightly better.

Given the moderately strong subsystem-environment conditions, all of the approximate methods considered struggled to satisfactorily represent the decays in the TA signals, which are characteristic of the electron transfer. However, this was not the case for the donor-state population, where classical-Q_v PBME/FBTS yielded substantial decays, but quantum-Q_v PBME/FBTS did not. This was somewhat surprising at first, since one would have expected the quantum-Q_v methods to perform better with respect to all features in the results. In this case, useful information about the electron transfer rate could be extracted from the classical-Q_v calculations of the donor-state population, since a classical treatment of the inner-sphere vibrational mode leads to a more accurate description of the subsystem-environment coupling than the quantum treatment. Apart from a lack of a significant decay in the donor-state population, quantum-Q_v PBME/FTBS performed substantially better than classical-Q_v PBME/FBTS. The classical-Q_v treatments were unable to capture the maximum population following the pump pulse and to reproduce all of the vibrational features in the TA signals, whereas the quantum-Q_v treatments were able to.

In general, the PBME and FBTS methods are not well suited for extracting the electron transfer rate from a pump-probe TA signal of an electron transfer reaction in which the subsystem-environment coupling is moderately strong to strong. However, our study suggests that they can be used to extract reliable information about the vibrational dynamics from the TA signal under these conditions. The next steps will be to determine if the recently proposed improvements to the PBME solution, which are just as efficient as the original PBME solution [84, 85], are capable of capturing the decay in the TA signals of the current model, and to test these methods on more realistic models of PIET reactions which can be parametrized using electronic structure calculations.

Chapter 5

Simulation of a Proton Transfer Reaction in a Polar Nanocluster

We now shift the focus to simulating the dynamics of a heavier particle, the proton. Proton transfer (PT) reactions are common in chemistry and biology, so the assessment of approximate solutions of the QCLE for simulating them is of great interest. In this Chapter, we study PT reactions occurring in polar nanoclusters. In these systems, the PT reaction is mediated by a strong coupling of the proton to the polar solvent. Simulations of such reactions therefore allow one to rigorously test the PBME method, which performs best under weak subsystem-bath coupling conditions. Moreover, this is the first time that the PBME solution is tested on a realistic system. In particular, we investigate a PT reaction in a hydrogen-bonded phenol trimethylamine complex dissolved in a nanocluster of methyl chloride molecules.

5.1 Azzouz-Borgis Model

We investigate a nanocluster model, which is based on the Azzouz–Borgis model [135], for a PT reaction in a hydrogen-bonded phenol (A) trimethylamine (B) complex (denoted by AHB) surrounded by N_S methyl chloride molecules. Within our mixed quantum-classical approach, the proton is the quantum subsystem and the remaining atoms constitute the classical environment. The Hamiltonian of the total system may be written as

$$\begin{aligned} \hat{H}(\hat{r},\hat{p},X) &= K_S(P) + K_C(P) + \hat{K}_P(\hat{p}) \\ &\quad + V_{SS}(R) + \hat{V}_{CS}(\hat{r},R) + \hat{V}_{PS}(\hat{r},R) + \hat{V}_{PC}(\hat{r},R_{AB}), \end{aligned} \tag{5.1}$$

where K_S, K_C, and $\hat{K}_P$ are the kinetic energies of the solvent, complex, and proton, respectively; V_{SS}, $\hat{V}_{CS}$, $\hat{V}_{PS}$, and $\hat{V}_{PC}$ are the solvent–solvent, complex–solvent, proton–solvent, and proton–complex potential energies, respectively; $\hat{r}$ and $\hat{p}$ are the position and momentum operators of the proton, respectively; R and P are the position and momentum vectors of the environment; and R_{AB} is the distance between the A and B groups in the AHB complex.

The A and B groups are modeled as single particles (Fig. 5.1), and polarizability effects are incorporated by allowing the charges on A and B to depend explicitly on the position of the proton, which is restricted to move along the A–B axis. The proton–complex interaction potential is given by a gas-phase H-bonding potential of the following form [135]:

$$\begin{aligned} V_{PC}(r;R_{AB}) &= be^{-aR_{AB}} + D_A\left[1-\exp\left(\frac{-n_A(r-d_A)^2}{2r}\right)\right] \\ &\quad + cD_A\left[1-\exp\left(\frac{-n_B(R_{AB}-r-d_B)^2}{2(R_{AB}-r)}\right)\right], \end{aligned}$$

where r is the distance between A and H. The values of all the parameters are taken

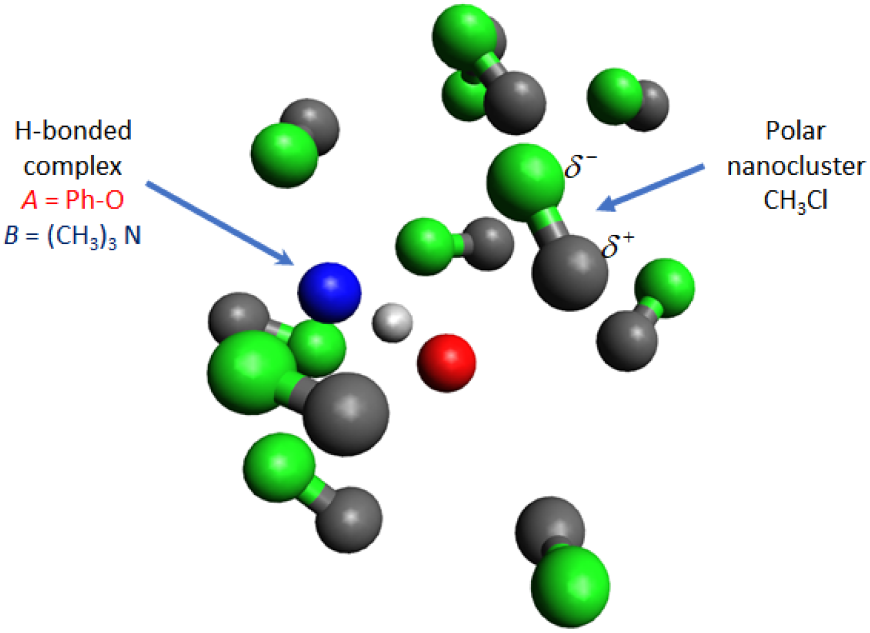

Figure 5.1: A pictorial representation of the Azzouz-Borgis model for a hydrogen-bonded phenol (red sphere) trimethylamine (blue sphere) complex surrounded by a cluster of methylchloride molecules (grey and green spheres).

Parameter	Value	Parameter	Value
a (Å^{-1})	11.2	D_A (kcal mol^{-1})	110
b (kcal mol^{-1})	7.1×10^{13}	n_a (Å^{-1})	9.26
d_A (Å)	0.95	n_b (Å^{-1})	11.42
d_B (Å)	0.97	c	0.776

Table 5.1: Hydrogen bonding potential parameters for the AHB complex, which correspond to a medium strong hydrogen bond.

Site	Q(e)	σ_i (Å)	ϵ_i (kcal mol^{-1})
CH$_3$	+0.25	3.774	0.238
Cl	-0.25	3.481	0.4150

Table 5.2: Lennard-Jones and Coulomb parameters for the methyl chloride solvent interactions.

from Reference [141] and are listed in Table 5.1. It should be noted that different sets of parameter values may be chosen to vary the strength of the hydrogen bond. This particular set of parameter values represents a medium strong OH–N hydrogen bond.

The methyl chloride molecules are modeled as rigid polar diatomic molecules, viz., the methyl and chloride groups are reduced to single sites with a fixed bond distance of 1.781 Å (Fig. 5.1). The solvent–solvent interactions are governed by the following Lennard-Jones and Coulomb potentials:

$$V_{SS} = \sum_{i \in m} \sum_{j \in n \neq m} 4\epsilon_{ij} \left[\left(\frac{\sigma_{ij}}{R_{ij}} \right)^{12} - \left(\frac{\sigma_{ij}}{R_{ij}} \right)^{6} \right] + \frac{K_C Q_i Q_j}{R_{ij}}, \tag{5.2}$$

where R_{ij} is the distance between site i on molecule m and site j on molecule n; ϵ_{ij} and σ_{ij} are the Lennard-Jones parameters between site i on molecule m and site j on molecule n; Q_i and Q_j are the charges sites i and j, respectively; and K_C is the Coulomb constant. The parameter values for this potential are listed in Table 5.2 and correspond to the same values obtained for the force field in Reference [195]. The Berthelot mixing rules are used to derive the cross parameters [196].

Finally, the proton–solvent interactions are governed by a Coulomb potential (V_{PS}), while the complex–solvent interactions are governed by pair-wise Lennard-Jones and Coulombic potentials (V_{CS}). V_{CS} takes the same form as that in Eq. 5.2, with the restriction that m can be only A or B. The Lennard-Jones parameters are chosen to be identical for all the site–site interactions and have the following values: $\sigma = 3.5$ Å and $\epsilon = 0.3974$ kcal mol^{-1}. The electrostatic interactions between any of the sites in the AHB complex and the solvent involve the interaction between the fixed charges of the solvent (Table 5.2) and the r-dependent charges Q_α on the complex. The r-dependency is introduced using the following expression:

$$Q_\alpha = (1 - f(r))Q_\alpha^c + f(r)Q_\alpha^i, \tag{5.3}$$

where

$$f(r) = \frac{1}{2}\left[1 + \frac{r - r_0}{\sqrt{(r - r_0)^2 + l^2}}\right]. \tag{5.4}$$

In the above equation, α is either A, H, or B, $r_0 = 1.43$ Å, and $l = 0.125$ Å. The superscripts c and i refer to the covalent and ionic states, respectively, of the AHB complex. These two states result from the PT reaction, $\mathrm{AH}\cdots\mathrm{B} \rightleftharpoons \mathrm{A}^- \cdots \mathrm{H}^+\ \mathrm{B}$, i.e. when the proton is on the phenol, the complex is in its covalent state, and when the proton is on the amine, the complex is in its ionic state. Thus, by smoothly varying the switching function $f(r)$ (Eq. 5.3) from 0 to 1, one can account for the charge redistribution due to the protonic motion. When $f(r) = 0$, the charges correspond to the ones in the covalent state, and when $f(r) = 1$, the charges correspond to the ones in the ionic state (see values of charges in Table 5.3).

State	Q_A (e)	Q_H (e)	Q_B (e)
Covalent	-0.5	+0.5	0
Ionic	-1.0	+0.5	+0.5

Table 5.3: Charges on the different sites in the AHB complex depending on its charge state.

5.2 PBME Dynamics

5.2.1 Computational Details

In order to simulate the dynamics of the PT reaction using the PBME approach, one first defines the quantum subsystem Hamiltonian as follows:

$$\hat{h}_s = \hat{K}_P(\hat{p}) + \hat{V}_{PC}(\hat{r}, R_{AB}). \tag{5.5}$$

As one can see, this form of the subsystem Hamiltonian depends on R_{AB}, which has implications on the numerical simulation of the system. To evaluate the mapping Hamiltonian (Eq. 2.16), the subsystem states $|\lambda\rangle$ must be obtained by solving the eigenvalue problem $\hat{h}_s|\lambda\rangle = \epsilon_\lambda|\lambda\rangle$. This leads to two scenarios that depend on whether the AB bond length, R_{AB}, is fixed or not. If R_{AB} is fixed, the subsystem Hamiltonian depends only on $\hat{r}$ and $\hat{p}$ and, thus, the subsystem states will not change over the course of a trajectory. In this case, the eigenvalue problem needs to be solved only once at the beginning of the simulation. Conversely, if R_{AB} is not constrained, the AB bond length will fluctuate over the course of a trajectory, rendering the subsystem Hamiltonian R_{AB}-dependent. In this case, the eigenvalue problem must be solved at every time step of the trajectory, adding to the computational cost of the simulation. Another drawback is the introduction of arbitrary eigenvector sign inversions upon diagonalization, which must be properly dealt with. To circumvent these issues, a viable approximation may be to solve the eigenvalue problem only once at the beginning of the simulation for R_{AB} fixed at the average AB distance. Such an approximation would be most valid if the AB distance oscillates, with small deviations about its average value. In this Chapter, the results generated rely on this approximation, in which R_{AB} is fixed at 2.7 Å (in accordance with the average distance reported in Ref. [135]).

The solution of the time-independent Schrödinger equation for $\{|\lambda\rangle\}$ and $\{\epsilon_\lambda\}$ is carried out by expanding the subsystem states in a set of normalized basis functions $|\phi_i\rangle$, i.e.,

$$|\lambda\rangle = \sum_i c_i |\phi_i\rangle, \tag{5.6}$$

which are chosen to be the wavefunctions of the quantum harmonic oscillator,

$$\phi_i(r) = \langle r|\phi_i\rangle = (2^k k!\sqrt{\pi})^{-1/2}\alpha^{1/2} H_k(\alpha(r-r_0))\text{exp}\left[-\alpha^2(r-r_0)^2/2\right], \tag{5.7}$$

where k is an integer, $H_k(x)$ is the k-th Hermite polynomial, and i is an index associated with a pair of values for k and r_0. Two sets of basis functions are used, each containing six functions (such that $k = 0$–5) and each centered at a different r_0. These r_0 correspond to the minima of each well in $\hat{V}_{PC}$ and are located at $r = 1$ Å for the covalent well and $r = 1.6$ Å for the ionic well.

For the reasons discussed at the end of Sec. 2.3.2, the form of the mapping Hamiltonian with $\overline{h}^{\lambda\lambda'}$ is used. If $h^{\lambda\lambda'}$ is used, numerical instabilities arise due to the relatively large magnitudes of the $h^{\lambda\lambda'}$ matrix elements over the course of a trajectory. Thus, the mapping Hamiltonian takes the form

$$H_m(x,X) = K_S + K_C + V_{SS}(R) + \frac{\text{Tr }\hat{h}}{N} + \frac{1}{2\hbar}\sum_{\lambda\lambda'}\overline{h}^{\lambda\lambda'}(R)(r_\lambda r_{\lambda'} + p_\lambda p_{\lambda'}), \tag{5.8}$$

where $\overline{h}^{\lambda\lambda'}(R)$ is given by

$$\overline{h}^{\lambda\lambda'}(R) = \epsilon_\lambda \delta_{\lambda\lambda'} + \langle\lambda|\hat{V}_{CS}(\hat{r}, R) + \hat{V}_{PS}(\hat{r}, R)|\lambda'\rangle - \delta_{\lambda\lambda'} \frac{\mathrm{Tr}\ \hat{h}}{N}. \tag{5.9}$$

It is clear from the previous equation that the coupling potential is given by

$$\hat{V}_c(\hat{r}, R) = \hat{V}_{CS}(\hat{r}, R, R_{AB}) + \hat{V}_{PS}(\hat{r}, R). \tag{5.10}$$

Taking all of the above details into consideration, simulations of the system are carried out by propagating an ensemble of trajectories for three different cluster sizes, viz., $N_s = 7$, 9, 11. Initial equilibrium configurations are prepared by first melting a face–centered cubic lattice configuration with velocity rescaling to obtain a kinetic temperature of 150 K and then equilibrating with microcanonical dynamics for 7 ps. Production runs of 50 ps are generated using microcanonical dynamics. The equations of motion are integrated using the velocity-Verlet-type algorithm prescribed by Eqs. 2.55 and 2.56 with a time step of 0.4 fs. The bonds in the complex and solvent are constrained using the RATTLE [197] and SHAKE [198] algorithms. Finally, in the event of an evaporation of the cluster, the trajectory is terminated.

5.2.2 Complex and Solvent Properties

In order to gain insight into the dynamics of this system, we monitor trajectories of the solvent polarization, distance between the complex's center of mass and the center of mass of the solvent molecules, and the mapping analogue of the position of the proton. These results are then compared qualitatively to the results of adiabatic dynamics simulations in Refs. [155] and [159], which are known to give a realistic picture of the dynamics.

To begin with, the solvent polarization is defined as

$$\Delta E(R) = \sum_{i,a} Q_a e \left(\frac{1}{|R_i^a - s|} - \frac{1}{|R_i^a - s'|} \right), \tag{5.11}$$

where $Q_a e$ is the charge of atom a in molecule i (with $e = 1.602 \times 10^{-19}$C), and s and s' are points within the complex corresponding to the minima of $\hat{V}_{PC}$. As seen in Eq. 5.11, the solvent polarization is a collective solvent coordinate, which measures the difference between the solvent electric fields at points s and s'. Therefore, this quantity monitors the solvent dynamics as the complex switches between the covalent (lower values) and ionic states (higher values).

Secondly, the distance between the complex's center of mass and the center of mass of the solvent molecules (denoted by d) gives insight into the preferred positions of the complex within the cluster. When d is close to 0, i.e. both centres of mass overlapping, the complex is situated in the core of the cluster and is in its ionic state. Conversely, when d is large, the complex is situated on the surface of the cluster and is in its covalent state. This correlation between location and state occurs because a larger number of solvent molecules is required to stabilize complexes with larger dipole moments [154, 155, 199, 200].

Finally, because the proton is the key particle in the reaction, knowledge of its position along the course of the PT is desired. In the mapping representation, one can gain insight into the motion of the proton by monitoring the mapping analogue of the proton's position operator; according to Eq. 2.17, it is given by

$$q_m(x) = \sum_{\lambda\lambda'} q_{\lambda\lambda'} c_{\lambda\lambda'}(x), \tag{5.12}$$

where $q_{\lambda\lambda'} = \langle \lambda | \hat{q} | \lambda' \rangle$. It should be noted that, unless $c_{\lambda\lambda'}$ fulfills the requirement given by Eq. 2.32, the dynamics of the mapping variables (x) can take place outside of the physical

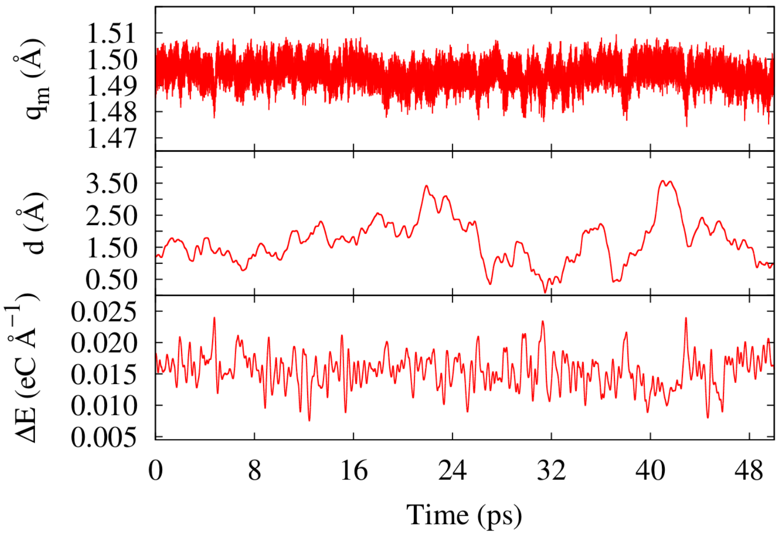

Figure 5.2: The protonic position in the mapping space, q_m, (top) the distance between the centers of mass of the complex and solvent, d, (middle) and the solvent polarization, ΔE, (bottom) along a representative trajectory of the $N_s = 11$ cluster.

space. For this reason, q_m may provide a "rough" probe of the motion of the proton.

Results for ΔE, d, and q_m along a representative trajectory of the system are presented in Figure 5.2. In this case, $N_s = 11$ and, therefore, the system is expected to exhibit a bistable behaviour with the ionic form of the complex being more stable [155]. As can be seen, none of these quantities clearly capture the expected bistability. In particular, both q_m and ΔE primarily fluctuate around some mean values (viz., $\langle q_m \rangle \approx 1.495$ Å and $\langle \Delta E \rangle \approx 0.017$ eC/Å), with q_m fluctuating on a faster time scale than ΔE ($\approx$ 10 fs for q_m and $\approx$ 200 fs for ΔE), as expected. Occasional hops in q_m to lower values are observed, but these values do not persist for more than a few picoseconds. Most of these hops are accompanied by the expected structural changes in the cluster, namely, a decrease in d and an increase in ΔE, indicative of the system becoming more ionic in character. In addition, the ranges of d and ΔE values explored by the system (i.e., approximately $0 < d < 4.0$

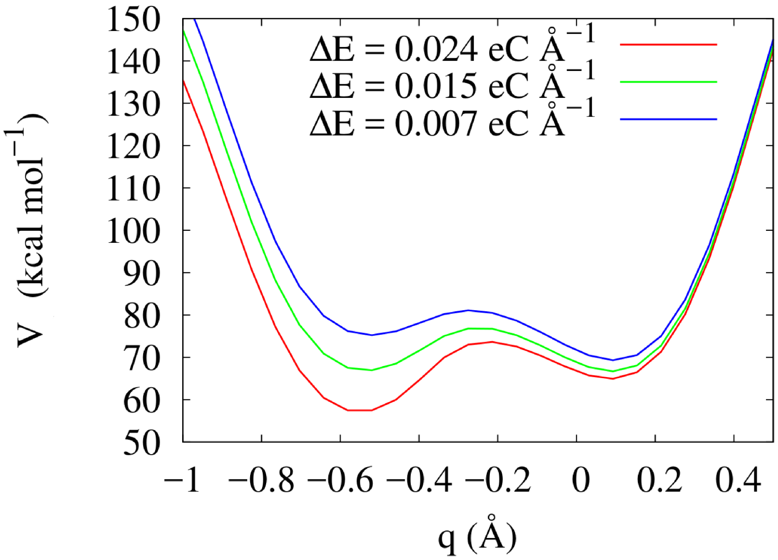

Figure 5.3: The potential energy (V) for three different solvent configurations, corresponding to low, intermediate, and high values of the solvent polarization for the $N_s = 11$ cluster.

Å and $0.010 < \Delta E < 0.020$ eC Å^{-1}) mainly correspond to the intermediate values observed in the adiabatic simulations (i.e., approximately $0 < d < 12$ Å and $0 < \Delta E < 0.030$ eC Å^{-1}) [155].

Based on Fig. 5.2, one sees that PBME dynamics is not capable of accessing either the covalent or ionic wells observed in the adiabatic dynamics simulations (situated at $d \approx 4.5$ Å and $\Delta E \approx 0.005$ eC Å^{-1} for the covalent well, and $d \approx 1.5$ Å and $\Delta E \approx 0.023$ eC Å^{-1} for the ionic well [155]). This ability to sample a "bit" of both states is consistent with the fact that PBME dynamics is mean-field-like. Nevertheless, as seen in Fig. 5.2, PBME is capable of capturing the expected qualitative trends in ΔE and d associated with the PT. This is supported by the fact that the potential $\hat{V} = \hat{V}_{CS}(\hat{r}, R) + \hat{V}_{PS}(\hat{r}, R) + \hat{V}_{PC}(\hat{r}; R_{AB})$ behaves in the expected way over a range of ΔE values, as shown in Fig. 5.3. In this figure, $V(q, R)$ is plotted for three representative snapshots of the $N_s = 11$ cluster, corresponding to large, intermediate, and small solvent polarizations, i.e., $\Delta E = 0.024$, 0.016, and 0.007,

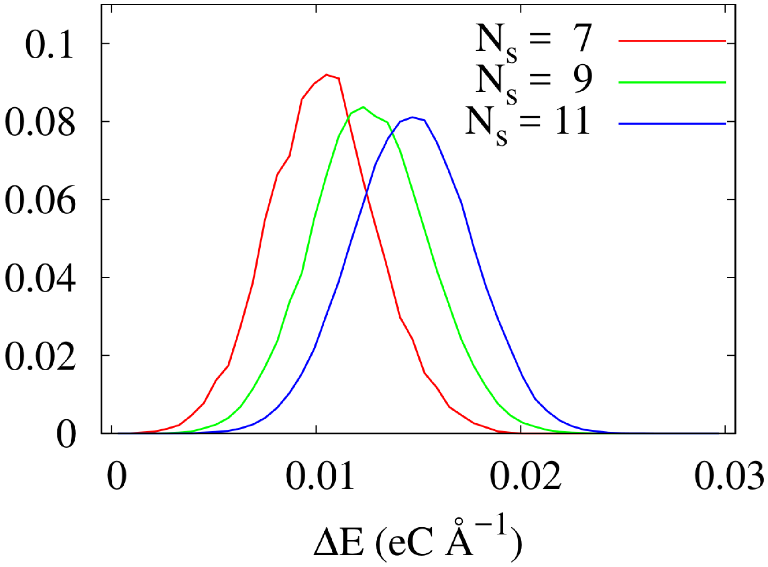

Figure 5.4: Histograms of the solvent polarization, ΔE, for the $N_s = 7$, 9, and 11 clusters.

respectively. These ΔE values were chosen because they correspond to the ionic, barrier-top, and covalent configurations of the complex, respectively, observed in the adiabatic dynamics simulations [155]. It can be seen that as ΔE increases, the ionic well (at $q \approx -0.55$Å) becomes more stable at the expense of the covalent well (at $q \approx 0.1$Å), which is exactly what is observed in the adiabatic dynamics simulations. Thus, although the potential switches between being primarily ionic and primarily covalent in character, the overall PBME potential is still mean-field-like. Similar behaviours are observed for the smaller clusters and, therefore, those results are not shown.

Histograms of the solvent polarization and the distance between the centers of mass of the complex and solvent for all three cluster sizes (generated from an ensemble of 180 trajectories per cluster) are presented in Figs. 5.4 and 5.5, respectively. As the number of solvent molecules is increased from $N_s = 7$ to $N_s = 11$, it can be seen that the maximum of the solvent polarization histogram (Fig. 5.4) shifts to higher polarization values, namely,

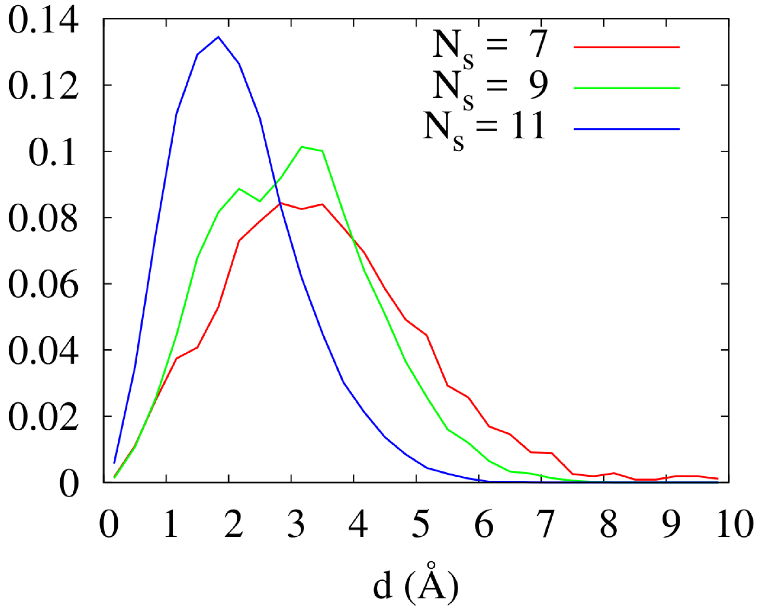

Figure 5.5: Histograms of the distance between the centers of mass of the complex and solvent, d for the $N_s = 7$, 9, and 11 clusters.

from ≈ 0.009 eC Å^{-1} for $N_s = 7$ to ≈ 0.012 eC Å^{-1} for $N_s = 9$ to ≈ 0.016 eC Å^{-1} for $N_s = 11$. This indicates that the solvent becomes increasingly polarized on average, which in turn is a sign that complexes with more ionic character become increasingly stable as the size of the cluster increases. This observation is consistent with the previous trend for this model obtained by adiabatic dynamics [155]. However, in stark contrast to the results in Ref. [155], the PBME histograms are unimodal whereas the adiabatic ones are bimodal (due to the existence of stable covalent and ionic wells), and the maxima of the PBME histograms lie in the central regions of the adiabatic ones.

In the case of the d histograms, as the number of solvent molecules is increased from $N_s = 7$ to $N_s = 11$, it can be seen that the maximum of each histogram shifts to lower d values, namely, from ≈ 3.2 Å for $N_s = 7$ to ≈ 2.8 Å for $N_s = 9$ to ≈ 1.8 Å for $N_s = 11$. This indicates that the complex prefers to reside closer to the center of mass of the solvent as the size of the cluster increases. Again, this behaviour is consistent with what is observed in the previous adiabatic simulations, except for the fact that the PBME histograms are unimodal whereas the adiabatic ones are bimodal. The unimodal character of the ΔE and d histograms is a clear testament to the mean-field nature of the PBME dynamics, which is due to the mixing of ground- and excited-subsystem state potentials (see the summation in the last term of Eq. 5.8). As a consequence, the system cannot switch completely between the two stable configurations of the system observed in the adiabatic dynamics simulations.

To gain insight into the correlation between the solvent polarization and the position of the complex within the cluster, joint histograms of d and ΔE were calculated for all three cluster sizes. These histograms, shown in Fig. 5.6, demonstrate that the more polarized the cluster is, the closer the complex will reside to the center of mass of the solvent, irrespective of the cluster size. In contrast to the two peaks observed in the joint histograms calculated via adiabatic dynamics [155], these histograms contain only one peak. Hence, the picture of the reaction dynamics given by the PBME method is very different than that given by adiabatic dynamics, in which the PT reaction involves diffusion of the complex from the surface to the interior of the cluster and vice versa. PBME dynamics cannot effectively capture these excursions of the complex, especially in the larger clusters.

To gain insight into the correlation between the protonic motion and the solvent dynamics, the joint histograms of q_m and ΔE are presented in Fig. 5.7 for all three cluster sizes. For the $N_s = 7$ and $N_s = 9$ clusters, there is no distinct correlation between q_m and ΔE. However, for $N_s = 11$, q_m and ΔE are negatively correlated, i.e., as ΔE increases, q_m decreases. This negative correlation is consistent with what is seen in the adiabatic dynamics of the proton in physical space, where the mean position of the proton tends towards the B group as the solvent polarization increases. However, the inability of the PBME dynamics to capture this behaviour in the smaller clusters suggests that the protonic

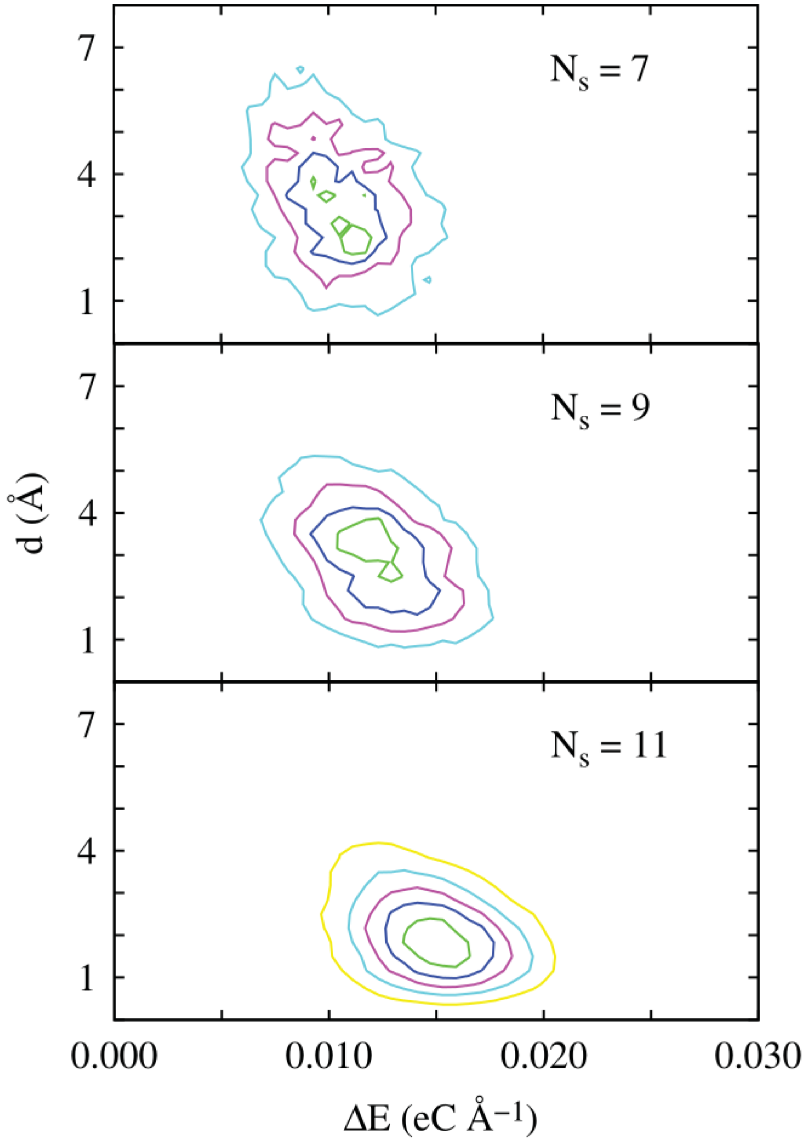

Figure 5.6: Joint histograms of the distance between the centers of mass of the complex and solvent, d, and the solvent polarization, ΔE, for the N_s = 7, 9, and 11 clusters (from top to bottom).

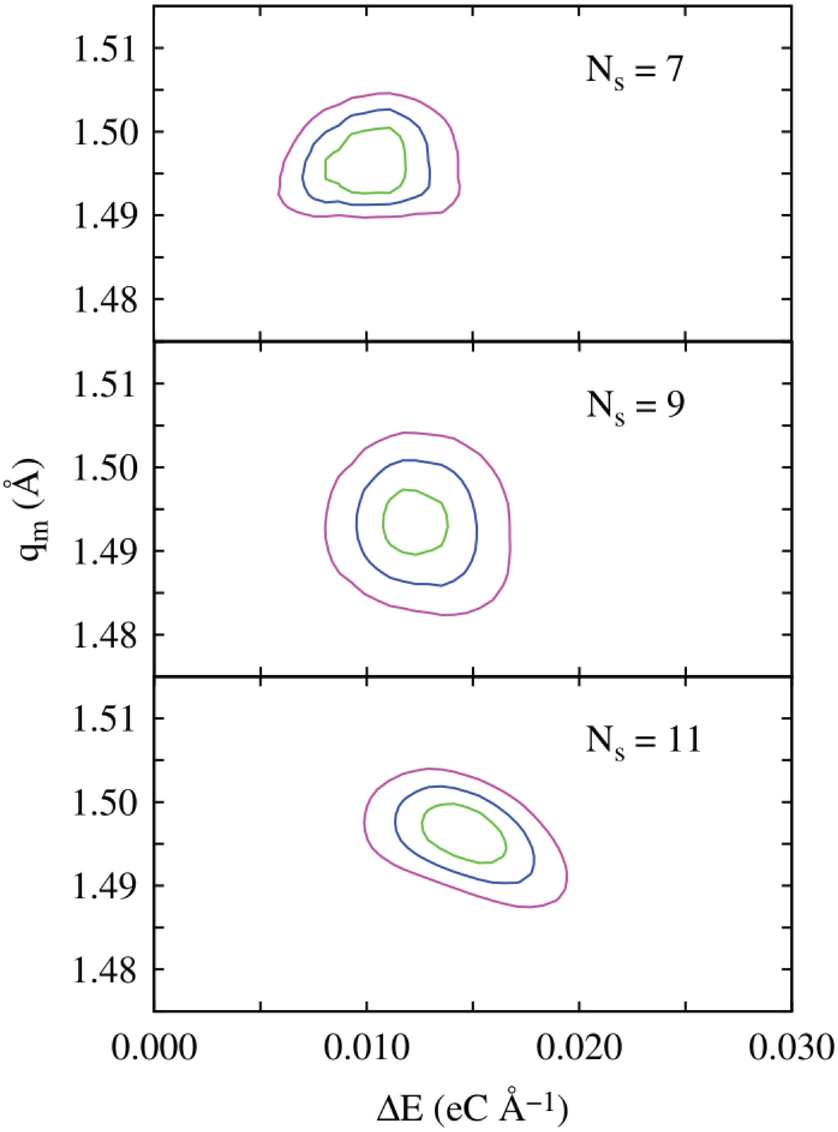

Figure 5.7: Joint histograms of the mapping analogue of the protonic position, q_m, and the solvent polarization, ΔE, for the $N_s = 7$, 9, and 11 clusters (from top to bottom).

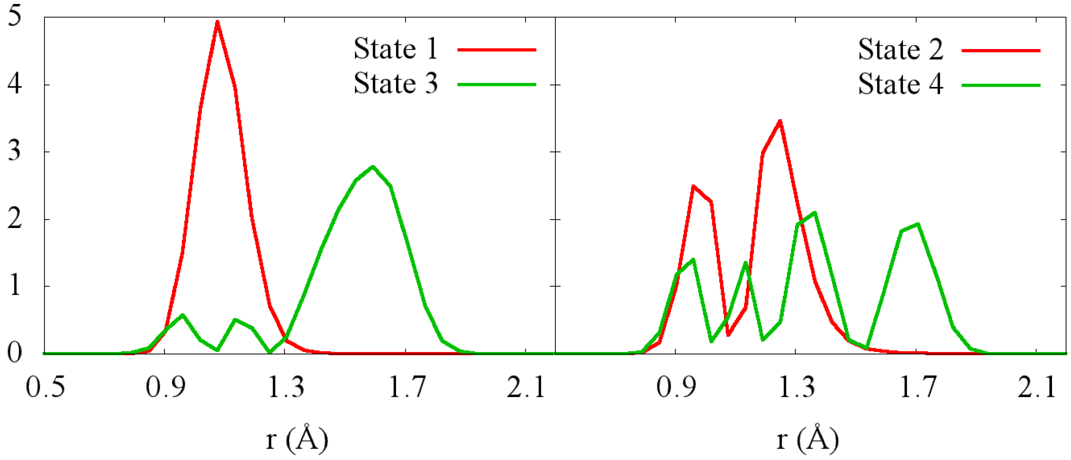

Figure 5.8: The first four subsystem state probability distributions, $\lambda^2(r)$, as a function of the A–H distance, r.

motion in the mapping space (as monitored by q_m) does not provide an accurate mapping of the motion in the physical space. This due to the fact that, like the Hamiltonian, q_m has contributions from the expectation values of the position of the proton in the ground- and excited-subsystem states (see Eq. 5.12 and the definition of $q_{\lambda\lambda'}$ that follows). For this reason, and owing to the fast oscillatory behaviour of $c_{\lambda\lambda'}(x)$, it is impossible for q_m to represent the position of the proton in the physical space accurately.

5.2.3 Character of Protonic Subsystem States

We now briefly discuss the character of the subsystem states, $\{|\lambda\rangle\}$, used in the PBME dynamics simulations of the system. Specifically, the subsystem states are used to compute the matrix elements of the Hamiltonian, forces, and observable operators.

In Fig. 5.8, the probability distributions, $\lambda^2(r)$, are plotted as a function of the A–H distance, r, for the first four subsystem states, i.e. the ones used for the calculations in this Chapter. These plots describe the probability of finding the proton at position r while in state $|\lambda\rangle$. As can be seen, the probability distribution associated with the first subsystem state, $|1\rangle$, has a maximum at 1 Å, which corresponds to the minimum of the covalent well in the hydrogen bonding potential. The probability distribution associated with the third subsystem state, $|3\rangle$, has a mainly ionic character but also a non-negligible covalent character. On the other hand, the probability distribution associated with the second ($|2\rangle$) and fourth ($|4\rangle$) subsystem states are quite delocalized. It should be noted that none of the probability distributions have maxima corresponding directly to the minimum of the ionic well (at 1.6 Å) in the hydrogen bonding potential. This is due to the fact that, in the absence of the coupling to the solvent, the complex cannot be stabilized in the ionic state. In the following section, we will see how the characters of these distributions can distinctly impact the shape of a free energy profile when a quantum reaction coordinate is chosen.

5.3 Reaction Coordinates and Free Energy Calculations

In this section, expressions for calculating free energy profiles using PBME dynamics are derived. The expressions are then used to calculate free energy profiles for the PT reaction based on two different reaction coordinates, one quantum and one classical. The differences between these profiles are discussed.

To gain insight into the energetics of a reaction, one may examine its free energy along a suitable reaction coordinate, i.e., a function that monitors the progress of the reaction. This reaction coordinate may either be classical or quantum mechanical in character, depending on the nature of the reaction. In the case of a PT reaction in a polar nanocluster, there are three potentially viable reaction coordinates: the solvent polarization, proton position, and distance between the center of mass of the complex and the center of mass of the solvent (see Section 5.2.1). In this work, we consider the solvent polarization (a classical coordinate) and the proton position (a quantum coordinate), and study the ability of the PBME approach to capture the expected features in the free energy profiles for both reaction coordinates.

For a general reaction coordinate ξ (which may be a quantum operator, a function of the classical configuration, or a combination of the two), the free energy, W, may be defined according to the following statistical mechanical expression:

$$\beta W(\xi') = -\ln\langle\delta(\xi-\xi')\rangle, \tag{5.13}$$

where $\beta = 1/k_BT$ and $\langle\ldots\rangle$ denotes an expectation value. In the following subsections, we show how this expectation value may be calculated using the PBME method.

5.3.1 PBME Approach

Using the PBME approach, the expectation value in Eq. 5.13 is given by

$$\langle\delta(\xi-\xi')\rangle = \int dxdX\ (\delta(\xi-\xi'))_m\tilde{\rho}_m(x,X), \tag{5.14}$$

where $(\delta(\xi-\xi'))_m$, the mapping analogue of the delta function, may be obtained by applying Eq. 2.17:

$$(\delta(\xi-\xi'))_m = \sum_{\lambda\lambda'}\langle\lambda|\delta(\xi-\xi')|\lambda'\rangle c_{\lambda\lambda'}(x). \tag{5.15}$$

Up to this point, the form of ξ has not been established, but depending on whether ξ is a function of classical or quantum mechanical variables, the evaluation of Eq. 5.15 will differ. When the reaction coordinate is taken to be the solvent polarization, a purely classical quantity, $\xi \equiv \xi(R) = \Delta E(R)$, and therefore it can be factored out of the sum in Eq. 5.15, resulting in the following expression:

$$(\delta\left(\Delta E(R)-\Delta E'\right))_m = \delta\left(\Delta E(R)-\Delta E'\right)\sum_{\lambda}c_{\lambda\lambda}(x). \tag{5.16}$$

However, when the reaction coordinate is taken to be the proton position, a quantum mechanical variable, $\xi \equiv r$, and therefore the matrix elements of Eq. 5.15 must be evaluated, resulting in the following expression:

$$(\delta(r-r'))_m = \sum_{\lambda\lambda'} \langle\lambda|\delta(r-r')|\lambda'\rangle c_{\lambda\lambda'}(x), \tag{5.17}$$

where

$$\begin{aligned}\langle\lambda|\delta(r-r')|\lambda'\rangle &= \int dr\ \lambda(r)\delta(r-r')\lambda'(r)\\ &= \lambda(r')\lambda'(r'). \end{aligned} \tag{5.18}$$

Upon substituting Eqs. 5.16 and 5.17 into Eq. 5.14, the expressions for the averages become

$$\langle\delta\left(\Delta E(R)-\Delta E'\right)\rangle = \int dxdX\ \delta\left(\Delta E(R)-\Delta E'\right)\left(\sum_{\lambda} c_{\lambda\lambda}(x)\right)\tilde{\rho}_m(x,X) \tag{5.19}$$

for the solvent polarization, and

$$\langle\delta(r-r')\rangle = \int dxdX\ \left(\sum_{\lambda\lambda'} \lambda(r')\lambda'(r')c_{\lambda\lambda'}(x)\right)\tilde{\rho}_m(x,X) \tag{5.20}$$

for the proton position, respectively. The upper limits of the sums in these expressions depend on the number of subsystems states that are included in the calculation. The mapping analogue of the density matrix, $\tilde{\rho}_m(x,X)$, appearing in Eqs. 5.19 and 5.20, is given by Eq. 2.27. In this work, we have replaced the equilibrium Wigner distribution with its high-temperature approximation, i.e.

$$\rho_W^{\lambda\lambda'} \approx \frac{e^{-\beta H^{\lambda\lambda'}}}{\int dX \sum_{\lambda\lambda'} e^{-\beta H^{\lambda\lambda'}}}. \tag{5.21}$$

This is a reasonable approximation for the system at hand, given that its temperature is relatively high. In addition, this approximation greatly simplifies the sampling of the initial conditions of the classical environment. In addition, we have assumed that the excited subsystem states are negligibly populated, such that

$$\rho_W^{\lambda\lambda'} = \begin{cases} \frac{e^{-\beta H^{11}}}{\int dX \sum_{\lambda\lambda'} e^{-\beta H^{\lambda\lambda'}}} & \text{if } \lambda = \lambda' = 1 \\ 0 & \text{in any other case.} \end{cases} \tag{5.22}$$

To sample the initial conditions from the density matrix in Eq. 5.22, it is first convenient to rewrite it as follows:

$$\rho_W^{11} = \frac{e^{-\beta H^{11}}}{\int dX \sum_{\lambda\lambda'} e^{-\beta H^{\lambda\lambda'}}} = \frac{e^{-\beta H^{11}}}{\int dX e^{-\beta H^{11}}} \times \frac{\int dX e^{-\beta H^{11}}}{\int dX \sum_{\lambda\lambda'} e^{-\beta H^{\lambda\lambda'}}}. \tag{5.23}$$

Noting that

$$\sum_{\lambda\lambda'} e^{-\beta H^{\lambda\lambda'}} = e^{-\beta H^{11}} \left(1 + \sum_{\lambda\neq 1} e^{-\beta(H^{\lambda\lambda} - H^{11})} + \sum_{\lambda\neq\lambda'} e^{-\beta(H^{\lambda\lambda'} - H^{11})} \right) \tag{5.24}$$

we may rewrite Eq. 5.23 as

$$\rho_W^{11} = \frac{e^{-\beta H^{11}}}{\int dX e^{-\beta H^{11}}} \times \frac{1}{\langle 1 + \sum_{\lambda\neq 1} e^{-\beta(H^{\lambda\lambda} - H^{11})} + \sum_{\lambda\neq\lambda'} e^{-\beta(H^{\lambda\lambda'} - H^{11})} \rangle_{11}}, \tag{5.25}$$

where $\langle \ldots \rangle_{11} = \frac{\int dX e^{-\beta H^{11}} \ldots}{\int dX e^{-\beta H^{11}}}$ denotes a ground-state average. Under these conditions,

$\tilde{\rho}_m(x, X)$ becomes

$$\tilde{\rho}_m(x, X) = \frac{2}{\hbar(\pi\hbar)^N} e^{-x^2/\hbar} \left(r_1^2 + p_1^2 - \frac{\hbar}{2} \right) \frac{e^{-\beta H^{11}}}{\int dX e^{-\beta H^{11}}} \\ \times \frac{1}{\langle 1 + \sum_{\lambda \neq 1} e^{-\beta(H^{\lambda\lambda} - H^{11})} + \sum_{\lambda \neq \lambda'} e^{-\beta(H^{\lambda\lambda'} - H^{11})} \rangle_{11}}. \tag{5.26}$$

Based on Eqs. 5.19 to 5.26, one sees how to generate the free energy profiles using PBME dynamics. The phase space integrals in Eqs. 5.19 and 5.20 may be evaluated as follows:

1. Sample the initial values of the mapping variables, x, according to the Gaussian distribution in Eq. 5.26.

2. Sample the initial positions and momenta of the classical DOF from a long constant temperature PBME trajectory generated using the Hamiltonian H^{11}, i.e. a trajectory restricted to the ground subsystem state, in accordance with the bath part of the initial density matrix in Eq. 5.26.

3. Starting from these initial conditions, propagate the system in time by solving the PBME equations of motion (Eq. 2.25) using the states obtained from solving the subsystem eigenvalue problem. In practice, only a subset of the subsystem states may contribute appreciably to the dynamics, so one may truncate the full set of states to reduce the simulation time. (The number of subsystem states needed can be determined by computing the free energy profile using increasing numbers of states and checking for convergence.) Calculate $c_{\lambda\lambda'}$ and ξ along each trajectory in the ensemble.

4. When $\xi = \Delta E$, the average in Eq. 5.19 can be obtained by histogramming the values of $\Delta E(R)$ explored by the ensemble of trajectories, into bins centered at the various

$\Delta E'$ values. However, instead of adding 1 to the bin each time $\Delta E(R) = \Delta E'$, one adds the corresponding value of the $\sum_\lambda c_{\lambda\lambda}$ factor. When $\xi = r$, the average in Eq. 5.20 can be obtained by evaluating $\sum_{\lambda\lambda'} \lambda(r')\lambda'(r')c_{\lambda\lambda'}(x)$ at each time step of each trajectory and then averaging this quantity over all time steps in the ensemble of trajectories. The $\lambda(r') = \langle r|\lambda\rangle$ appearing in Eq. 5.20 may be evaluated using Eqs. 5.6 and 5.7 for every value of r'.

5. The free energy is finally obtained by multiplying the average from the previous step by the factor on the second line of Eq. 5.26 (evaluated during the sampling of the initial conditions from the trajectory restricted to the ground subsystem state) and then taking the negative logarithm of the result.

5.3.2 Free Energy Profiles

Before presenting the free energy profiles for the PT reaction, we describe the simulation details for computing the free energy profiles for the $N_s = 7$ cluster. The initial conditions of the cluster and complex were sampled from a 1 ns trajectory on the ground subsystem state, i.e. using H^{11} in accordance with Eq. 5.26. The first four (out of twelve) subsystem states were used in the production dynamics (as the higher lying states were found to contribute negligibly to the final results). The equations of motion were integrated using the velocity-Verlet-type algorithm prescribed by Eqs. 2.55 and 2.56, with a time step of 0.05 fs was used. All other parameters were the same as the ones used in Section 5.1.

The free energy profiles as a function of the solvent polarization (left panel) and protonic position (right panel) reaction coordinates for the $N_s = 7$ cluster are shown in Fig. 5.9. As can be seen, the two free energies present two very different pictures; when the reaction coordinate is chosen to be the (classical) solvent polarization, only a single well is observed, while when the (quantum) protonic position is chosen, one observes a predominantly double-

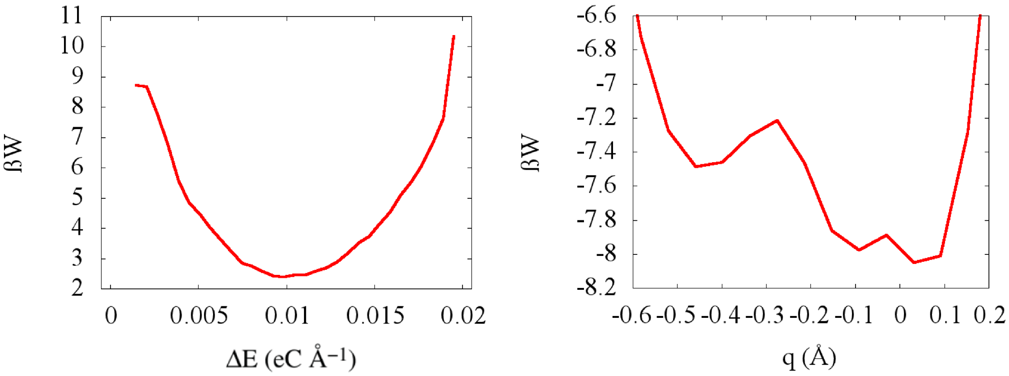

Figure 5.9: Free energy profiles along the solvent polarization (left) and proton position (right) reaction coordinates for the PT reaction in the $N_s = 7$ cluster, calculated using PBME dynamics.

well profile. The first result is in stark contrast with those obtained in previous studies based on adiabatic-QCLE simulations [68, 155], where use of the solvent polarization reaction coordinate yields a clearly double-well free energy profile, as is expected for charge transfer reactions occurring in hydrogen-bonded complexes that are dissolved in a polar solvent. The inability of PBME dynamics to capture the expected bistable behaviour when the solvent polarization (a purely classical reaction coordinate) is used, is due to the fact that the classical DOF experience forces derived from a mean-field-like potential that essentially mixes the potentials associated with the covalent and ionic forms of the complex. Therefore, the solvent polarization is not a suitable reaction coordinate when PBME dynamics is used to compute the free energy. In contrast, the free energy as a function of the protonic position has a double-well profile, suggesting that a quantum reaction coordinate is more suitable when PBME dynamics is used. It should be noted that the free energy change, ΔG_{rxn}, and barrier height, $\Delta G^{\ddagger}$, are different from the previously reported values of $\Delta G_{\mathrm{rxn}} \approx 1.3/\beta$ and $\Delta G^{\ddagger} \approx 5/\beta$, respectively, in Ref. [155]. These differences are likely due to the different methods and reaction coordinates used.

Chapter 6

Conclusions and Future Work

The modeling of large chemical systems is feasible more than ever due to the rapid progress of computer technology. Ground-state dynamics simulations are now commonplace and are frequently used to complement information obtained from experiments or as a predictive tool. Such simulations rely on the Born-Oppenheimer approximation; however, many chemical processes of interest are not confined to the ground state or a single potential energy surface. This has prompted the development of methods for simulating the dynamics of a system when the Born-Oppenheimer approximation breaks down. Unfortunately, as the size of the system grows, fully quantum dynamical methods quickly become intractable. Therefore, developmental work has focused on methods capable of efficiently treating larger systems. One way to accomplish this is by introducing approximations into exact or inexact (but highly accurate) methods. In doing so, simplified and faster algorithms are obtained; however, one must understand for which systems and/or under which conditions these algorithms work best, in order to minimize the error introduced by the approximations. The work presented in this thesis was an investigation of this idea.

In this thesis, our interest was in algorithms that are derived from the QCLE, which is known to be an accurate equation of motion for simulating the dynamics of mixed quantum-classical systems. Because the solution of the QCLE becomes increasingly difficult as the quantum subsystem size and simulation time grow, approximate solutions have been developed to alleviate these difficulties. Our work focused on testing the validity of two approximate solutions, namely the PBME solution and the FBTS, for simulating the dynamics and spectroscopy of a variety of charge transfer processes.

Firstly, formalisms for calculating pump-probe TA signals using PBME and FBTS were laid out. These formalisms were based on the EOM-PMA, a general approach that can be used to calculate any type of nonlinear spectroscopic signal. The main advantage of EOM-PMA is that it avoids the often costly calculation of ORFs. However, using this approach, one must generate an ensemble of at most $2^{N_p} - 1$ trajectories (where N_p is the number of laser pulses employed in the spectroscopic technique) in order to extract the appropriate component of the polarization corresponding to the nonlinear signal of interest. In our work, we exploited the computational efficiency of the PBME and FBTS methods for generating these trajectories. The PBME-PMA and FBTS-PMA approaches were then tested on a model PIET reaction. By comparing to the numerically exact results for the TA signals in this model, the performances of our combined approaches were assessed. Under weak subsystem–bath coupling conditions, the results of these approaches were in reasonable agreement with the exact results, while under relatively strong coupling conditions, the agreements started to break down. This was expected, as the underlying approximations of both the PBME and FBTS methods were previously shown to improve with decreasing subsystem–bath coupling.

As a second step, the PBME-PMA and FBTS-PMA approaches were tested on a more complex PIET model, in which the ET complex is coupled to an inner-sphere vibrational mode. Unlike the simpler model, two different subsystem–bath decompositions of the system were possible, which depended on whether or not the vibrational mode is included in the quantum subsystem. For the classical treatment of the vibrational mode, the simulation details were essentially the same as those used in the treatment of the simpler model, with the exception of an additional classical DOF. However, the situation is somewhat more complex for the quantum treatment of the vibrational mode, and so we worked out the necessary theoretical/simulation details to carry it out. In this case, the resulting manifold of subsystem states reflects the vibronic nature of the system. In the end, the results showed that no single method was able to capture all of the features of the pump-probe TA signals; reliable information about the vibrational dynamics could be extracted from the TA signals, but none of the methods were able to fully capture the signal decay observed in the numerically exact results.

The PBME method was also used to simulate the dynamics of a more realistic model of a charge transfer reaction, namely a PT reaction in a phenol–trimethylamine complex dissolved in a polar nanocluster. Our work constituted one of the first applications of PBME dynamics to a realistic system. This system represented an extreme case for testing the limits of the PBME approach, given the prevalence of electrostatic interactions between the dipoles in the system. In our simulations, the transferring proton was treated quantum mechanically, while the rest of the system (i.e. complex and cluster molecules) was treated classically. We started by following the dynamical behaviour of various complex and cluster properties in an ensemble of PBME trajectories. Interestingly, PBME dynamics was not capable of exploring the expected cluster configurations associated with the covalent and ionic states of the phenol–trimethylamine complex. Instead, PBME dynamics generated stable cluster configurations that are neither distinctly covalent or distinctly ionic in character, but rather have mixed characters. This behaviour was attributed to the fact that the overall potential governing the PBME dynamics is a sum over potentials that localize the system in both the covalent and ionic wells. Our results highlighted the mean-field-like nature of the PBME method for describing the dynamics of the classical DOF. We then went on to derive PBME-based expressions for the free energy along both classical and quantum reaction coordinates, namely the solvent polarization and protonic position, respectively. The free energy profile obtained using the classical reaction coordinate had a single well, reflecting once again the mean-field-like potential experienced by the classical DOF in the PBME dynamics. In contrast, the use of a quantum reaction coordinate yields the expected double-well character of the free energy profile. This is due to the fact that the values of r, ranging from the covalent to the ionic well, are used to calculate the $\lambda(r)$'s in Eq. 5.20 and thus contributions to the ionic well are always taken into account (despite the fact that the solvent molecules do not explore values of ΔE that distinctly correspond to the ionic well). Overall, our result suggests that it is possible to obtain reasonable free energy profiles using the PBME method for strongly coupled systems, as long as one could identify a good quantum reaction coordinate.

Based on the results in this thesis, the following general picture emerges: (i) The approximate solutions of the QCLE give rise to more efficient algorithms with better convergence properties compared to the surface-hopping solutions of the QCLE. (ii) They give rise to algorithms that can be easily integrated into larger molecular dynamics codes (as the quantum DOF are described in terms of continuous variables whose evolution is classical-like). (iii) The main downside is the breakdown of the approximations as the coupling between the subsystem and environment increases. (iv) If there is a bias (or asymmetry) in the energies of the subsystem states, the approximate solutions may struggle to yield accurate results. This is due to the inability of the potentials to capture the dynamics induced by the asymmetries in the Hamiltonian. For this reason, the use of the traceless form of the Hamiltonian is necessary in more complex systems, as it helps to tame dynamical instabilities. (v) The performance of PBME is affected by the form of the observable; namely, PBME struggles to capture the correct dynamics when diagonal operators are involved. This is due to the $-\hbar$ term found in the expression for the mapping analogue of an operator, which can render the observable more sensitive to trajectories that take the mapping variables out of their physical space.

In contrast to the QCLE-based surface-hopping algorithms, PBME and FBTS can struggle to accurately capture the dynamics of observables for the systems and conditions encountered in this thesis. That being said, their efficiency and ease of implementation warrant the development of improvements which expand their domain of applicability, e.g. the improvements proposed in Refs. [84] and [85] for PBME and in Ref. [86] for FBTS. Testing these improvements on the systems studied in this thesis would be a worthwhile endeavour. It would also be worthwhile to develop an entirely new approximate solution of the QCLE and an algorithm for simulating such an approximation. The fact that the PBME and FBTS approaches yield classical-like equations of motion for the quantum DOF, makes them suitable candidates for incorporation into open source MD codes such as LAMMPS or GROMACS. Doing so could expand the applicability of PBME/FBTS to complex systems by allowing for the treatment of atomistically explicit classical environments. This will be particularly important when studying large systems in which nonadiabatic effects are pronounced, such as those encountered in applications to the design of more efficient photovoltaic and semiconductor technologies.

Bibliography

[1] E. B. Davies. *Quantum Theory of Open Systems.* Academic-Press, London, 1976.

[2] E. B. Davies and H. Spohn. Open quantum systems with time-dependent Hamiltonians and their linear response. *J. Stat. Phys.*, 19:511, 1978.

[3] U. Weiss. *Quantum dissipative systems.* World Scientific, London, 1993.

[4] H.D. Meyer, U. Manthe, and L. S. Cederbaum. The multi-configurational time-dependent Hartree approach. *Chem. Phys. Lett.*, 165(1):73–78, 1990.

[5] U. Manthe, H. D. Meyer, and L. S. Cederbaum. Wave-packet dynamics within the multiconfiguration Hartree framework: General aspects and application to NOCl. *J. Chem. Phys.*, 97(5):3199–3213, 1992.

[6] M. H. Beck, A. Jäckle, G. A. Worth, and H. D. Meyer. The multiconfiguration time-dependent Hartree (mctdh) method: a highly efficient algorithm for propagating wavepackets. *Phys. Rep.*, 324(1):1–105, 2000.

[7] H Köppel, M Döscher, I Bâldea, H-D Meyer, and PG Szalay. Multistate vibronic interactions in the benzene radical cation. ii. quantum dynamical simulations. *J. Chem. Phys.*, 117(6):2657–2671, 2002.

[8] M Nest and H-D Meyer. Dissipative quantum dynamics of anharmonic oscillators with the multiconfiguration time-dependent hartree method. *J. Chem. Phys.*, 119(1): 24–33, 2003.

[9] J. Cao and G. A. Voth. The formulation of quantum statistical mechanics based on the Feynman path centroid density. i. equilibrium properties. *J. Chem. Phys.*, 100(7): 5093–5105, 1994.

[10] J. Cao and G. A. Voth. The formulation of quantum statistical mechanics based on the Feynman path centroid density. ii. dynamical properties. *J. Chem. Phys.*, 100(7): 5106–5117, 1994.

[11] S. Jang and G. A. Voth. A derivation of centroid molecular dynamics and other approximate time evolution methods for path integral centroid variables. *J. Chem. Phys.*, 111(6):2371–2384, 1999.

[12] R. Ramírez and T. López-Ciudad. The Schrödinger formulation of the Feynman path centroid density. *J. Chem. Phys.*, 111(8):3339–3348, 1999.

[13] E. A. Polyakov, A. P. Lyubartsev, and P. N. Vorontsov-Velyaminov. Centroid molecular dynamics: Comparison with exact results for model systems. *J. Chem. Phys.*, 133(19):194103, 2010.

[14] I. R. Craig and David E D. E. Manolopoulos. Quantum statistics and classical mechanics: Real time correlation functions from ring polymer molecular dynamics. *J. Chem. Phys.*, 121(8):3368–3373, 2004.

[15] B. J. Braams and D. E. Manolopoulos. On the short-time limit of ring polymer molecular dynamics. *J. Chem. Phys.*, 125(12):124105, 2006.

[16] K. K. G. Smith, J. A. Poulsen, G. Nyman, and P. J. Rossky. A new class of ensemble conserving algorithms for approximate quantum dynamics: Theoretical formulation and model problems. *J. Chem. Phys.*, 142(24):244112, 2015.

[17] K. K. G. Smith, J. A. Poulsen, G. Nyman, A. Cunsolo, and P. J. Rossky. Application of a new ensemble conserving quantum dynamics simulation algorithm to liquid para-hydrogen and ortho-deuterium. *J. Chem. Phys.*, 142(24):244113, 2015.

[18] W. H. Miller. Classical S-matrix : Numerical application to inelastic collisions. *J. Chem. Phys.*, 53:3578, 1970.

[19] K. G. Kay. Semiclassical propagation for multidimensional systems by an initial value method. *J. Chem. Phys.*, 101:2250, 1994.

[20] K. G. Kay. Integral expressions for the semi-classical time-dependent propagator. *J. Chem. Phys.*, 100:4377, 1994.

[21] K. G. Kay. Numerical study of semiclassical initial value methods for dynamics. *J. Chem. Phys.*, 100:4432, 1994.

[22] X. Sun and W. H. Miller. Mixed semiclassical-classical approaches to the dynamics of complex molecular systems. *J. Chem. Phys.*, 106:916, 1997.

[23] G. Stock and M. Thoss. Semiclassical description of nonadiabatic quantum dynamics. *Phys. Rev. Lett.*, 78:578–581, 1997.

[24] X. Sun, H. Wang, and W. H. Miller. On the semiclassical description of quantum coherence in thermal rate constants. *J. Chem. Phys.*, 109:4190, 1998.

[25] H. Wang, X. Sun, and W. H. Miller. Semiclassical approximations for the calcula-

tion of thermal rate constants for chemical reactions in complex molecular systems. *J. Chem. Phys.*, 108:9726, 1998.

[26] X. Sun, H. Wang, and W. H. Miller. Semiclassical theory of electronically nonadiabatic dynamics: Results of a linearized approximation to the initial value representation. *J. Chem. Phys.*, 109:7064, 1998.

[27] E. Pollak and J. Liao. A new quantum transition state theory. *J. Chem. Phys.*, 108: 2733, 1998.

[28] H. Wang, M. Thoss, K. Sorge, R. Gelabert, X. Giménez, and W. H. Miller. Semiclassical description of quantum coherence effects and their quenching: A forward-backward initial value representation study. *J. Chem. Phys.*, 114:2562, 2001.

[29] W. H. Miller. The semiclassical initial value representation: A potentially practical way for adding quantum effects to classical molecular dynamics simulations. *J. Phys. Chem. A*, 105:2942, 2001.

[30] O. V. Prezhdo and V. V. Kisil. Mixing quantum and classical dynamics. *Phys. Rev. A*, 56:162, 1997.

[31] A. Donoso and C. C. Martens. Simulation of coherent nonadiabatic dynamics using classical trajectories. *J. Chem. Phys.*, 102:4291, 1998.

[32] J. C. Tully. Mixed quantum-classical dynamics. *Faraday Discuss.*, 110:407, 1998.

[33] R. Kapral and G. Ciccotti. Mixed quantum classical dynamics. *J. Chem. Phys.*, 110: 8919, 1999.

[34] A. Donoso and C. C. Martens. Semiclassical multistate Liouville dynamics in the adiabatic representation. *J. Chem. Phys.*, 112:3980, 2000.

[35] M. Santer, U. Manthe, and G. Stock. Quantum-classical Liouville description of multi-dimensional nonadiabatic molecular dynamics. *J. Chem. Phys.*, 114:2001, 2001.

[36] I. Horenko, C. Salzmann, B. Schmidt, and C. Schutte. Quantum-classical Liouville approach to molecular dynamics: Surface hopping Gaussian phase-space packets. *J. Chem. Phys.*, 117:11075–11088, 2002.

[37] M. J. Bedard-Hearn, R. E. Larsen, and B. J. Schwartz. Mean-field dynamics with stochastic decoherence (mf-sd): A new algorithm for nonadiabatic mixed quantum/classical molecular-dynamics simulations with nuclear-induced decoherence. *J. Chem. Phys.*, 123(23):234106, 2005.

[38] H. Kim and R. Kapral. *ChemPhysChem*, 9:470, 2008.

[39] S. A. Fischer, C. T. Chapman, and X. Li. *J. Chem. Phys.*, 135:144102, 2011.

[40] C.-Y. Hsieh and R. Kapral. Nonadiabatic dynamics in open quantum-classical systems: Forward-backward trajectory solution. *J. Chem. Phys.*, 137(22):22A507, 2012.

[41] H. M. Jaeger, S. Fischer, and O. V. Prezhdo. Decoherence-induced surface hopping. *J. Chem. Phys.*, 137(22):22A545, 2012.

[42] L. Wang, D. Trivedi, and O. V. Prezhdo. Global flux surface hopping approach for mixed quantum-classical dynamics. *J. Chem. Theory Comput.*, 10(9):3598–3605, 2014.

[43] R. Kapral. Quantum dynamics in open quantum-classical systems. *J. Phys. Condens. Matter*, 27(7):073201, 2015.

[44] L. Wang, A. E. Sifain, and O. V. Prezhdo. Fewest switches surface hopping in Liouville space. *J. Phys. Chem. Lett.*, 6(19):3827–3833, 2015.

[45] A. E. Sifain, L. Wang, and O. V. Prezhdo. Mixed quantum-classical equilibrium in global flux surface hopping. *J. Chem. Phys.*, 142(22):224102, 2015.

[46] J. C. Tully. Molecular dynamics with electronic transitions. *J. Chem. Phys.*, 93:1061, 1990.

[47] J. C. Tully. Nonadiabatic dynamics. In D. L. Thompson, editor, *Modern Methods for Multidimensional Dynamics Computations in Chemistry*, page 34. World Scientific, New York, 1998.

[48] F. Webster, E. T. Wang, P. J. Rossky, and R. A. Friesner. Stationary-phase surface hopping for nonadiabatic dynamics - two-state systems. *J. Chem. Phys.*, 100:4835–4847, 1994.

[49] E. R. Bittner and P. J. Rossky. Quantum decoherence in mixed quantum-classical systems: Nonadiabatic processes. *J. Chem. Phys.*, 103:8130–8143, 1995.

[50] E. R. Bittner, B. J. Schwartz, and P. J. Rossky. Quantum decoherence: a consistent histories treatment of condensed phase non-adiabatic quantum molecular dynamics. *J. Mol. Struct.: THEOCHEM*, 389:203–216, 1997.

[51] O. V. Prezhdo. Mean field approximation for the stochastic schrödinger equation. *J. Chem. Phys.*, 111:8366–8377, 1999.

[52] C. Brooksby and O. V. Prezhdo. Quantized mean-field approximation. *Chem. Phys. Lett.*, 346:463–469, 2001.

[53] A. W. Jasper, C. Zhu, S. Nangia, and D. G. Truhlar. *Faraday Discuss.*, 127:1, 2004.

[54] M. J. Bedard-Hearn, R. E. Larsen, and B. J. Schwartz. *J. Chem. Phys.*, 123:234106, 2005.

[55] J. E. Subotnik. Augmented Ehrenfest dynamics yields a rate for surface hopping. *J. Chem. Phys.*, 132(13):134112, 2010.

[56] J. E. Subotnik and N. Shenvi. A new approach to decoherence and momentum rescaling in the surface hopping algorithm. *J. Chem. Phys.*, 134(2):024105, 2011.

[57] N. Shenvi, J. E. Subotnik, and W. Yang. Phase-corrected surface hopping: Correcting the phase evolution of the electronic wavefunction. *J. Chem. Phys.*, 135(2):024101, 2011.

[58] N. Shenvi, J. E. Subotnik, and W. Yang. Simultaneous-trajectory surface hopping: A parameter-free algorithm for implementing decoherence in nonadiabatic dynamics. *J. Chem. Phys.*, 134(14):144102, 2011.

[59] P. V. Parandekar and J. C. Tully. Detailed balance in Ehrenfest mixed quantum-classical dynamics. *J. Chem. Theory Comput.*, 2(2):229–235, 2006.

[60] A. Bastida, C. Cruz, J. Zúñiga, A. Requena, and B. Miguel. The Ehrenfest method with quantum corrections to simulate the relaxation of molecules in solution: Equilibrium and dynamics. *J. Chem. Phys.*, 126(1):014503, 2007.

[61] J. R. Schmidt, P. V. Parandekar, and J. C. Tully. Mixed quantum-classical equilibrium: Surface hopping. *J. Chem. Phys.*, 129(4):044104, 2008.

[62] C. C. Martens and J. Fang. Semiclassical-limit molecular dynamics on multiple electronic surfaces. *J. Chem. Phys.*, 106:4918, 1997.

[63] A. Donoso, D. Kohen, and C. C. Martens. Simulation of nonadiabatic wave packet interferometry using classical trajectories. *J. Chem. Phys.*, 112:7345, 2000.

[64] S. Nielsen, R. Kapral, and G. Ciccotti. Non-adiabatic dynamics in mixed quantum-classical systems. *J. Stat. Phys.*, 101:225–242, 2000.

[65] C. Wan and J. Schofield. Mixed quantum-classical molecular dynamics: Aspects of multithreads algorithms. *J. Chem. Phys.*, 113:7047, 2000.

[66] C. Wan and J. Schofield. Exact and asymptotic solutions of the mixed quantum-classical Liouville equation. *J. Chem. Phys.*, 112:4447, 2000.

[67] D. MacKernan, R. Kapral, and G. Ciccotti. Sequential short-time propagation of quantum-classical dynamics. *J. Phys.: Condes. Matter*, 14:9069–9076, 2002.

[68] G. Hanna and R. Kapral. Quantum-classical Liouville dynamics of nonadiabatic proton transfer. *J. Chem. Phys.*, 122:244505, 2005.

[69] D. MacKernan, G. Ciccotti, and R. Kapral. Trotter-based simulation of quantum-classical dynamics. *J. Phys. Chem. B*, 112:424, 2008.

[70] H. Kim, A. Nassimi, and R. Kapral. Quantum-classical Liouville dynamics in the mapping basis. *J. Chem. Phys.*, 129(8):084102, 2008.

[71] A. Kelly, R. van Zon, J. M. Schofield, and R. Kapral. *J. Chem. Phys.*, 136:084101, 2012.

[72] C.-Y. Hsieh and R. Kapral. Analysis of the forward-backward trajectory solution for the mixed quantum-classical Liouville equation. *J. Chem. Phys.*, 138(13):134110, 2013.

[73] A. Kelly and T. E. Markland. Efficient and accurate surface hopping for long time nonadiabatic quantum dynamics. *J. Chem. Phys.*, 139(1):014104, 2013.

[74] A. Sergi, D. MacKernan, G. Ciccotti, and R. Kapral. Simulating quantum dynamics in classical environments. *Theor. Chem. Acc.*, 110:49–58, 2003.

[75] D. A. Uken, A. Sergi, and F. Petruccione. Filtering schemes in the quantum-classical Liouville approach to nonadiabatic dynamics. *Phys. Rev. E*, 88:033301, 2013.

[76] D. Dell'Angelo and G. Hanna. Self-consistent filtering scheme for efficient calculations of observables via the mixed quantum-classical Liouville approach. *J. Chem. Theory Comput.*, 12(2):477–485, 2016.

[77] D. Dell'Angelo and G. Hanna. Using multi-state transition filtering to improve the accuracy of expectation values via mixed quantum-classical Liouville dynamics. In *AIP Conf. Proc.*, volume 1790, page 020009. AIP Publishing, 2016.

[78] A. Nassimi, S. Bonella, and R. Kapral. *J. Chem. Phys.*, 133:134115, 2010.

[79] H. D. Meyer and W. H. Miller. unknown. *J. Chem. Phys.*, 70:3214, 1979.

[80] G. Stock. A semiclassical self consistent field approach to dissipative dynamics: The spin–boson problem. *J. Chem. Phys.*, 103:1561, 1995.

[81] R. Glauber. Coherent and incoherent states of the radiation field. *Phys. Rev.*, 131: 2766, 1963.

[82] G. Stock and M. Thoss. Classical description of nonadiabatic quantum dynamics. *Adv. Chem. Phys.*, 131:243, 2005.

[83] N. Rekik, C-Y Hsieh, H. Freedman, and G. Hanna. A mixed quantum-classical Liouville study of the population dynamics in a model photo-induced condensed phase electron transfer reaction. *J. Chem. Phys.*, 138:144106(1), 2013.

[84] H. W. Kim and Y. M. Rhee. Improving long time behavior of Poisson bracket mapping equation: A non-Hamiltonian approach. *J. Chem. Phys.*, 140(18):184106, 2014.

[85] H. W. Kim, W.G. Lee, and Y. M. Rhee. Improving long time behavior of Poisson bracket mapping equation: A mapping variable scaling approach. *J. Chem. Phys.*, 141(12):124107, 2014.

[86] C.-Y. Hsieh, J. Schofield, and R. Kapral. Forward–backward solution of quantum-classical Liouville equation in the adiabatic mapping basis. *Mol. Phys.*, 111(22-23): 3546–3554, 2013.

[87] M. R. Wasielewski. Photoinduced electron transfer in supramolecular systems for artificial photosynthesis. *Chem. Rev.*, 92(3):435–461, 1992.

[88] M. E. Michel-Beyerle. *The Reaction Center of Photosynthetic Bacteria Structure and Dynamics*. Springer Berlin Heidelberg, Berlin, Heidelberg, 1996. ISBN 978-3-642-61157-5.

[89] P. Piotrowiak. Photoinduced electron transfer in molecular systems: Recent developments. *Chem. Soc. Rev.*, 28(2):143–150, 1999.

[90] M. E. El-Khouly, O. Ito, P. M. Smith, and F. D'Souza. Intermolecular and supramolecular photoinduced electron transfer processes of fullerene–porphyrin/phthalocyanine systems. *J. Photochem. Photobiol. C*, 5(1):79–104, 2004.

[91] W. R. Duncan and O. V. Prezhdo. Theoretical studies of photoinduced electron transfer in dye-sensitized TiO $_2$. *Annu. Rev. Phys. Chem.*, 58(1):143–184, 2007.

[92] O. V. Prezhdo, W. R. Duncan, and V. V. Prezhdo. Photoinduced electron dynamics at the chromophore–semiconductor interface: A time-domain ab initio perspective. *Prog. Surf. Sci.*, 84(1):30–68, 2009.

[93] T. M. Clarke and J. R. Durrant. Charge photogeneration in organic solar cells. *Chem. Rev.*, 110(11):6736–6767, 2010.

[94] C. Deibel and V. Dyakonov. Polymer–fullerene bulk heterojunction solar cells. *Rep. Prog. Phys.*, 73(9):096401, 2010.

[95] A. Listorti, B. O'Regan, and J. R. Durrant. Electron transfer dynamics in dye-sensitized solar cells. *Chem. Mat.*, 23(15):3381–3399, 2011.

[96] K. Wynne, G. D. Reid, and R. M. Hochstrasser. Vibrational coherence in electron transfer: the tetracyanoethylene–pyrene complex. *J. Chem. Phys.*, 105(6):2287–2297, 1996.

[97] I. V. Rubtsov and K. Yoshihara. Vibrational coherence in electron donor- acceptor complexes. *J. Phys. Chem. A*, 103(49):10202–10212, 1999.

[98] S. A. Kovalenko, N. Eilers-Konig, T. A. Senyushkina, and N. P. Ernsting. Charge transfer and solvation of betaine-30 in polar solvents - A femtosecond broadband transient absorption study. *J. Phys. Chem. A*, 105:4834–4843, 2001.

[99] Y. Tanimura and A. Ishizaki. Modeling, calculating, and analyzing multidimensional vibrational spectroscopies. *Acc. Chem. Res.*, 42:1270, 2009.

[100] P. McRobbie and E. Geva. A benchmark study of different methods for calculating one- and two-dimensional optical spectra. *J. Phys. Chem. A*, 113:10425, 2009.

[101] N. E. Shemetulskis and R. F. Loring. Semiclassical theory of the photon echo: Application to polar fluids. *J. Chem. Phys.*, 97:1217, 1992.

[102] M. A. Sepúlveda and S. Mukamel. Semiclassical theory of molecular nonlinear optical polarization. *J. Chem. Phys.*, 102:9327, 1995.

[103] C. F. Spencer and R. F. Loring. Dephasing of a solvated two-level system: A semiclassical approach for parallel computing. *J. Chem. Phys.*, 105:6596, 1996.

[104] S. A. Pentidis and R. F. Loring. Calculation of the photon echo with mixed-state propagation. *Chem. Phys. Lett.*, 287:217, 1998.

[105] O. Kühn and N. Makri. Forward-backward semiclassical calculation of spectral line shapes: I_2 in a rare gas cluster. *J. Phys. Chem. A*, 103:9487, 1999.

[106] M. Ovchinnikov, V. A. Apkarian, and G. A. Voth. Semiclassical molecular dynamics computation of spontaneous light emission in the condensed phase: Resonance Raman spectra. *J. Chem. Phys.*, 184:7130, 2001.

[107] C. Dellago and S. Mukamel. Simulation algorithms for multidimensional nonlinear response of classical many-body systems. *J. Chem. Phys.*, 119:9344, 2003.

[108] Q. Shi and E. Geva. A comparison between different semiclassical approximations for optical response functions in nonpolar liquid solution II. the signature of excited state dynamics on two-dimensional spectra. *J. Chem. Phys.*, 129:124505, 2008.

[109] S. Mukamel. *Principles of Nonlinear Optical Spectroscopy.* Oxford University Press, New York, 1995.

[110] G. Hanna and E. Geva. A computational study of the 1d and 2d infrared spectra of a vibrational mode strongly coupled to its environment: Beyond the cumulant and condon approximations. *J. Phys. Chem. B*, 112:12991, 2008.

[111] G. Hanna and E. Geva. Multi-dimensional spectra via the mixed quantum-classical Liouville method: Signatures of nonequilibrium dynamics. *J. Phys. Chem. B*, 113: 9278, 2009.

[112] G. Hanna and E. Geva. Signature of nonadiabatic transitions on the pump-probe infrared spectra of a hydrogen-bonded complex dissolved in a polar solvent: A computational study. *J. Phys. Chem. B*, 115:5191, 2011.

[113] L. Seidner, G. Stock, and W. Domcke. Nonperturbative approach to femtosecond spectroscopy: General theory and application to multidimensional nonadiabatic photoisomerization processes. *J. Chem. Phys.*, 103:3998, 1995.

[114] B. Wolfseder, L. Seidner, G. Stock, and W. Domcke. Femtosecond pump-probe spectroscopy of electron-transfer systems: A nonperturbative approach. *Chem. Phys.*, 217:275, 1997.

[115] M. F. Gelin, A. V. Pisliakov, D. Egorova, and W. Domcke. A simple model for the calculation of nonlinear optical response spectra and femtosecond time-resolved spectra. *J. Chem. Phys.*, 118:5287, 2003.

[116] M. F. Gelin, D. Egorova, and W. Domcke. Efficient method for the calculation of time- and frequency-resolved four-wave mixing signals and its application to photon-echo spectroscopy. *J. Chem. Phys.*, 23:164112, 2005.

[117] D. Gelman, G. Katz, R. Kosloff, and M. A. Ratner. Dissipative dynamics of a system passing through a conical intersection: Ultrafast pump-probe observables. *J. Chem. Phys.*, 123:134112, 2005.

[118] H. B. Wang and M. Thoss. Nonperturbative simulation of pump-probe spectra for electron transfer reactions in the condensed phase. *Chem. Phys. Lett.*, 389:43–50, 2004.

[119] T. Mančal, A. V. Pisliakov, and G. R. Fleming. Three-dimensional optical three-pulse

photon echo spectroscopy. I. Nonperturbative approach to the calculation of spectra. *J. Chem. Phys.*, 124:234504, 2006.

[120] A. V. Pisliakov, T. Mančal, and G. R. Fleming. Two-dimensional optical three-pulse photon echo spectroscopy II. Signatures of coherent electronic motion and exciton population transfer in dimer two-dimensional spectra. *J. Chem. Phys.*, 124:234505, 2006.

[121] B. J. Ka and E. Geva. A nonperturbative calculation of nonlinear spectroscopic signals in liquid solution. *J. Chem. Phys.*, 125:214501, 2006.

[122] H. Wang and M. Thoss. Nonperturbative quantum simulation of time-resolved nonlinear spectra: Methodology and application to electron transfer reactions in the condensed phase. *Chem. Phys.*, 347:139, 2008.

[123] M. F. Gelin, D. Egorova, and W. Domcke. Efficient calculation of the polarization induced by n coherent laser pulses. *J. Chem. Phys.*, 131:194103, 2009.

[124] M. F. Gelin, D. Egorova, and W. Domcke. Efficient calculation of time- and frequency-resolved four-wave-mixing signals. *Acc. Chem. Res.*, 42:1290, 2009.

[125] R. P. Bell. *The Proton in Chemistry.* Chapmann & Hall, London, 1973.

[126] A. A. Kornyshev, M. Tosi, and J. Ulstrup, editors. *Electron and Ion Transfer in Condensed Media.* World Scientific, Singapore, 1997.

[127] A. Warshel. *Computer modelling of chemical reactions in enzymes and solutions.* Wiley-Interscience, 1991.

[128] P. K. Agarwal, S. P. Webb, and S. Hammes-Schiffer. Computational studies of the

mechanism for proton and hydride transfer in liver alcohol dehydrogenase. *J. Am. Chem. Soc.*, 122(19):4803–4812, 2000.

[129] E. F. Caldin and V. Gold. *Proton-transfer reactions*. Springer, 2013.

[130] R. M. Tarkka and S. A. Jenekhe. Effects of electronic delocalization on intramolecular proton transfer. *Chem. Phys. Lett.*, 260(5-6):533–538, 1996.

[131] F. L. Carter. *Molecular electronic devices*, volume 1. M. Dekker, 1982.

[132] Y. Fan, H. Hu, and H. Liu. Sustainable power generation in microbial fuel cells using bicarbonate buffer and proton transfer mechanisms. *Environ. Sci. Technol.*, 41(23): 8154–8158, 2007.

[133] D. E. Moilanen, D. B. Spry, and M. D. Fayer. Water dynamics and proton transfer in nafion fuel cell membranes. *Langmuir*, 24(8):3690–3698, 2008.

[134] K. D. Kreuer. On the development of proton conducting polymer membranes for hydrogen and methanol fuel cells. *J. Membr. Sci.*, 185(1):29–39, 2001.

[135] H. Azzouz and D. Borgis. A quantum molecular-dynamics study of proton-transfer reactions along asymmetrical H bonds in solution. *J. Chem. Phys.*, 98:7361, 1993.

[136] T. Yamamoto and W. H. Miller. Path integral evaluation of the quantum instanton rate constant for proton transfer in a polar solvent. *J. Chem. Phys.*, 122:044106, 2005.

[137] R. Collepardo-Guevara, I. R. Craig, and D. E. Manolopoulos. Proton transfer in a polar solvent from ring polymer reaction rate theory. *J. Chem. Phys.*, 128(14):144502, 2008.

[138] S. Sugawara, T. Yoshikawa, T. Takayanagi, M. Shiga, and M. Tachikawa. Quantum

proton transfer in hydrated sulfuric acid clusters: A perspective from semiempirical path integral simulations. *J. Phys. Chem. A*, 115(42):11486–11494, 2011.

[139] V. Guallar, V. S. Batista, and W. H. Miller. Semiclassical molecular dynamics simulations of excited state double-proton transfer in 7-azaindole dimers. *J. Chem. Phys.*, 110:9922, 1999.

[140] V. Guallar, V. S. Batista, and W. H. Miller. Semiclassical molecular dynamics simulations of intramolecular proton transfer in photoexcited 2-(2'-hydroxyphenyl)–oxazole. *J. Chem. Phys.*, 113(21):9510–9522, 2000.

[141] S. Hammes-Schiffer and J. C. Tully. Proton transfer in solution: Molecular dynamics with quantum transitions. *J. Chem. Phys.*, 101:4657, 1994.

[142] S. Hammes-Schiffer and J. C. Tully. *J. Chem. Phys.*, 103:8528, 1995.

[143] S. R. Billeter, S. P. Webb, P. K. Agarwal, T. Iordanov, and S. Hammes-Schiffer. *J. Chem. Phys.*, 114:6925, 2001.

[144] S. R. Billeter, S. P. Webb, T. Iordanov, P. K. Agarwal, and S. Hammes-Schiffer. *J. Am. Chem. Soc.*, 123:11262, 2001.

[145] J. Steadman and J. A. Syage. Picosecond mass-selective measurements of phenol-(nh3)n acid-base chemistry in clusters. *J. Chem. Phys.*, 92(7):4630–4632, 1990.

[146] J. A. Syage and J. Steadman. Picosecond measurements of phenol excited-state proton-transfer in clusters. 1. solvent basicity and cluster size effects. *J. Chem. Phys.*, 95(4):2497–2510, 1991.

[147] R. Knochenmuss, G. R. Holtom, and D. Ray. Proton-transfer reaction-rates as a

probe of size-dependent properties of large water clusters. *Chem. Phys. Lett.*, 215 (1-3):188–192, 1993.

[148] S. K. Kim, J. K. Wang, and A. H. Zewail. Femtosecond ph jump - dynamics of acid-base reactions in solvent cages. *Chem. Phys. Lett.*, 228(4-5):369–378, 1994.

[149] J. A. Syage. Ultrafast measurements of chemistry in clusters - excited-state proton-transfer. *J. Phys. Chem.*, 99(16):5772–5786, 1995.

[150] S. K. Kim, J. J. Breen, D. M. Willberg, L. W. Peng, A. Heikal, J. A. Syage, and A. H. Zewail. Solvation ultrafast dynamics of reactions. 8. acid-base reactions in finite-sized clusters of naphthol in ammonia, water, and piperidine. *J. Phys. Chem.*, 99(19):7421–7435, 1995.

[151] A. L. Sobolewski and W. Domcke. Photoinduced electron and proton transfer in phenol and its clusters with water and ammonia. *J. Phys. Chem. A*, 105(40):9275–9283, 2001.

[152] M. Meuwly, A. Bach, and S. Leutwyler. Grotthus-type and diffusive proton transfer in 7-hydroxyquinoline center dot(nh3)(n) clusters. *J. Am. Chem. Soc.*, 123(46): 11446–11453, 2001.

[153] A. Bach, C. Tanner, C. Manca, H. M. Frey, and S. Leutwyler. Ground- and excited state proton transfer and tautomerization in 7-hydroxyquinoline center dot(NH3)(n) clusters: Spectroscopic and time resolved investigations. *J. Chem. Phys.*, 119(12): 5933–5942, 2003.

[154] W. H. Thompson. Proton transfer in nanoconfined polar solvents. ii. adiabatic proton transfer dynamics. *J. Phys. Chem. B*, 109:18201, 2005.

[155] H. Kim and R. Kapral. Solvation and proton transfer in polar molecule nanoclusters. *J. Chem. Phys.*, 125:234309, 2006.

[156] Z. Sun, C. K. Siu, O. P. Balaj, M. Gruber, V. E. Bondybey, and M. K. Beyer. Proton transfer in ionic water clusters. *Angew. Chem. Int. Ed.*, 45(24):4027–4030, 2006.

[157] C. Lao-Ngam, P. Asawakun, S. Wannarat, and K. Sagarik. Proton transfer reactions and dynamics in protonated water clusters. *Phys. Chem. Chem. Phys.*, 13(10): 4562–4575, 2011.

[158] S. Rakshit, R. Saha, P. K. Verma, and S. M. Pal. Role of solvation dynamics in excited state proton transfer of 1-naphthol in nanoscopic water clusters formed in a hydrophobic solvent. *Photochemistry and Photobiology*, 88(4):851–859, 2012.

[159] C. S. Sow, J. Tomkins, and G. Hanna. Computational study of the one-and two-dimensional infrared spectra of a proton-transfer mode in a hydrogen-bonded complex dissolved in a polar nanocluster. *ChemPhysChem*, 14(14):3309–3318, 2013.

[160] S. Li and W. H. Thompson. How accurate is time-independent perturbation theory for calculating frequency shifts of diatomic molecules in rare gas fluids? *Chem. Phys. Lett.*, 405:304, 2005.

[161] J. Rodriguez, J. Marti, E. Guardia, and D. Laria. Protons in non-ionic aqueous reverse micelles. *J. Phys. Chem. B*, 111:4432, 2007.

[162] K. R. Mitchell-Koch and W. H. Thompson. Infrared spectra of a model phenol-amine proton transfer complex in nanoconfined ch3cl. *J. Phys. Chem. B*, 112:7448, 2008.

[163] J. Tomkins and G. Hanna. Signatures of nanoconfinement on the linear and nonlinear vibrational spectroscopy of a model hydrogen-bonded complex dissolved in a polar solvent. *J. Phys. Chem. B*, 117(43):13619–13630, 2013.

[164] I. V. Aleksandrov. The statistical dynamics of a system consisting of a classical and a quantum subsystem. *Z. Naturforsch.*, 36:902–908, 1981.

[165] W. Boucher and J. Traschen. Semiclassical physics and quantum fluctuations. *Phys. Rev. D*, 37:3522–3532, 1988.

[166] Z.-Q. Zhang and Q.-J. Chu. *Phys. Lett. A*, 131:517, 1988.

[167] R. Balescu and W. Y. Zhang. Kinetic equation, spin hydrodynamics and collisional depolarization rate in a spin-polarized plasma. *J. Plasma phys.*, 40(2):215–234, 1988.

[168] M. H. Anderson, J. N. Ensher, M. R. Matthews, C. E Weisman, and E. A. Cornell. Observation of bose-einstein condensation in a dilute atomic vapor. *Science*, 269:198, 1995.

[169] O. V. Prezhdo and P. J. Rossky. Mean-field molecular dynamics with surface hopping. *J. Chem. Phys.*, 107:825, 1997.

[170] E. Wigner. On the quantum correction for thermodynamic equilibrium. *Phys. Rev.*, 40:749, 1932.

[171] J. C. Tully. *Int. J. Quantum Chem.*, 25:299, 1991.

[172] M. P. Miller and C. W. McCurdy. *J. Chem. Phys.*, 69:5163, 1978.

[173] M. Thoss and G. Stock. Mapping approach to the semiclassical description of nonadiabatic quantum dynamics. *Phys. Rev. A*, 59:64, 1999.

[174] J. Schwinger. *Quantum theory of angular momentum.* L.C. Biedenharn and H. V. Dam, New York, 1965.

[175] S. Nielsen, R. Kapral, and G. Ciccotti. Statistical mechanics of quantum-classical systems. *J. Chem. Phys.*, 115:5805–5815, 2001.

[176] M. Cho. Coherent two-dimensional optical spectroscopy. *Chem. Rev.*, 108:1331, 2008.

[177] J. P. Ogilvie and K. J. Kubarych. Multidimensional electronic and vibrational spectroscopy: an ultrafast probe of molecular relaxation and reaction dynamics. *Advances in Atomic, Molecular, and Optical Physics*, 57:249, 2009.

[178] U. Müller and G. Stock. *J. Chem. Phys.*, 108:7516, 1998.

[179] A. Kelly and Y. M. Rhee. *J. Phys. Chem. Lett.*, 2:808–812, 2011.

[180] Y. Tanimura and Y. Maruyama. Gaussian-Markovian quantum Focker-Planck approach to nonlinear spectroscopy of a displaced morse potential system: Dissociation predissociation, and optical stark effects. *J. Chem. Phys.*, 107:1779, 1997.

[181] M. F. Gelin, D. Egorova, and W. Domcke. A new method for the calculation of two-pulse time-and frequency-resolved spectra. *Chem. phys.*, 312(1-3):135–143, 2005.

[182] R. Kapral. Progress in the theory of mixed-quantum classical dynamics. *Annu. Rev. Phys. Chem.*, 57:129, 2006.

[183] H. Wang, M. Thoss, and W. H. Miller. *J. Chem. Phys.*, 115:2979, 2001.

[184] H. Wang, X. Song, D. Chandler, and W. H. Miller. Semiclassical study of electronically nonadiabatic dynamics in the condensed phase: Spin-boson problem with debye spectral density. *J. Chem. Phys.*, 110:4828, 1999.

[185] P. Huo and D. F. Coker. *Mol. Phys.*, 110:1035, 2012.

[186] K. Hyojoon and R. Kapral. Quantum bath effects on nonadiabatic reaction rates. *Chem. Phys. Lett.*, 423:76, 2006.

[187] B. R. Landry and J. E. Subotnik. How to Recover Marcus theory with Fewest Switches Surface Hopping: Add Just a Touch of Decoherence. *J. Chem. Phys.*, 137:22A513, 2012.

[188] F. Martinez, N. Rekik, and G. Hanna. Simulation of nonlinear optical signals via approximate solutions of the quantum–classical Liouville equation: Application to the pump–probe spectroscopy of a condensed phase electron transfer reaction. *Chem. Phys. Lett.*, 573:77–83, 2013.

[189] F. Martinez and G. Hanna. Assessment of approximate solutions of the quantum–classical Liouville equation for dynamics simulations of quantum subsystems embedded in classical environments. *Mol. Simulat.*, 41(1-3):107–122, 2015.

[190] M. F. Gelin, D. Egorova, and W. Domcke. Efficient calculation of time- and frequency-resolved four-wave-mixing signals. *Acc. Chem. Res.*, 42(9):1290–1298, 2009.

[191] T. Mančal, A. V. Pisliakov, and G. R. Fleming. Two-dimensional optical three-pulse photon echo spectroscopy. i. nonperturbative approach to the calculation of spectra. *J. Chem. Phys.*, 124(23):234504, 2006.

[192] Z. Wang, A. Pakoulev, Y. Pang, and D. D. Dlott. Vibrational substructure in the OH stretching bend in water. *Chem. Phys. Lett.*, 378:281, 2003.

[193] S. Bonella and D. F. Coker. A semiclassical limit for the mapping Hamiltonian approach to electronically nonadiabatic dynamics. *J. Chem. Phys.*, 114:7778, 2001.

[194] S. Bonella and D. F. Coker. Land-map, a linearized approach to nonadiabatic dynamics using the mapping formalism. *J. Chem. Phys.*, 122:194102, 2005.

[195] B. Bigot, B. J. Costa-Cabral, and J. L. Rivail. Conformational equilibrium of 1,

2-dichloroethane in methylchloride. a monte carlo simulation of the differential gauche–anti solvation. *J. Chem. Phys.*, 83(6):3083–3094, 1985.

[196] M. P. Allen and D. J. Tildesley. *Computer Simulation of Liquids.* Oxford University Press, Oxford, 1987.

[197] H. C. Andersen. Rattle: A “velocity” version of the Shake algorithm for molecular dynamics calculations. *J. Comp. Phys.*, 52:24, 1983.

[198] J. P. Ryckaert, G. Ciccotti, and H. J. C. Berendsen. *J. Comput. Phys.*, 23:327, 1977.

[199] S. Consta and R. Kapral. Dynamics of proton transfer in mesoscopic clusters. *J. Chem. Phys.*, 104:4581, 1996.

[200] S. Li and W. H. Thompson. Proton transfer in nanoconfined polar solvents. 1. free energies and solute position. *J. Phys. Chem. B*, 109:4941, 2005.